NUMERICAL AND EXPERIMENTAL STUDIES OF THREE-DIMENSIONAL CRACK EVOLUTION IN ALUMINUM ALLOYS: MACROSCALE TO MICROSCALE

A Dissertation

Presented to the Faculty of the Graduate School

of Cornell University

in Partial Fulfillment of the Requirements for the Degree of

Doctor of Philosophy

by

Ashley Dawn Spear

May 2014

NUMERICAL AND EXPERIMENTAL STUDIES OF THREE-DIMENSIONAL CRACK EVOLUTION IN ALUMINUM ALLOYS: MACROSCALE TO MICROSCALE

Ashley Dawn Spear, Ph.D.

Cornell University 2014

In a broad sense, the work described herein addresses either extreme of a traditional da/dN vs. dK plot. The first chapter addresses the uppermost limit of such plot, where tearing represents the limit state of structural failure. Subsequent chapters address the lower limit, where emphasis is placed on nucleation and early propagation of microstructurally small fatigue cracks (MSFCs). A common theme throughout the dissertation is the development of new tools and techniques (be they experimental or numerical) to enable unprecedented interrogation of crack evolution in 3D, with applications to various aluminum-alloy structures. Each chapter represents a separate body of work providing novel contributions in one or more areas involving fracture mechanics (viz. structural prognosis, corrosion science and engineering, and materials characterization). A brief overview of each chapter is described next.

In Chapter 1, a methodology is described for predicting in real time the residual strength of structures with discrete-source damage. An artificial neural network (ANN) is trained using linear-elastic fracture mechanics (LEFM)-based data from numerical models; the ANN predicts residual strength given a set of damage parameters. Section 1.3 focuses on augmenting the existing LEFM-based modeling toolset to simulate ductile tearing and thereby improve resid-

ual strength values used to train an ANN. Validation results are presented for two ductile-tearing simulations. Chapters 2 through 4 focus on MSFC initiation and propagation in an Al-Mg-Si alloy used to line composite-overwrapped pressure vessels. Chapter 2 describes an experimental study regarding the effect of an alkaline-based chemical milling treatment used to dimensionally reduce the Al-Mg-Si pressure-vessel liners. 3-D scanning electron microscopy is employed to quantify surface pitting caused by the chemical-milling treatment. The 3-D surface characteristics, along with high-magnification fractographs, are used to explain the observed 50% reduction in low-cycle fatigue lives among the chemically-milled specimens compared to a control group. In Chapter 3, an experimental methodology based on post-mortem measurements is developed to quantify 3-D rates of propagation and crack-surface crystallography for a naturally nucleated MSFC in an Al-Mg-Si specimen. The measurements are made possible through recent developments in 3-D characterization methods. Findings from the study demonstrate: 1) the complexity and variability of 3-D MSFC evolution in the Al-Mg-Si alloy and 2) the viability of the post-mortem characterization approach for quantifying 3-D MSFC evolution in polycrystalline alloys. The dissertation culminates with Chapter 4, which, for the first time, demonstrates the 3-D digital reconstruction and numerical simulation of a sequence of directly measured MSFCs, where both MSFC geometry and individual grain morphologies and orientations are explicitly represented at the polycrystalline length scale. The numerical reconstruction is demonstrated using 3-D measurements from Chapter 3. Work from Chapters 1 and 2 is published in [1, 2, 3, 4] and [5], respectively. The combined work from Chapters 3 and 4 is described in [6, 7, 8] and is currently in preparation for additional journal publication.

BIOGRAPHICAL SKETCH

Ashley is originally from Cheyenne, Wyoming, and attended the University of Wyoming for her undergraduate studies. She graduated *summa cum laude* with a Bachelor of Science degree in Architectural Engineering in 2007. Ashley joined the Cornell Fracture Group in 2008 to begin pursuing both a Master of Science and a Doctor of Philosophy degree in Civil and Environmental Engineering with a Structural Engineering option.

To my family, for paving the way

ACKNOWLEDGEMENTS

This work would not have been possible without the support and guidance of so many. First, heartfelt gratitude is expressed to Professor Ingraffea for providing me with invaluable advisory in the way of both academic and personal affairs. I know I will call upon many of the lessons he has taught me as I embark on my own journey as a faculty advisor. Thank you also to Professors Alan Zehnder and Chris Earls and to Dr. Ed Glaessgen for serving on my special committee. My co-authors deserve tremendous gratitude for their contributions in shaping and helping to realize many of the ideas described in this work: Robert Suter, Frankie Li, Jonathan Lind, Jacob Hochhalter, Michael Veilleux, Albert Cerrone, and Amanda Priest – thank you. Special thanks also to many of the folks from NASA Langley Research Center (or its affiliates) who were indispensable in helping me to find my way around the polishing labs, load frames, and SEMs: Roy Crooks, Wes Tayon, Vipul Gupta, Scott Willard, William Johnston, Gregory Shanks, James Baughman, Stewart Walker, Harold "Clay" Claytor, David Hartman, and Johnnie West. A number of people have provided valuable discussions that helped to guide various aspects of my work, including Wilkins Aquino, Robert Piascik, Stephen Smith, Robert Bucci, Mark James, Joseph Lewis, Lorie Grimes-Ledesma, David Dawicke, and Don Zimmerman. A special debt of gratitude is also owed to members of the Cornell Fracture Group, especially Bruce Carter and Brett Davis, who have been both colleagues and friends since I joined the group in 2008.

Funding for this work has been provided largely through the National Science Foundation (NSF) Graduate Research Fellowship Program under Grant No. DGE-0707428 and by NASA under contract NNX08AC50A. Resources have also

been provided under the auspices of the U.S. Department of Energy (DOE) by Lawrence Livermore National Laboratory under contract DE-AC52-07NA27344 and by grant DESC0002001 at Carnegie Mellon University. Use of the Advanced Photon Source, an Office of Science User Facility operated for the U.S. DOE Office of Science by Argonne National Laboratory, was supported by the U.S. DOE under Contract No. DE-AC02-06CH11357. Reconstruction of HEDM data as well as simulations described in Chapter 4 were conducted on Texas Advanced Computing Center's cluster Stampede through allocation TG-MSS110031 provided by the Extreme Science and Engineering Discovery Environment (XSEDE) Science Gateways program and supported by the NSF. Dr. Gerd Heber developed the parallel finite-element code used in the simulations presented in Chapter 4. The crystal-plasticity model used in this work was implemented by Drs. Antoinette Maniatty, David Littlewood, and Paul Wawrzynek.

Finally, I would not be writing this acknowledgement were it not for the loved ones in my life who have encouraged me to pursue my dreams, have supported my ambitions, have provided solace in times of need, and have taught me life lessons that I cannot begin to articulate here: Mom, Pops, Gary, Velta, Breck, Kev, Seren, and Kenz – thank you. Finally, my dearest and sweetest thank you goes to my husband, Mike, who has shared in my trials and tribulations; I cannot imagine a better life partner.

TABLE OF CONTENTS

LIST OF TABLES

LIST OF FIGURES

CHAPTER 1

A NUMERICAL FRAMEWORK FOR REAL-TIME PREDICTIONS OF RESIDUAL STRENGTH BASED ON MACROSCALE ELASTIC-PLASTIC FRACTURE SIMULATIONS

1.1 Introduction

Resilient aircraft control involves adaptive responses to off-nominal flight conditions, including the incurrence of structural discrete-source damage during flight. *Discrete-source damage* is typically manifested as a result of a structural impact event, including hail- and birdstrike. In 2003, an Airbus A300 operated by DHL was struck by a surface-to-air missile after takeoff from Baghdad, Iraq, causing discrete-source damage to crucial control surfaces of the left wing [9]. In 2008, a Boeing 747-438 operated by Qantas Airways incurred in-flight structural damage to the fuselage and right wing leading edge following the failure of an onboard oxygen cylinder [10]. Although the aircraft landed safely in both cases, these examples motivate a need for more resilient, adaptive control system responses.

In these types of cases, problems associated with in-flight discrete-source damage, for example inability to sustain original design loads, can be exacerbated by crack propagation from damaged regions. To avoid unstable crack propagation, load levels must be maintained below a reduced load-carrying capacity, or *residual strength*, of damaged flight structures. Adaptive control system responses might include automatic adjustment of certain flight parameters (e.g. velocity, maximum acceleration) to accommodate structural residual strength. This ac-

commodation implies that accurate residual strength predictions of flight structures with complex damage configurations be made *in real time, during flight*; this capability currently does not exist for commercial aviation.

Challenges to developing an adaptive response technology include accurately predicting residual strength of discrete-source damaged structures both *offline* (i.e. during control system design) and *online* (i.e. in real time onboard the aircraft). In the offline context, researchers have developed various tools for determining residual strength of thin, damaged metallic structures using elastic-plastic fracture mechanics (EPFM)-based numerical methods. For example, two common finite element (FE) modeling techniques involve nodal release and adaptive remeshing. Both techniques represent cracks geometrically [11]. The former, however, prescribes possible crack trajectories, which introduces inherent mesh dependencies into fracture simulations and limits generality of crack path predictions. Nodal release techniques have been used in 2D [12, 13, 14, 15, 16, 17, 18, 19] and in 3D [20, 21, 22] for studying crack growth parameters and predicting residual strength of structures where the crack path was known a priori and where mesh refinement along the crack path sufficiently characterized growth increments. Adaptive remeshing techniques avoid such mesh dependencies and enable simulation of arbitrary crack propagation using evolutionary models or criteria [23, 24, 25, 26, 27]. Adaptive remeshing techniques have been implemented in both 2D [28] and in 3D [29, 30]. Of the described techniques, 3-D, adaptively remeshed, elastic-plastic tearing simulations provide the most general prediction capabilities for crack growth and residual strength.

It is infeasible to perform a rigorous and computationally intensive crack growth simulation within the possible short time span following a discrete-source damage event. Thus, an approximation, or *surrogate model*, is needed for making online predictions of residual strength. Queipo et al. provided a complete description of surrogate modeling development and optimization [31]. With regard to surrogate construction, they described both parametric (e.g. polynomial regression and Kriging) and nonparametric (e.g. radial basis functions) approaches. In nonparametric approaches, a global functional form relating system input to system response is not assumed.

Artificial neural networks (ANNs) are a nonparametric surrogate modeling approach and are trained to infer a nonlinear mapping from system input to system response, or output. The reader is referred to [32] for an extensive methodology overview of the most widely used types of ANNs. Different types of ANNs have been applied extensively for damage detection [33, 34, 35, 36, 37, 38, 39] and, to a much lesser extent, for damage assessment. Ouenes et al. employed an ANN methodology to predict fracture indicators (e.g. density of fractures) in naturally fractured rock reservoirs as a function of various geological and geophysical data [40]. Pidaparti et al. employed an ANN to predict residual strength and corrosion rate of aging aircraft panels with collinear multi-site damage by training with experimental results and validating with both experimental results and analytical solutions [41]. Recently, Mohanty et al. used a Gaussian process (GP) approach to predict fatigue crack growth in aluminum 2024-T351 specimens by training two distinct models, one presented with experimental load parameters as input and another presented with piezoelectric sensor signals as input [42]. In that work, Mohanty et al. used

observed fatigue crack lengths and growth rates as known output for training each model.

Alternatively, ANNs can be trained using results from numerical experiments, or simulations [43]. For example, Sankararaman et al. recently used linear-elastic fracture parameters computed from FE analyses to train a GP model as part of a method to statistically infer equivalent initial flaw size in fatigue applications [44]. High-fidelity numerical simulations can provide training data when analytically- and experimentally-derived data are limited due either to a lack of generally applicable analytical solutions or to prohibitive costs of obtaining sufficient experimental data.

The purpose of the work presented here is two-fold: (1) to illustrate a methodology for creating a surrogate model as a real-time residual strength prediction tool and (2) to describe and validate numerical tools for making accurate residual strength predictions offline using fully 3-D, elastic-plastic, FE-based crack growth simulations. The high-fidelity, more computationally expensive tools described in (2) can provide training data that, when coupled with the surrogate model methodology described in (1), can be used in the design of adaptive response technology.

Consistent with the two-fold purpose, this chapter is divided into two primary sections. Section 1.2 illustrates the methodology for developing a surrogate model (in particular, an ANN) that predicts residual strength as a function of discrete-source damage parameters. The methodology is illustrated using a relatively simple proof-of-concept example. The procedure for gathering training

data is described in 1.2.1 and 1.2.2. Because an implementation-ready ANN is beyond the scope of this work, training data for the proof-of-concept example relies on reduced-order residual strength approximations. After collecting training data, a simple ANN is constructed in 1.2.3 by optimizing certain performance parameters. Finally, a sensitivity study is conducted in 1.2.4 to understand the effect of each damage parameter on predicted residual strength specifically for the proof-of-concept structure.

Section 1.3 improves upon offline residual strength prediction tools used in Section 1.2 by simulating 3-D, elastic-plastic tearing. The tools provide more general crack growth simulation capabilities and can be used to generate accurate residual strength training data. A relatively large, integrally-stiffened panel (ISP) that exhibits crack branching is simulated in 1.3.3 to validate the tools.

Results and discussions from the ANN proof-of-concept example and from the elastic-plastic tearing simulation are provided in each respective section. Section 1.4 offers a summary and conclusions for the entirety of this work.

1.2 Neural Network Development and Methodology

This section describes the development of a surrogate model for predicting residual strength of discrete-source damaged aircraft structures in real time. A global functional form is not assumed for the nonlinear relationship between residual strength and the damage parameters influencing it; thus, a nonparametric surrogate model is developed. In particular, a supervised ANN is considered due to rapid prediction capabilities amenable to real-time applications.

In Fig. 1.1, the upper dashed region shows the generalized procedure for developing an ANN (surrogate model) that predicts residual strength as a function of parameterized discrete-source damage. The lower dashed region shows the functionality of the ANN (surrogate model) in a real-time context.

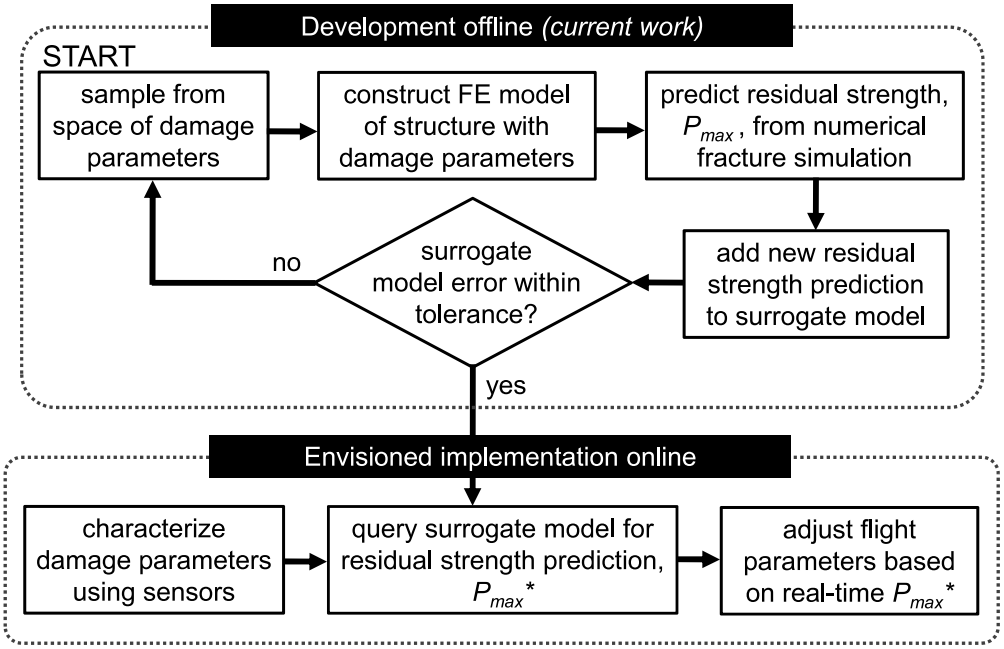

Figure 1.1: Upper dashed box illustrates a general approach for developing a surrogate model to predict residual strength of damaged structures. Lower dashed box illustrates how the surrogate model would function onboard an aircraft for predicting residual strength of damaged structures in real time.

The first step in this type of surrogate model development is typically referred to as design of experiment (DOE) [31] and involves obtaining data points that will be used to train and test the ANN. The DOE should be based on the intended application of the ANN. For example, if the ANN is intended to provide residual strength predictions in terms of maximum allowable bending moment

in a damaged aircraft wing, then the data points should be gathered using an appropriate wing structure with applied boundary conditions of interest. Each data point includes sampled input variable(s) and corresponding known system response(s), called *target output*. Once the ANN has been trained to map given input to target output, it becomes a useful tool for predicting system response when presented with new input that is within the training range but does not necessarily correspond to data points used for training.

To illustrate the methodology, a simple ANN is developed using a representative wing structure and reduced-order (linear-elastic) approximations for predicting residual strength. The representative wing structure is a 61.0 x 91.4 cm^2 integrally-stiffened panel (ISP) with three blade stiffeners each 5.1 cm in height, as shown in Fig. 1.2. The ISP skin and stiffeners are 0.23 cm thick. The panel is modeled as linear-elastic with elastic modulus E = 71.0 GPa and Poisson's ratio ν = 0.33, similar to values for a 2*XXX* series lower wing skin aluminum alloy (AA).

Multiple FE models of the uncracked panel are constructed using ABAQUS® [46]. A shell-solid modeling technique is employed, where each panel is modeled using 3-D solid elements in a region that will contain damage and shell elements elsewhere, as depicted schematically in Fig. 1.2. In this way, 3-D constraint is inherently captured along crack fronts using fully 3-D solid elements, while shell elements help maintain a level of computational efficiency yet are able to capture out-of-plane deformation and possible buckling. The shell and solid element regions are joined using a coupling constraint, whereby resultant forces and moments acting at shell edge nodes on the shell-solid boundary are

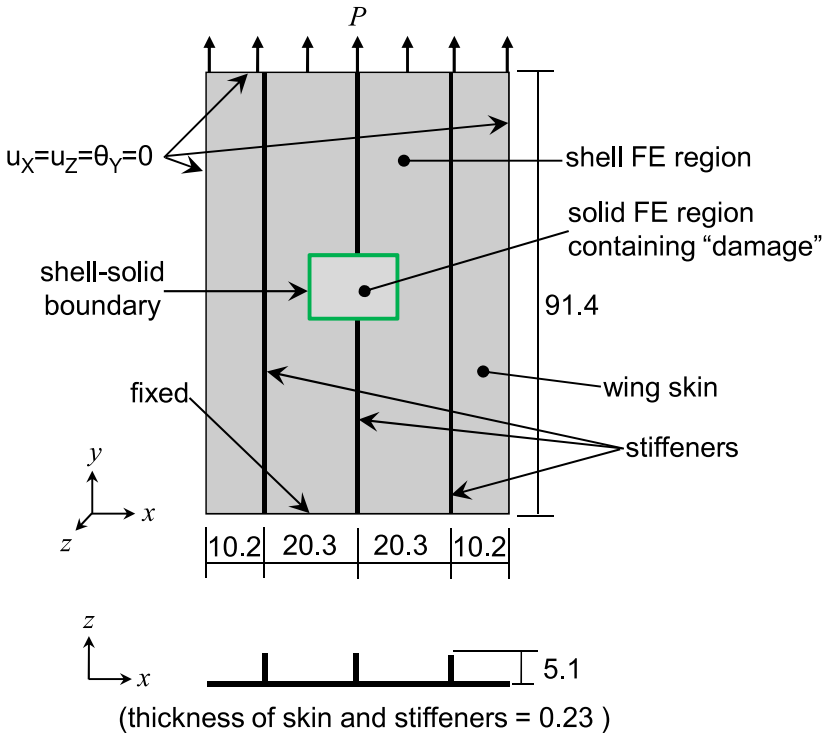

Figure 1.2: Schematic of ISP model with dimensions similar to those used in [45]. Plan view (top) and cross-section showing integral blade stiffeners (bottom). A damage-containing region is modeled using 3-D solid elements (enclosed in shell-solid boundary) while remainder of panel is modeled with shell elements. Dimensions in cm.

distributed as forces acting at nodes located in a region of influence on the solid surface of the shell-solid boundary. A mesh refinement study is carried out to ensure adequate discretization of the panel models. *Uncracked* panels are modeled using approximately 2050 quadratic shell elements and between 1800 and 17,300 quadratic brick elements, depending on the size of the damaged region. Boundary conditions for the ISP models are defined to emulate tensile loading conditions for a region of the lower wing surface and are shown schematically in Fig. 1.2.

A supplementary study was carried out to determine shell-solid boundary effects on nearby crack fronts in order to minimize the size of the solid region without affecting stress intensity factors (SIFs) computed along nearby crack fronts. Maintaining fracture parameter accuracy is especially important since fracture parameters are used to predict structural residual strength (described in 1.2.2), which is in turn used to train the ANN (described in 1.2.3). The supplementary study considered a 61.0 x 91.4 cm^2 unstiffened panel of the same (linear-elastic) material and thickness as the ISP described above. The panel had a single, 12.7 cm long, centrally-located through-crack oriented in the x direction (normal to applied tensile load). Both tensile and bending conditions were considered in the study. The panel was modeled entirely with shell elements except for a region containing the crack, which was modeled with 3-D solid elements. All model parameters remained constant while varying the size (both in-plane dimensions) of the square-shaped solid region, therefore varying the distance from the shell-solid boundary to the crack front. The size of the solid region was initially slightly larger than the length of the crack and was increased until computed SIFs converged. Results from the supplementary study indicated that for a static, linear-elastic crack, the distance from shell-solid boundary to nearest crack front should be no less than 25% of the crack length. This ensures that the shell-solid boundary has negligible effect on computed SIFs. The same general rule is applied to the example ISP models described in the ANN study.

The following sections describe the generally applicable methodology for developing an ANN as a real-time residual strength prediction tool.

1.2.1 Input Variables: Discrete-source Damage Parameters

Discrete-source damage in this work is represented by a symmetric, star-shaped, array of equi-length cracks, as depicted in Fig. 1.3(b). This representation of discrete-source damage is motivated by observations of petaling caused by penetration damage to thin metallic structures, see Fig. 1.3(a). If all of the cracks in the star-shaped array of Fig. 1.3(b) separate under load (i.e. there are no crack closure effects), then the cracked region transfers no load and effectively represents a circular hole with petaling edges, similar to that shown in Fig. 1.3(a). The damage representation is parameterized by the following four variables that are postulated to influence residual strength of the ISP: n (number of crack "legs" in the damage configuration); a (length of each crack leg, in cm); d_x (distance from middle stiffener to center of damage configuration, in cm); and θ (orientation of damage configuration, defined as the angle between the positive x axis and the nearest crack leg).

The sample space of damage configurations is defined by a range of values for each parameter. Ranges can be specified based on accident reports, photographic evidence, potential structural threats, design specifications, and so forth. Inherently, the ANN predictions are valid only for input parameter values within the range of training data. Thus, it is necessary to define the sample space based on the particular ANN application. In the example ANN, ranges for each damage parameter are limited to some extent by the ISP geometry. Each range is given in Table 1.1. The parameter n, takes integer values ranging from two to six. The range of θ depends on n due to the definition of orientation and the symmetry of the star-shaped configuration. The range of a is defined in terms of ISP bay width, from $1/8 * baywidth$ to $1/4 * baywidth$. Due to symmetry

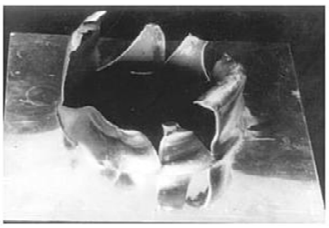

a)

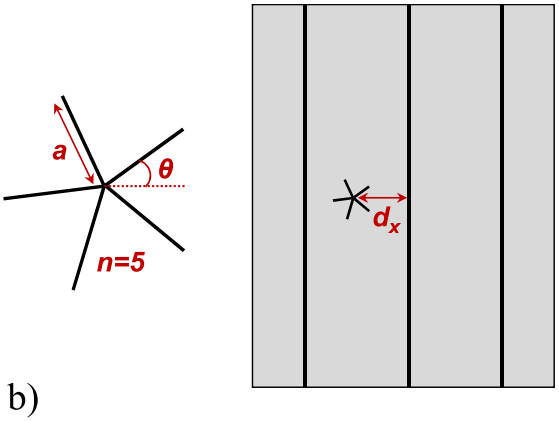

b)

Figure 1.3: (a) Petaling on the reverse side of a metallic sheet subject to explosive, discrete-source damage [47]. (b) Schematic showing the representation and parameterization of discrete-source damage in the ANN example described in this work.

of the ISP model, the parameter d_x ranges from 10.2 cm (damage centered in mid-bay) to 0 (damage centered at middle stiffener). If the damage is located such that the damage-containing, solid FE region overlaps anywhere with the middle stiffener, the stiffener is assumed to be severed in the damaged region and is modeled explicitly as such.

The damage parameter space is sampled to obtain damage configurations, each

Table 1.1: Range of values associated with each damage parameter in the example ANN.

Damage Parameter	Range
n	2-6
θ: n = 2 (deg)	0-90
θ: n = 3 (deg)	0-60
θ: n = 4 (deg)	0-45
θ: n = 5 (deg)	0-36
θ: n = 6 (deg)	0-30
a (cm)	1.27-5.08
d_x (cm)	0-10.2

expressed as a combination of input parameters (n, θ, a, d_x). The space of variables can be sampled using a number of different sampling methods, including random, stratified, and Latin Hypercube [48]. Latin Hypercube Sampling (LHS) is a type of stratified sampling method that guarantees each partition, or stratum, of input variable space is sampled, though not necessarily uniformly. In this work, LHS is performed five times for each of the variables (θ, a, and d_x). Each of the five LHS runs corresponds to a different value of n (two, ..., six cracks) and requires the number of partitions to be specified. The MATLAB® implementation for LHS is used here [49], where output is provided in the range from zero to one. Each sample value is then scaled to the respective parameter range according to Table 1.1.

Table 1.2 shows all damage configurations (26 in total) that are modeled in the ISP ANN example, where each configuration is expressed in terms of sampled input parameters. For each damage configuration, the x and y dimensions of the square, damage-containing, solid FE region are provided in the sixth col-

umn. The x and y dimensions are each 25% larger than the diameter of the star-shaped damage (i.e. $1.25 * 2a$), as suggested by the supplementary shell-solid boundary effect study described above. The last column specifies whether or not the solid, damaged region severs the middle stiffener. If so, the portion of the stiffener that intersects the solid model region is removed; otherwise the stiffener remains intact.

1.2.2 Target Output: Residual Strength from Numerical Fracture Simulations

For each input damage configuration, a numerical fracture simulation is employed to determine residual strength, which provides target output used to train and test the ANN. FRANC3D/NG [50] is used to insert each parameterized star-shaped crack configuration into the solid FE region of each panel. An ABAQUS® contact algorithm is employed to prevent crack surfaces from overlapping during the applied loading. Contact properties are defined as frictionless in the tangential direction with "hard" pressure-overclosure behavior normal to the contacting crack surfaces, which minimizes interpenetration. The FE models are then analyzed using ABAQUS®, and FE analysis results are post-processed to determine residual strength.

For the sake of illustrating the ANN methodology, two simplifying assumptions are made here to predict residual strength of the ISPs. First, the ISPs remain linear-elastic and can be analyzed using LEFM parameters (SIFs). Second,

Table 1.2: Damage configurations modeled in the ISP ANN example. Each damage configuration is assigned an alphanumeric identification with number corresponding to n. The sixth column provides x and y dimensions of the square region in the shell-solid ISP.

Damage configuration ID	a **(cm)**	d_x **(cm)**	θ **(deg)**	n	**Solid region *x,y* dimensions (cm)**	**Severs stiffener?**
2A	3.8	7.1	21.8	2	9.39	NO
2B	4.2	2.1	87.8	2	10.48	YES
2C	3.0	3.6	2.2	2	7.53	YES
2D	1.4	0.2	35.7	2	3.49	YES
2E	2.3	9.9	36.5	2	5.66	NO
2F	4.5	6.1	44.9	2	11.25	NO
3A	3.7	8.3	5.0	3	9.36	NO
3B	1.5	0.6	25.2	3	3.72	YES
3C	2.9	9.6	23.2	3	7.15	NO
3D	4.0	3.7	32.9	3	9.88	YES
3E	4.6	1.7	10.4	3	11.56	YES
3F	2.0	6.3	38.6	3	4.92	NO
4A	1.7	6.5	6.6	4	4.15	NO
4B	3.4	1.7	18.7	4	8.60	YES
4C	4.9	9.7	25.1	4	12.3	NO
4D	2.1	4.4	27.0	4	5.37	NO
4E	3.0	7.0	14.9	4	7.52	NO
5A	3.3	8.2	4.8	5	8.30	NO
5B	2.2	0.8	6.9	5	5.43	YES
5C	1.5	5.4	19.8	5	3.84	NO
5D	3.2	9.4	22.6	5	7.91	NO
6A	1.8	8.3	5.4	6	4.50	NO
6B	3.7	9.7	26.5	6	9.21	NO
6C	4.9	6.0	12.2	6	12.20	NO
6D	4.2	2.0	18.4	6	10.61	YES
6E	3.0	3.5	21.9	6	7.54	YES

the residual strength can be predicted for a static crack configuration (i.e. crack growth is not modeled in this example).

In the ISP ANN example, the LEFM approximation of residual strength is based on mixed-mode I/II fracture criteria [23, 25] to account for local mode mixity (in-plane) of angled cracks in the star-shaped damage array. In [51], Broek described a practical mixed-mode I/II failure envelope, approximated by the equation of an ellipse:

$$(K_I/K_{Ic})^2 + (K_{II}/K_{IIc})^2 = 1, \tag{1.1}$$

where K_I and K_{II} are the mode I and mode II plane-strain stress intensity factors and K_{Ic} and K_{IIc} are the mode I and mode II fracture toughness values. For the AA 2*XXX* series material in the ISP example, $K_{Ic} = 32$ MPa $\sqrt{m}$, and K_{IIc} is assumed to be 10% less than K_{Ic} after results from the strain energy density criterion presented by Sih [25].

Using this mixed-mode LEFM-based approximation, residual strength is defined here as the applied traction load, Fig. 1.2, that first causes unstable crack growth for any point along any crack front of the star-shaped damage configuration. In other words, as soon as one point along one crack front reaches a critical combination $(K_I, K_{II})_c$ on the elliptical failure envelope, the entire panel is assumed to fail. The method for determining the residual strength for each damaged panel is shown in Fig. 1.4 and proceeds as follows: (1) analyze the ISP FE model with applied traction, P; (2) compute K_I and K_{II} at each node along each crack front using FRANC3D/NG; (3) *for each crack front node*, find the intersection point $(K_I, K_{II})_c$ of the elliptical failure envelope with a straight line from the origin to the computed (K_I, K_{II}) and subsequently find the linear scaling factor, λ, that maps (K_I, K_{II}) to $(K_I, K_{II})_c$; (4) of all the computed scaling factors, select the most critical, λ_c; (5) calculate the maximum-allowable load or

residual strength, P_{max}, as P scaled by λ_c.

To ensure that nonlinearity due to crack face contact does not invalidate the linear load scaling approach described above, each of the damaged ISPs is reanalyzed with the respective scaled load, i.e. the approximated residual strength. In all cases, $(K_I, K_{II}) = (K_I, K_{II})_c$ at the predicted crack front failure point, indicating that the scaled loads indeed correspond to failure loads according to the LEFM-based failure criterion assumed for this example problem. Values of P_{max} provide the target outputs used to train the ANN.

1.2.3 Neural Network Construction

The inputs (sampled damage parameters) and target outputs (residual strength predictions from numerical fracture simulations) are used to train and test an ANN. For the ISP example, a feedforward ANN with a backpropagation learning rule [32, 52], which is a commonly used type of supervised ANN, is constructed using MATLAB® [49]. The ANN consists of a single hidden layer mapping the four-parameter input vectors (n, θ, a, d_x) to the single-valued outputs (P_{max}). The reader is referred to [52] for a general discussion on ANNs and details regarding specific implementation of the transfer functions and training algorithm described next. A tan-sigmoid transfer function is employed to map the weighted inputs plus bias to the interval (-1,1). A linear transfer function then proportionally maps the weighted results plus bias from the hidden layer to the output layer. Data presented to the ANN is divided into three sets—training, validation, and test. Weights and biases of the ANN are adjusted at each iteration, or epoch, using the training set and a Levenberg-Marquardt op-

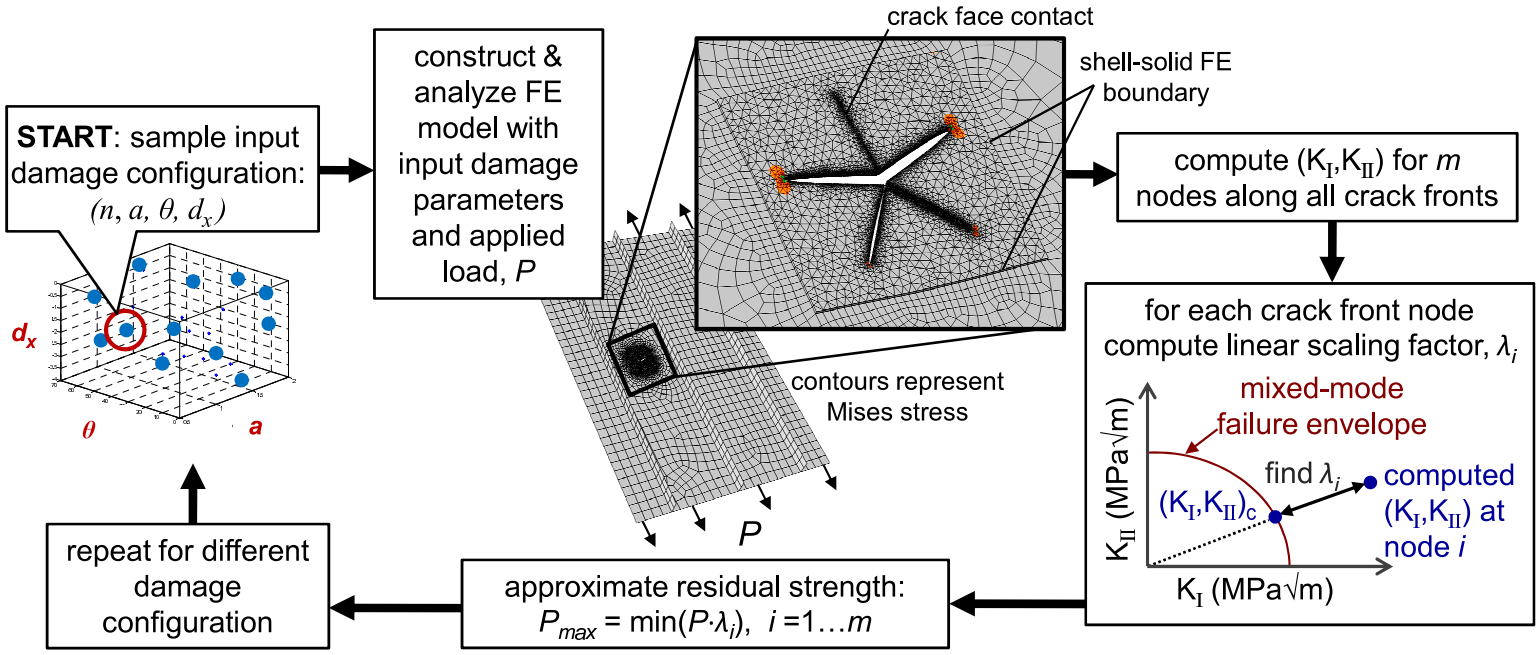

Figure 1.4: LEFM-based procedure for approximating residual strength of the damaged ISPs in the ANN example.

timization algorithm, as described in [53]. The algorithm seeks to improve performance of the ANN by minimizing error between the ANN outputs and the target outputs. Weights and biases from training at any epoch are then used to check performance of the ANN using the validation and test sets. The validation set prevents overtraining of the ANN by ceasing training if performance degrades over a certain number of successive epochs. The test set is not used for training but is used to test ANN accuracy following the current training epoch. The ANN performance metric used here is the mean squared error (MSE), calculated as:

$$MSE^{(i)} = \frac{1}{Q^{(i)}} \sum_{k=1}^{Q^{(i)}} (t_k^{(i)} - p_k)^2, \tag{1.2}$$

where the superscript *(i)* corresponds to the training, validation, or test set, Q is the number of data points in the respective set, t_k is target output for the k^{th} input, and p_k is output predicted by the ANN for the same k^{th} input.

The ANN can be optimized by adjusting any number of parameters, including transfer functions between layers, number of hidden layers, various performance metrics, and so forth. In the ISP example, the ANN is optimized by varying the number of neurons in the hidden layer (4,5,6) and by increasing size of the training set from 60%, to 70%, to 80% of the available data (with the balance equally divided between validation and test sets). Further, the performance metrics are optimized by minimizing MSE for the training and testing sets and by specifying that the correlation coefficient between ANN output and targets should be at least 0.95 over the entire data set.

1.2.4 Parametric Sensitivity Studies

The trained ANN is then employed to conduct parametric sensitivity studies, whereby sensitivity of residual strength to each postulated damage parameter is gauged. The sensitivity studies are carried out for configuration 4E, Table 1.2, as it represents an average damage configuration in terms of n, a, and d_x as compared to the other configurations.

A sensitivity study is carried out for each of the four damage parameters. In each study, three damage parameters of configuration 4E are held constant while one is varied. The variable parameter in each study takes values in the range of the corresponding variable on which the ANN was trained. For example, the longest a considered in the sensitivity study is no longer than the longest a used to train the ANN, which is $a = 4.9$ cm in the ISP example (damage configurations 4C and 6C). Further, the variable parameter takes values that are equally incremented within the respective range. Results from the study are presented in the following subsection.

1.2.5 Results and Discussion from Neural Network Example

Table 1.3 shows the approximated residual strength values of all damaged ISPs based on numerical fracture analyses and LEFM assumptions outlined in 1.2.2. The table is sorted in order of increasing residual strength, and the most influential damage parameters as determined from the sensitivity study are provided to help draw preliminary conclusions. One immediate observation is that panels with severed stiffeners have lower ($\approx 50 - 80$ MPa) residual strengths, as ex-

pected. The single exception is damage configuration 2B. Though it severs the stiffener, configuration 2B is less critical than all other stiffener-severing cases and some intact-stiffener cases because it is an $n = 2$ configuration (straight crack) aligned with the loading direction. Overall, the correlation between severed stiffener and reduced residual strength highlights the effect of the load carrying stiffener on crack criticality.

The ISPs with the lowest computed residual strength (configuration 3D) and highest computed residual strength (configuration 5C) are presented in Fig. 1.5. Each ISP is depicted with its respective residual strength, or failure load, applied. The predicted point of first-failure lies along the crack front indicated. Configuration 5C has *more* cracks and is 62.5% smaller than configuration 3D, though it is not the smallest of all configurations. More importantly, configuration 5C leaves the stiffener intact while configuration 3D results in a severed stiffener. For configuration 3D, the crack front that lies within the severed region and near the geometric discontinuity of the stiffener junction is subjected to higher stresses and is predicted to be critical.

The optimal ANN consists of four neurons in a single hidden layer with 80% of available data (i.e. twenty damage configurations) allocated to training. ANN performance metric (MSE) as a function of training epochs is plotted in Fig. 1.6 for training, validation, and test sets. The ANN is best trained at epoch 141, beyond which the MSE in the validation set continually increases and overtraining is said to occur. At this epoch, MSE of the three sets are $MSE^{train} = 0.001$, $MSE^{val} = 0.87$, and $MSE^{test} = 0.30$. Weights and biases connecting the input layer (damage parameters) to the hidden layer and the hidden layer to the out-

Table 1.3: LEFM-based residual strength approximations for all damage configurations considered in the ISP example, sorted by increasing residual strength.

Damage configuration ID	a **(cm)**	d_x **(cm)**	**Severs stiffener?**	P_{max} **(MPa)**
3D	4.0	3.7	YES	54.2
6D	4.2	2.0	YES	56.8
3E	4.6	1.7	YES	56.8
4B	3.4	1.7	YES	58.1
6E	3.0	3.5	YES	63.5
2C	3.0	3.6	YES	67.6
5B	2.2	0.8	YES	71.2
3B	1.5	0.6	YES	73.8
2D	1.4	0.2	YES	80.7
6C	4.9	6.0	NO	82.7
4C	4.9	9.7	NO	83.9
2A	3.8	7.1	NO	89.1
3A	3.7	8.3	NO	90.3
2B	4.2	2.1	YES	93.8
5A	3.3	8.2	NO	94.3
4E	3.0	7.0	NO	98.4
5D	3.2	9.4	NO	101.5
2F	4.5	6.1	NO	102.1
6B	3.7	9.7	NO	109.2
3C	2.9	9.6	NO	110.2
4A	1.7	6.5	NO	124.9
3F	2.0	6.3	NO	128.2
2E	2.3	9.9	NO	129.5
6A	1.8	8.3	NO	130.7
4D	2.1	4.4	NO	132.8
5C	1.5	5.4	NO	146.7

put layer (residual strength) at training epoch 141 are presented in Tables 1.4 and 1.5.

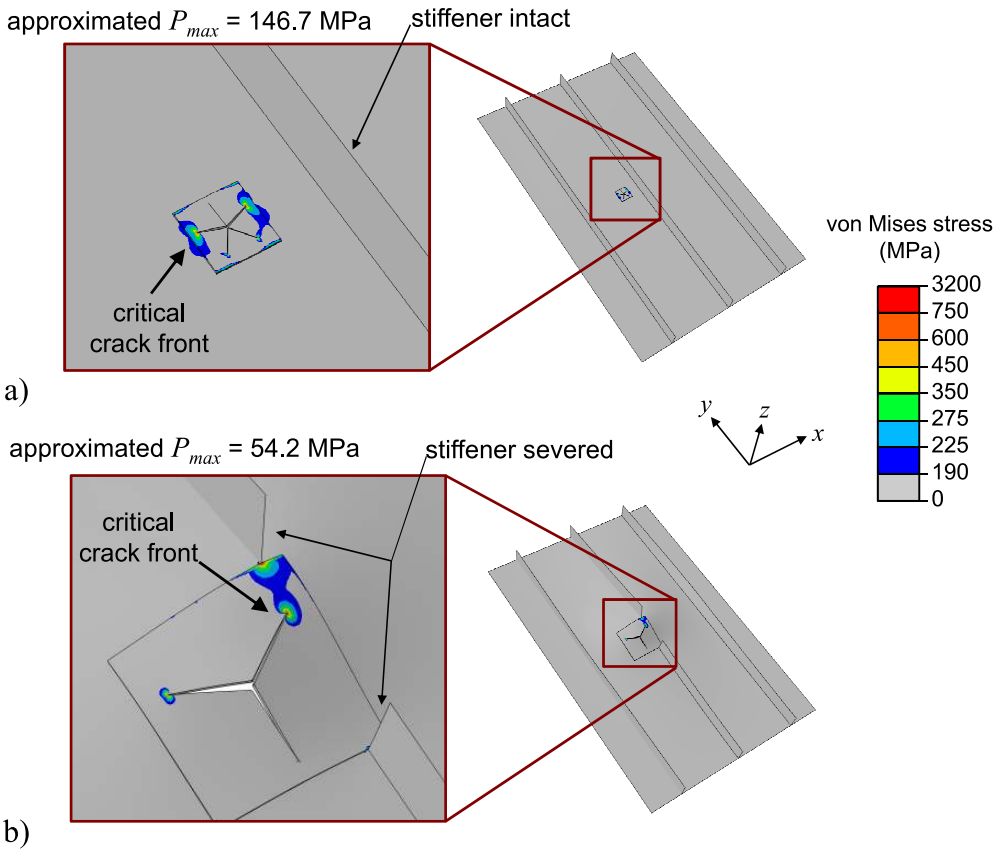

Figure 1.5: Two different damaged panels (ID 5C and ID 3D) shown with respective P_{max} applied. Panels represent damage configurations that are least critical (a) and most critical (b) of all configurations considered. Predicted failure point lies along the indicated crack front. Deformation is scaled by factor of 10. FE mesh is not shown for better contour visualization.

Considering the entire set of damage configurations, the ANN predictions correlate well with the target outputs at epoch 141, as depicted in Fig. 1.6. Despite the good overall correlation and small MSE for the training set, the MSE in the validation and testing sets (which include only three damage configurations each) may be too large for actual implementation onboard an aircraft. It is suspected that adding more samples to the entire set of damaged ISPs would

further reduce these errors in the ANN.

The influence of each damage parameter on predicted residual strength can

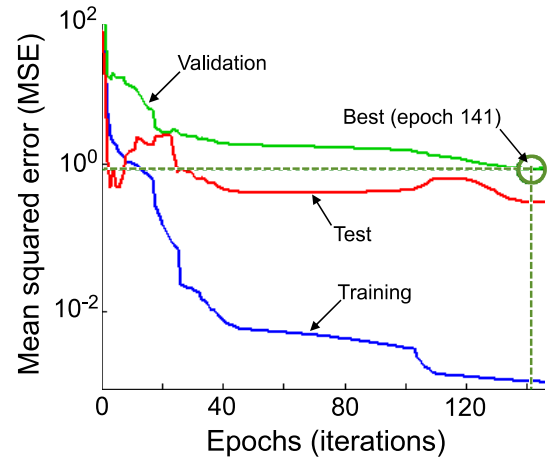

a)

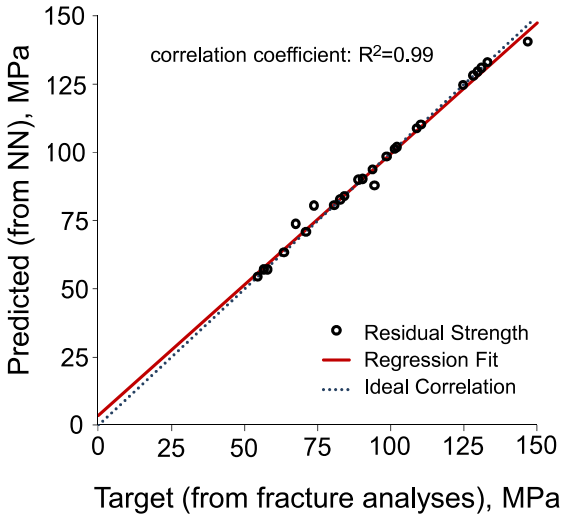

b)

Figure 1.6: (a) ANN performance as a function of training epochs for the optimized ANN; overtraining occurs after epoch 141. (b) Correlation between predicted and target residual strength values considering all damage configurations.

Table 1.4: ANN weights and biases used to map input layer to hidden layer for the optimized ANN at training epoch 141.

	Input	Hidden layer neuron			
		1	2	3	4
Weights	n	-0.43	-2.98	-1.11	1.83
	a	0.69	-9.17	1.61	-2.27
	d_x	3.58	-0.15	1.50	-8.74
	θ	-1.53	2.87	-2.96	5.58
Biases		-0.42	0.45	1.37	2.94

Table 1.5: ANN weights and bias used to map hidden layer to output for the optimized ANN at training epoch 141.

	Hidden layer neuron	Output
Weights	1	0.78
	2	0.25
	3	-1.70
	4	1.05
Bias		1.29

be visualized graphically by plotting predicted residual strength as a function of each damage parameter (see Fig. 1.7). Sensitivity can be quantified by a number of different metrics, many of which yield comparable results [54]. Here, sensitivity is quantified by the correlation coefficient c_v, expressed as a percentage:

$$c_v = \frac{\sigma}{\bar{P}_{max}}, \text{ where } \sigma = \sqrt{\frac{\sum_{i=1}^{N}(P_{max,i} - \bar{P}_{max})^2}{N-1}}. \tag{1.3}$$

For any given sensitivity subset, i corresponds to the i^{th} sample configuration, $\bar{P}_{max}$ is the average residual strength of the subset, and N is the total number of damage configurations in the respective subset. Sensitivities to each damage pa-

rameter are calculated as $c_v^{(d_x)} = 24.8\%$, $c_v^{(a)} = 16.6\%$, $c_v^{(n)} = 6.0\%$, and $c_v^{(\theta)} = 1.2\%$.

Orientation and number of cracks are found to have relatively minor influences on predicted residual strength, which is apparent both by their sensitivity metrics and by the plots (b) and (d) of Fig. 1.7. Crack length, on the other hand, has a more significant influence and causes a reduction in predicted residual strength as crack length increases, which is expected. What is unexpected, however, is the step-like behavior depicted in Fig. 1.7(c). This behavior is caused by binary modeling of the stiffener (explicitly modeling as severed or intact), a feature that is inherently implicit in both crack size and location. The stiffener effect is also apparent in Fig. 1.7(a) of damage location sensitivity. Predicted residual strength is lowest (and relatively insensitive to damage location) if the damage is located such that it severs the stiffener. As the damage location moves away from the stiffener and is no longer severing it, there is a linear increase in residual strength until the damage is located within the middle quarter of the bay.

In general, the importance of this kind of sensitivity study is (1) to gain a better intuition of how and why certain damage characteristics influence residual strength and (2) to potentially decrease the dimensionality of the ANN by neglecting parameters deemed insignificant.

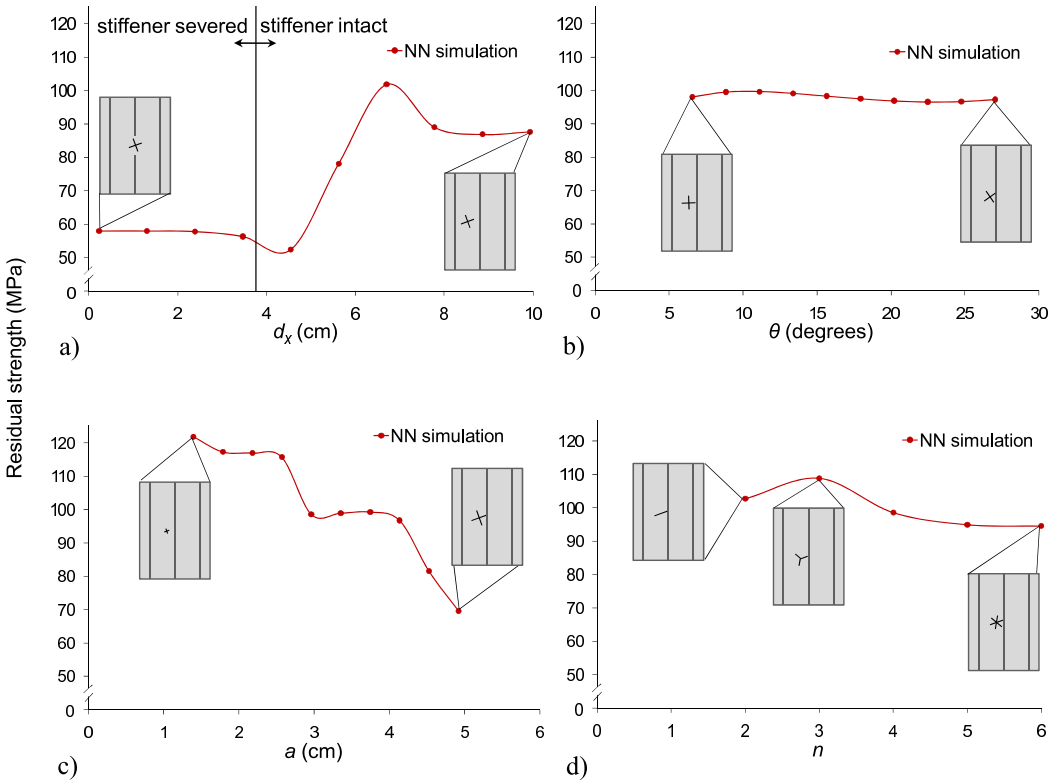

Figure 1.7: Sensitivity of predicted residual strength to each damage parameter.

1.3 3-D Elastic-plastic Fracture Simulations for Improved Neural Network Training

For discrete-source damage cases involving significant ductile tearing, a generally applicable 3-D EPFM framework should be used for improving residual strength training data. An elastic-plastic crack growth simulation procedure, as implemented in this section, is illustrated in Fig. 1.8 and proceeds as follows:

1. define an uncracked FE model and boundary conditions;
2. extract a sub-region of the mesh for crack insertion, remeshing, and recon-

nection with the global mesh;

3. map previous deformation and material state onto the remeshed model;
4. perform nonlinear FE analysis and monitor the crack growth criterion;
5. once criterion is satisfied, stop the current FE analysis to update crack configuration, remesh sub-region, and reconnect sub-region mesh with global mesh;
6. repeat from step 3 until critical crack length is achieved or until residual strength is attained.

The simulation procedure allows for prediction of curvilinear crack paths and arbitrary crack front evolution. The EPFM framework was overviewed in [4] and is described here for completeness. Additional details of the framework, including scripts used for implementation, are found in [2].

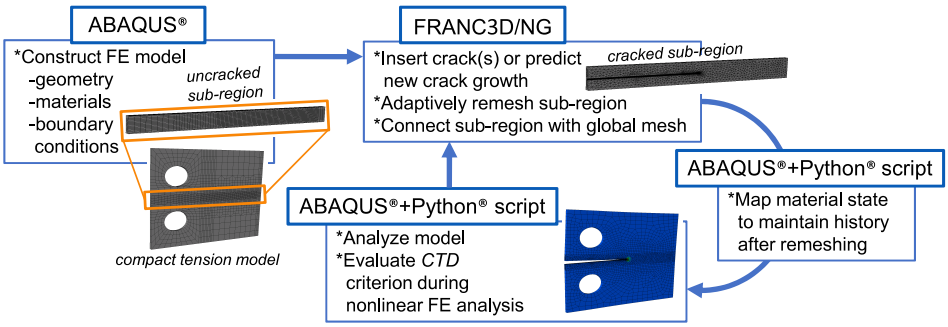

Figure 1.8: Elastic-plastic crack growth simulation algorithm using FRANC3D/NG.

1.3.1 Nonlinear Fracture Parameter: Crack-tip Displacement

In elastic-plastic tearing simulations, especially of thin metallic structures, crack growth should be characterized by an appropriate nonlinear parameter. Wells first suggested the crack-tip opening displacement ($CTOD$) as a potential parameter for characterizing elastic-plastic crack growth [55]. Later, Andersson [56] and de Koning [57] introduced the crack-tip opening angle ($CTOA$). Both parameters correlate impending crack growth to some critical amount of opening behind the crack tip. The results of a round-robin organized in 1979 by the ASTM Committee E-24 indicated that, of several proposed methods for predicting failure loads of various metallic fracture specimens, $CTOA$ (or an equivalent $CTOD$) was the most suitable [58]. Since then, many have continued to experimentally observe and numerically implement $CTOA$ and $CTOD$ as criteria for elastic-plastic crack growth (see [59] for a complete review of the criteria). A noted feature of these criteria is that a critical value calibrated for a specific material and thickness is applicable over a range of structural configurations comprising the same material and thickness under similar loading.

A criterion based on this parameter, which is called the crack-tip displacement (CTD) or sometimes referred to as the generalized crack (tip) opening displacement [29, 60], is implemented here. In this work, CTD is computed as:

$$CTD = \sqrt{{CTD_I}^2 + {CTD_{II}}^2 + {CTD_{III}}^2} \tag{1.4a}$$

$$CTD_I = v_1 - v_2 \tag{1.4b}$$

$$CTD_{II} = u_1 - u_2 \tag{1.4c}$$

$$CTD_{III} = w_1 - w_2, \tag{1.4d}$$

where u, v, and w correspond to displacements in the x, y, and z directions, respectively, and subscripts 1 and 2 denote the two points used to compute CTD. CTD is computed between two points that are initially coincident (one on each crack face) on the undeformed crack surface at a distance, d, behind the crack front node (i.e. in the direction normal to the crack front at the particular crack front node). This is illustrated schematically in 2D in Fig. 1.9. In 3D, CTD values are computed behind multiple crack front nodes. The pair of initially coincident points where CTD is calculated is called a CTD point. Element shape functions are used to interpolate displacements (u, v, w) such that the CTD points need not correspond to nodal locations.

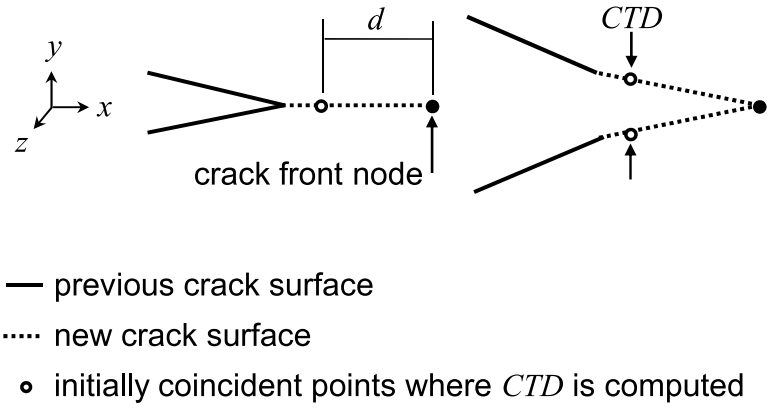

Figure 1.9: Simplified schematic of CTD implementation illustrated on crack profile.

Crack growth occurs when CTD attains a critical value, CTD_{crit}, within a specified tolerance. There are several ways to evaluate the CTD criterion when modeling a 3-D crack front, including evaluation at a single CTD point either mid-

way along the crack front or on the specimen's free surface. Alternatively, the CTD criterion may be evaluated by comparing CTD_{crit} to an average CTD value calculated for multiple CTD points. Because CTD_{crit} is known to depend on 3-D constraint at any point along a crack front, using a single CTD_{crit} to predict the advance of an entire crack front might not be valid for all cases. A more rigorous and computationally expensive evaluation technique would be to compare CTD at each CTD point to a constraint-dependent CTD_{crit}. While some work has been done to resolve a relationship between 3-D constraint and CTD_{crit} [61, 27], a constraint-dependent fracture criterion is not evaluated in the simulation described here.

1.3.2 Material State Mapping Algorithm

Following crack growth and remeshing, state variables are mapped from the previous mesh to the current mesh using an inverse isoparametric mapping routine, as in [62]. Lim et al. described the inverse isoparametric mapping technique for 2D elastic-plastic fracture simulations [63]. Implementation of the mapping algorithm consists of two high-level steps: (1) in the (n) mesh, state variables stored at integration points are extrapolated to nodes using element shape functions, and (2) displacements and state variables are transferred to either nodes or integration points in the $(n+1)$ mesh. The second step involves finding, for each point in the $(n+1)$ mesh, the natural coordinates (ξ, η) of that point with respect to the element from the undeformed (n) mesh in which that point would spatially reside. The inverse problem becomes finding the natural coordinates (ξ, η) that satisfy the known global coordinates:

$$X^{(n+1)} = \Sigma N_i(\xi, \eta) X_i^{(n)}, \tag{1.5}$$

where the subscript i ranges from one to the number of element nodes, $X^{(n)}$ are global nodal coordinates in the (n) mesh, $X^{(n+1)}$ are point or nodal coordinates in the $(n+1)$ mesh, and N are element shape functions evaluated at (ξ, η). Once (ξ, η) are known, nodal displacements and state variables, U, can be transferred from the (n) mesh to the $(n + 1)$ mesh in a forward manner, again using the element shape functions, N:

$$U^{(n+1)} = \Sigma N_i(\xi, \eta) U_i^{(n)}. \tag{1.6}$$

Two levels of mapping are incorporated into the extended FRANC3D/NG and ABAQUS® software framework. First, displacements are mapped onto the undeformed mesh following crack growth and remeshing. Second, a mapping function available in ABAQUS® is invoked to map the remaining state variables (e.g. stress, strain, plastic strain) onto the deformed mesh. When mapping material state between successive cracked configurations, it is critical that mesh refinement in regions of high gradients (e.g. near crack fronts) is sufficient to minimize solution diffusion, which occurs as a result of extrapolation, interpolation, and nodal averaging (if employed). This effect can become compounded as the crack growth simulation continues. After growing the crack and remeshing, the updated mesh model contains additional surface area due to crack extension, and equilibrium must be re-established before additional load is applied. During the equilibration procedure, global boundaries are held fixed and the new, traction-free crack surfaces are allowed to displace in response to surrounding fields, as shown in Fig. 1.10.

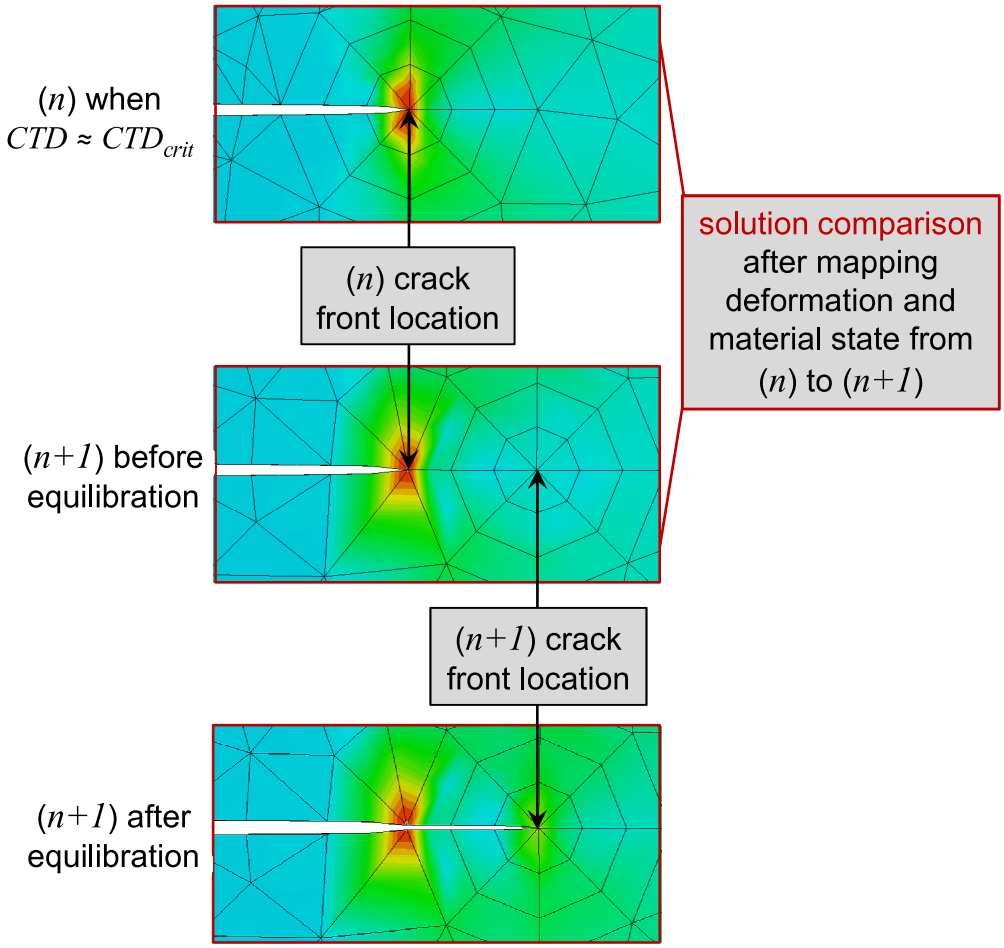

Figure 1.10: Qualitative comparison of deformation and equivalent plastic strain field after mapping and subsequent equilibration. Images show face of 3-D mesh.

1.3.3 Validation Simulations

Two stable-tearing experiments are simulated to validate the EPFM framework for predicting crack growth and residual strength of relatively thin metallic structures. To illustrate the necessity of using an EPFM framework for predicting crack propagation and residual strength in such cases, the experiments are

also simulated using an LEFM-based methodology. In the LEFM simulations, the material is modeled as linear-elastic, and crack growth is assumed to occur when an average value of K_I (and K_{II} for mixed-mode crack growth) along a crack front approximately equals fracture toughness of the material for any increment of crack length.

Arcan Specimen

A (modified) mixed-mode I/II Arcan fracture test [64] is simulated. Experimental details and results were provided in [65] and [66]. Drawings of the fracture specimen and modified load fixture are shown in Fig. 1.11. Curvilinear crack growth was induced in an AA 2024-T3 fracture specimen by applying monotonic load at a 30° angle relative to the fatigue precrack plane, as depicted in Fig. 1.11.

The FE model of the load fixture and fracture specimen is constructed using ABAQUS® and is depicted in Fig. 1.12. The FE model contains an initial crack of length 6.35 mm and does not simulate the fatigue precracking process. A mesh refinement study is first conducted by simulating a pure mode I Arcan test (0° loading angle). Results from the study reveal that, for the initial crack, the applied load at CTD_{crit} varies by less than 0.25% when the element length nearest the crack front is 0.33 mm or smaller. This converged level of mesh refinement is used for the mixed-mode Arcan model presented here (30° loading angle). The specimen and fixture are assumed to be perfectly bonded such that coincident nodes are merged at the specimen-fixture interface. The fixture is modeled using 6000 quadratic tetrahedral elements and remains unchanged

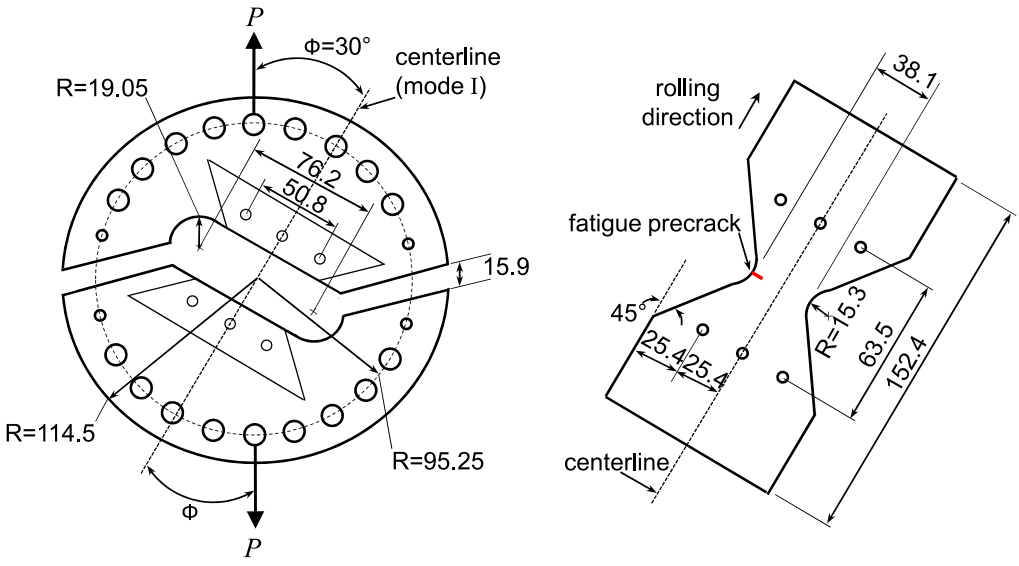

Figure 1.11: Schematic of Arcan test fixture (left) and 2.3 mm thick fracture specimen (right). Load, P, can be applied at different pinholes in the fixture to induce mode I/II crack growth in the specimen. Drawings not to scale. All length dimensions in mm.

throughout the simulation. The fracture specimen sub-region is subject to geometry and mesh updating within FRANC3D/NG. Depending on the crack length, the specimen comprises between 9000 and 25,000 quadratic elements, which include a standard rosette of quadratic-wedge, quadratic-brick, and quadratic collapsed-brick (pyramid) elements surrounding the crack front (see [50] for details). The bulk of the sub-region mesh comprises quadratic tetrahedral elements.

Material properties for the 15-5PH stainless steel fixture are $E = 207$ GPa and $\nu = 0.3$. The fixture is assumed to remain elastic during loading. Material properties for the AA 2024-T3 fracture specimen are $E = 71.4$ GPa, $\nu = 0.33$, and yield strength $\sigma_y = 345$ MPa. The strain hardening curve for the specimen is

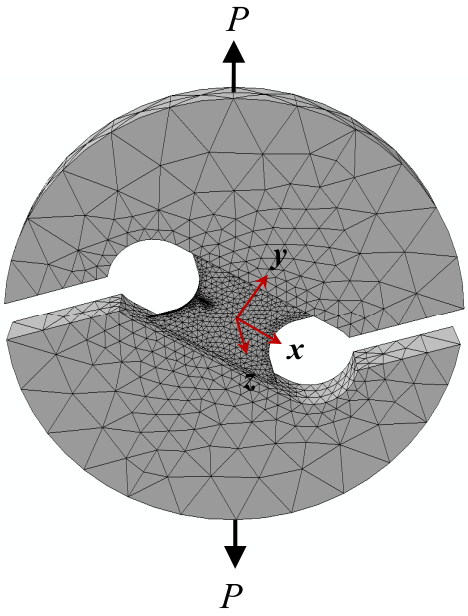

Figure 1.12: 3-D FE model of modified Arcan test set-up, including load fixture and fracture specimen. Line traction, P, is applied at 30° from mode I axis (y-axis).

provided in Fig. 1.13. A von Mises yield criterion with isotropic hardening is assumed. For the LEFM simulation, the specimen is modeled as linear-elastic with K_{Ic} = 37 MPa $\sqrt{m}$ for AA 2024-T3 in the LT orientation [67].

Crack growth occurs in the LEFM simulation when the average (K_I, K_{II}) along the crack front reaches a critical combination. The critical combination is determined using the mixed-mode failure envelope described in 1.2.2, where K_{IIc} is taken to be 10% less than K_{Ic}.

In the EPFM simulation, important observations from a number of studies inform the selection of CTD_{crit} and d used to predict crack growth. First, from [13, 65, 66], for 2.3 mm thick AA 2024-T3 specimens precracked in the L-T ori-

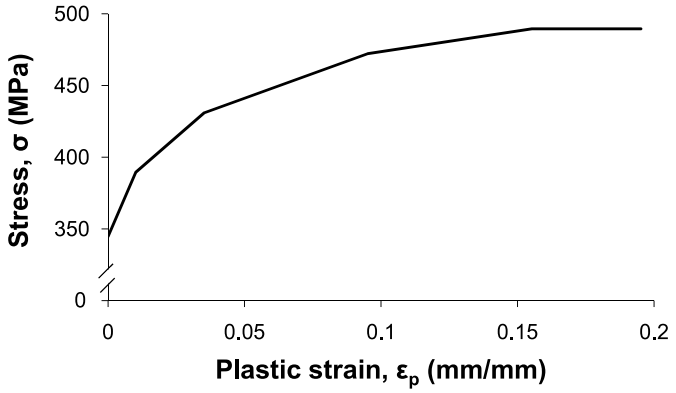

Figure 1.13: Strain hardening curve determined from uniaxial tension tests for AA 2024-T3 in LT orientation. Courtesy NASA Langley Research Center. Similar curves were used in [29] and [30].

entation, an average constant critical value of CTD_{crit}= 0.1 mm was observed, where CTD was measured on the specimen face at d = 1 mm. This critical value was observed for a range of specimens exhibiting mode I dominant crack growth, which includes the 30° Arcan test [65, 66]. Scatter among the measurements was typically ±0.02 mm. Second, significant crack front tunneling was observed in the fracture specimens, especially during initial crack extension [13]. Third, a recent study by Lan et al. suggested that modeling tunneled cracks using straight crack fronts can lead to over-estimation of load versus crack extension predictions [61]. This is because higher levels of constraint along a crack front, which can induce crack tunneling, effectively decrease fracture toughness. Lan et al. noted that surface-measured CTD values can be 24% larger for cases with crack tunneling than cases without. In the Arcan simulation, crack front tunneling and slant crack growth are not modeled. Thus, using the surface-measured value of CTD_{crit}= 0.1 mm from [13, 65, 66] as the crack growth criterion in the Arcan simulation, an over-prediction of load versus crack extension is expected. Assuming that the over-prediction is proportional to the difference

in surface-measured CTD_{crit} values between straight and tunneled crack fronts, CTD_{crit} is taken to be 0.08 mm, which is $\approx$ 24% less than the observed average surface-measured value of CTD_{crit}= 0.1 mm and also corresponds to the lower bound of experimental scatter. This adjusted critical value used in simulation should account for some expected over-prediction of residual strength.

Simulated crack growth occurs in increments of approximately 1 mm, which satisfies convergence results from similar simulations [29]. Propagation direction is predicted according to the maximum tangential stress theory [23], though a 2D CTD-based directional criterion [26] could also be used.

Simulation proceeds by applying displacement in the direction indicated in Fig. 1.12, which corresponds to a 30° loading angle. In the EPFM simulation, after each increment of, inclusively, crack growth, remeshing, and material state mapping (see subsection 1.3.2), all nodes with applied boundary conditions are held fixed while the model is brought into equilibrium. Then, additional displacement is applied, and the simulation continues until maximum load, or residual strength, is attained.

Applied load versus crack extension is plotted in Fig. 1.14 from the Arcan experiment and simulation. Both LEFM and EPFM simulation results are plotted. Compared to experiment, residual strength is 6.8% higher using the EPFM framework and 10.8% lower using the LEFM method. In the LEFM simulation, maximum load occurs at the first increment of crack growth; whereas, maximum load occurs in the EPFM simulation after a small amount of crack growth, consistent with experiment. The load to initiate crack extension is ap-

proximately the same in both EPFM and LEFM simulations since there are no residual stresses in the model at da=0. However, unlike the LEFM simulation, the EPFM simulation is able to capture the shape of the load versus crack extension curve. In other words, including plasticity effects in the model requires an increase in applied load, initially, to drive crack extension before reaching the residual strength of the specimen.

Although the EPFM framework captures the shape of the load versus crack extension curve, it slightly over-predicts the maximum load. The over-prediction is likely related to modeling the crack front, which tunnels or thumbnails in reality, as remaining straight throughout the simulation. Given a constraint-dependent CTD_{crit}, curvature along the crack front could be predicted using a point-by-point evaluation technique, in which case it is suspected that the load versus crack extension curve would be predicted even more accurately. Another potential contribution to the discrepancy is the numerical tolerance for satisfying CTD_{crit}, which in this case is set at 2%.

Figure 1.15 shows the simulated and experimental curvilinear crack trajectory as viewed from the specimen free surface. There is a slight deviation in the actual crack trajectory during the first 6.35 mm of crack length due to fatigue precracking processes, which are not modeled in the simulation. Rather, the fatigue precrack is simply modeled as a perfectly planar initial crack in the simulation. The deviation appears to have little effect on the predicted crack path thereafter.

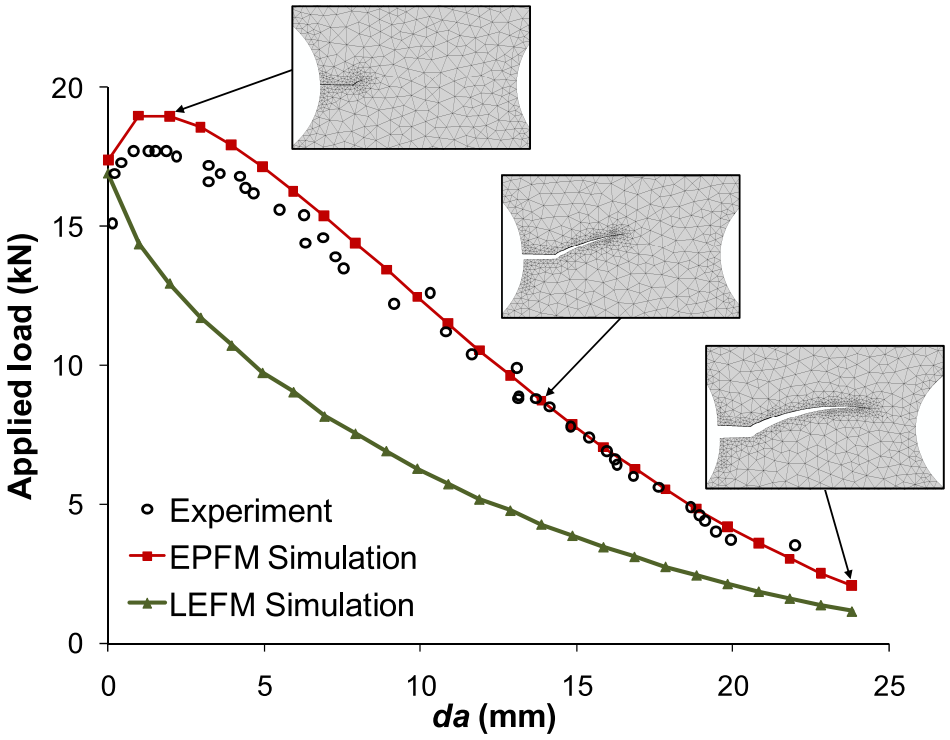

Figure 1.14: Applied load versus crack extension, *da*, from the 30° Arcan experiment and simulations. Insets show snapshots of deformed mesh at various crack increments. Complete simulation can be viewed at *www.cfg.cornell.edu*

Integrally-stiffened Panel

A stable tearing test of an ISP machined from a lower wing-skin aluminum alloy, C433-T39, is also simulated. The test was conducted at Alcoa Technical Center. Test details, data, and results were overviewed in [68] and have also been provided to the authors by Alcoa Technical Center. Relevant details are described next, and additional details from the test program can be found in A of the Appendix.

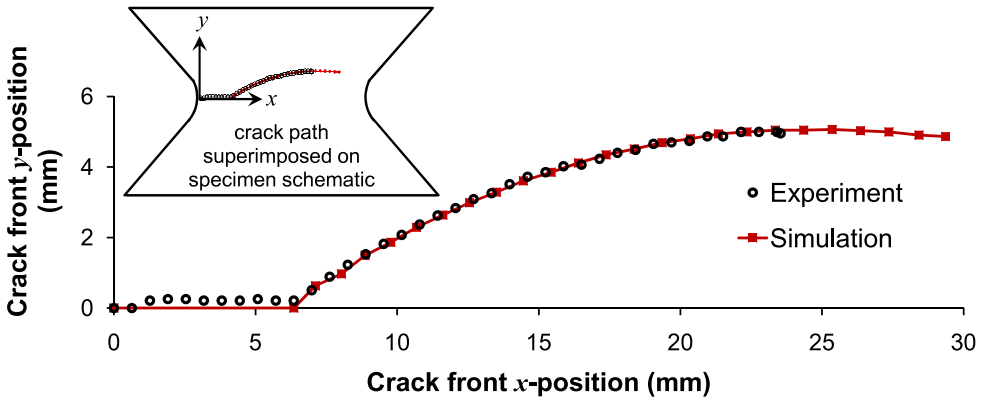

Figure 1.15: Comparison of experimental and simulated curvilinear crack paths in the 30° Arcan fracture test. Inset shows reference coordinate system.

Dimensions of the panel are shown in Fig. 1.16(a). An initial two-bay saw cut of length $\approx$ 2.54 cm was made at mid-height to completely sever the middle stiffener. The initial cut was then propagated under fatigue loading until both crack fronts were 2.54 cm short of reaching the intact stiffeners ($2a \approx$ 24.1 cm). The panel was then loaded monotonically in uniaxial tension until failure occurred by unstable crack growth. Crack front branching was observed, where an initial crack propagating toward an intact stiffener eventually split into two distinct cracks, one continuing into the adjacent bay and one propagating in the z direction within the stiffener. Photographs of the test panel with views of crack branching are provided in Fig. 1.17.

A 3-D FE model of the entire panel is constructed using ABAQUS® [46]. The FE model contains an initial crack of total length 24.1 cm, which corresponds to the fatigue crack length just prior to conducting the residual strength test. The FE model with initial crack is shown in Fig. 1.16(b). The global mesh region that remains unchanged throughout the tearing simulation is modeled us-

ing 56 and 9,400 quadratic-wedge and quadratic-brick elements, respectively. A 38.5 x 12.7 cm^2 sub-region centered in the panel is subject to geometry and mesh updating within FRANC3D/NG. The mesh interface between the sub- and global regions is coherent, obviating the enforcement of a coupling constraint.

Depending on crack length, the sub-region comprises between 27,000 and 95,000 quadratic elements, including a bulk of quadratic-tetrahedral elements and a standard rosette of quadratic-wedge, quadratic-brick, and pyramid elements surrounding the crack front (see [50] for details). Mesh refinement near each crack front is dictated, to some extent, by crack front location with respect to stiffener. As the crack initially propagates through the skin, element lengths nearest both crack fronts are 0.5 mm. When the crack fronts are within 1.5 mm of the 90° skin-stiffener junctions, however, near-crack front elements must decrease in size. This is because the rosette template of elements surrounding either crack front consists of three rings of equi-length elements. In order to accommodate (i.e. successfully mesh) a full rosette of elements within the proximity of the discontinuous geometry, the size of the template elements must decrease. The increased mesh refinement over several crack length increments, da, poses no detriment to the simulation procedure.

The thickened grip ends of the panel are modeled as linear-elastic with an elastic modulus approximately five times greater than that of C433-T39. The rest of the panel is assigned C433-T39 material properties: E = 71.4 GPa, ν = 0.3, and σ_y = 455 MPa [69]. The strain hardening curve used for C433-T39 is pro-

vided in Fig. 1.18. A von Mises yield criterion with isotropic hardening is assumed. For the LEFM simulation, the panel is modeled as linear-elastic with $K_{Ic} = 50$ MPa $\sqrt{m}$ for C433-T39 [69].

Boundary conditions are applied to simulate actual loading in the panel. Nodes on the bottom face of the lower grip end are fixed in the y direction. Displacement is applied in the y direction at nodes on the top face of the upper grip end. Additionally, nodes along the same top and bottom grip end faces are fixed in the x and z directions. For the EPFM simulation, after each increment of, inclusively, crack growth, remeshing, and material state mapping (see subsection 1.3.2), all nodes with applied boundary conditions are held fixed while the model is brought into equilibrium before applying additional displacement. Additionally, based on preliminary simulation results, the entire back (z_{min}) face is artificially fixed after mapping, during the equilibration procedure. This is because resonance in the z direction is observed with increased crack growth otherwise. The resonance occurs when mapped tensile and compressive stresses in the faces of the panel are artificially reversed during equilibration of the mapped solution. The additional boundary condition is, however, removed after the equilibration procedure so that z displacement is allowed during the subsequent loading step.

Crack growth occurs in the LEFM simulation when the average K_I value along either crack front reaches K_{Ic}. A mixed-mode failure criterion is unnecessary, as K_{II} and K_{III} are negligible (i.e. less than 2.5% of K_I for all crack growth increments).

For the EPFM simulation, CTD_{crit} was calibrated at NASA Langley Research Center from a middle-crack tension (MT) test of the same material (C433-T39) and thickness as the ISP [70]. In that work, 3-D FE simulations of the MT test revealed that simulated load versus crack extension matched experimental data when the mode I opening angle midway along the crack front at $d = 1.02$ mm reached a critical value of 6.5°. This angle corresponds to CTD_{crit} through the relation

$$tan(6.5^\circ) = \frac{CTD_{crit}}{1.02}. \tag{1.7}$$

The same criterion is applied in the EPFM simulation by specifying for both crack fronts that CTD_{crit} must attain a value of 0.116 mm at $d = 1.02$ mm behind the crack front and that the criterion be evaluated midway along either crack front.

Crack growth occurs in increments of ≈1.15 mm (about 15% of the skin thickness), which is selected to be approximately the same as that implemented by Seshadri et al. in a similar simulation [70]. Straight crack fronts are enforced during crack growth in the skin of ISP. Upon entering the intact stiffener, a crack front is evolved such that (1) a realistic, arbitrary crack front profile is represented (though the actual evolving crack front profile was not monitored during experiment) and (2) the new crack front profile has relatively smooth curvature to facilitate remeshing. A cross-section view of the panel in Fig. 1.19 shows different stages of simulated crack front evolution, from lead crack growth in the skin, to transition crack growth within the stiffener, to complete branching. The simulation proceeds as depicted in Fig. 1.8 until both initial crack fronts completely branch and P_{max} is attained.

Evaluation of the CTD criterion becomes nontrivial as a crack front transitions within the stiffener (i.e. while a crack front is within the stiffener but has not completely branched). Constraint effects introduced by the stiffener on the unsymmetric crack front profile, along with slight z displacement near the cracked region, lead to nonuniform and unsymmetric CTD values along the crack front. Evaluating the CTD criterion at only one point along the crack front becomes ambiguous to implement numerically and less representative, physically, of 3-D crack growth behavior. A simple and efficient approach to address these issues is to compare CTD_{crit} to an average of CTD values along the crack front. For transition crack growth in the stiffener, the middle third section of CTD points along the crack front are averaged and evaluated to predict crack propagation. Once the crack fully branches, the CTD criterion is again evaluated midway along each crack front.

Predicting crack front evolution for transition crack growth within the stiffener is not currently a fully-automated process. In this work, the straight portion of the crack front (see Fig. 1.19) is predicted using FRANC3D/NG and the curved portion of the front is specified by manually adding crack front points according to the two considerations described in the previous paragraph. Given a constraint-dependent CTD_{crit} relationship, a point-wise CTD criterion could be evaluated to evolve the arbitrarily-shaped crack front automatically.

The consequence of using LEFM versus EPFM simulation to determine residual strength is made clear in Fig. 1.20, which shows load versus crack extension for both LEFM and EPFM simulations. Experimental load versus crack extension

was not recorded during the tests; however, maximum applied load is plotted for two different ISP tests of the same material and loading conditions. Load required to initiate crack extension is similar using either the EPFM or LEFM method since there are no residual stresses in the model at da=0. Following initiation, however, the EPFM simulation predicts that the applied load must be increased to maintain crack propagation. The necessary increase in applied load occurs since a significant amount of energy in the system is dissipated through plastic deformation. This effect cannot be predicted by the LEFM simulation since plasticity effects are not modeled. As a result, much of the energy in the ISP for the LEFM simulation must be dissipated through creation of new fracture surface area, which means less load is required to drive crack growth in the LEFM simulation than in the EPFM simulation. Using the EPFM framework, residual strength is determined within 2% of experimental average of the two tests. On the other hand, the LEFM method underpredicts the average residual strength by 64%. Although the LEFM simulation does predict an increase in applied load at the stiffener junction due to geometrical effects, the increase is negligible compared to that due to plastic deformation.

From the EPFM simulation, equivalent plastic strain field evolution in the ISP is depicted in Fig. 1.21 for the first and final crack steps. Accumulation of plastic strain in the wakes of the advancing crack fronts is relatively significant, extending from initial to final crack front locations. The general shape of 45° contour lobes at da=0 mm is maintained at da=44 mm both for the lead crack front extending into adjacent bay and for the crack front propagating in the z direction within the stiffener. At da=44 mm, the equivalent plastic strain in each stiffener extends in the direction of both contour lobes to the stiffener boundary.

The consistent contour lobe shapes indicate that, despite increased z displacement as the crack propagates and severs initially-intact stiffeners, both lead and branched crack fronts remain locally mode I dominant throughout tearing.

Finally, as evident in Fig. 1.21 for da=44 mm, the mapping procedure inevitably leads to imperfections in the fields due to diffusion of the FE solution, which occurs in regions of high gradients from repeated extrapolation and interpolation procedures, see 1.3.2. If mapping errors significantly affect crack growth predictions, mesh refinement should mitigate this effect.

1.4 Conclusions

A surrogate model methodology and 3-D elastic-plastic fracture simulation toolset have been presented, which enable accurate residual strength prediction of damaged structures in real time. The methodology and toolset are particularly useful for scenarios involving metallic aircraft structures subject to discrete-source damage during flight. An accurate prediction of structural residual strength in these scenarios could aid in avoidance of catastrophic crack growth and subsequent structural failure.

The surrogate model methodology relies on offline numerical fracture simulations to obtain a set of data points describing residual strength as a function of discrete-source damage parameters. Strictly for illustration, an ANN has been constructed as a surrogate model for predicting residual strength of a representative wing sub-structure subject to discrete-source damage. In the illustra-

tion, offline residual strength values have been determined using computationally efficient linear-elastic fracture mechanics (LEFM) approximations. We have subsequently shown the consequences of using LEFM approximations for determining residual strength of damaged metallic structures and have described an elastic-plastic fracture mechanics (EPFM) framework to accurately determine residual strength using high-fidelity, 3-D, elastic-plastic tearing simulations. For an aluminum-alloy integrally-stiffened panel exhibiting crack branching, residual strength is predicted within 2% of experiment using an EPFM simulation and is underpredicted by 64% using an LEFM simulation.

The more general and rigorous elastic-plastic tearing framework should be used to generate accurate residual strength training data, especially for cases involving discrete-source damage. Also, the FE model for the structure of interest should include enough detail to fully capture the relationship between a particular global loading state and onset of unstable crack growth. Furthermore, damage should be parameterized by taking into account onboard sensor characterization capability and resolution. With these considerations in mind, the general surrogate model methodology coupled with the EPFM simulation framework presented in this work provides a means of achieving more resilient and adaptive aircraft control.

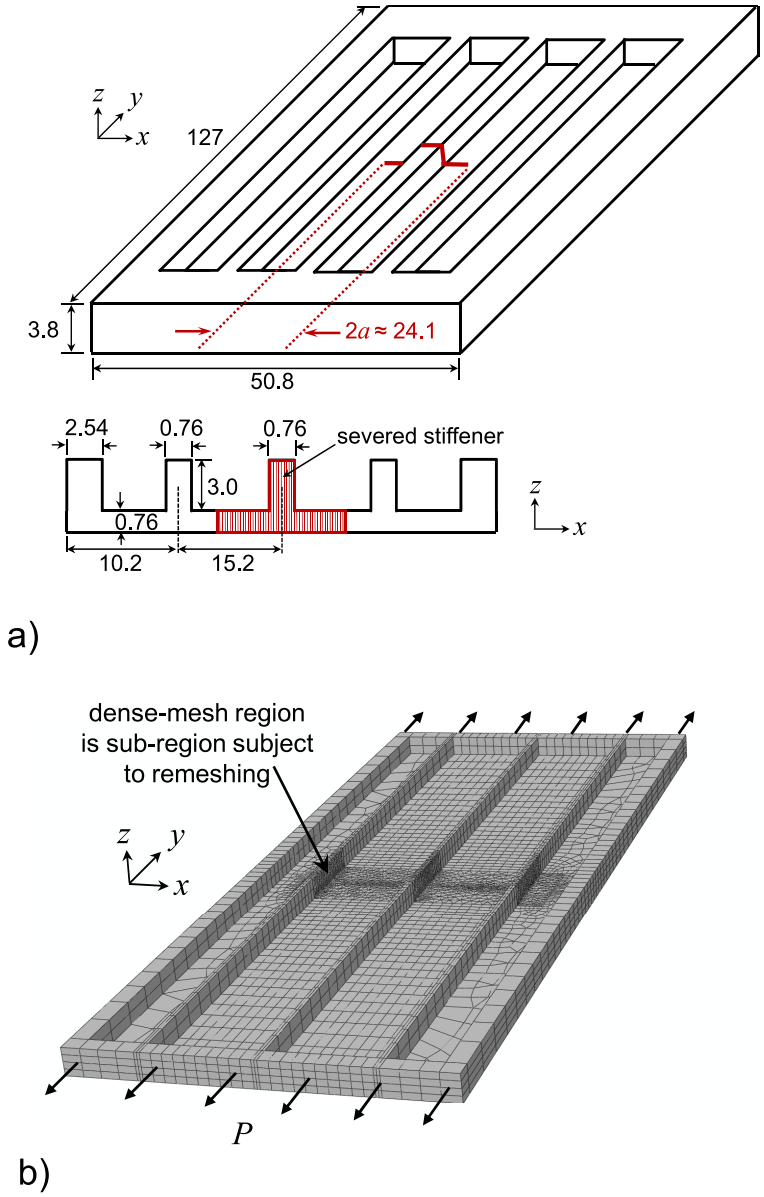

Figure 1.16: (a) Schematic (not to scale) from [68] showing dimensions of symmetric ISP tested at Alcoa Technical Center. Isoparametric view of full panel (top) indicates fatigue crack length $2a$ prior to residual strength test. Cross-section view (bottom) is shown in the plane of the severed stiffener. All dimensions are in cm. (b) Corresponding 3-D FE model of ISP. Initial crack severs middle stiffener. Traction, P, is applied uniaxially in the y direction.

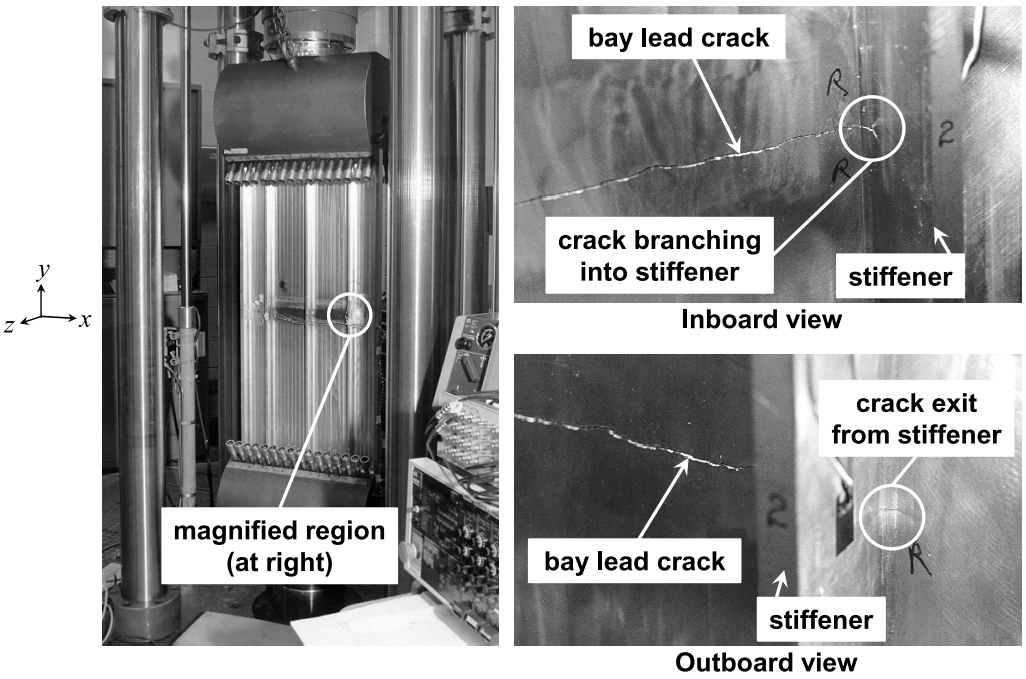

Figure 1.17: Photographs of ISP with central two-bay crack from the Alcoa test program [68]. Full panel in load frame (left) and angled views of crack front branching into stiffener (top right) then exiting the stiffener (bottom right).

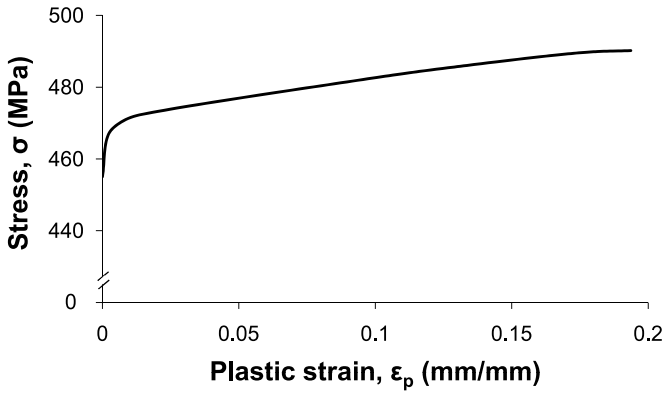

Figure 1.18: Strain hardening curve determined from uniaxial tension tests for C433-T39 in LT orientation [68].

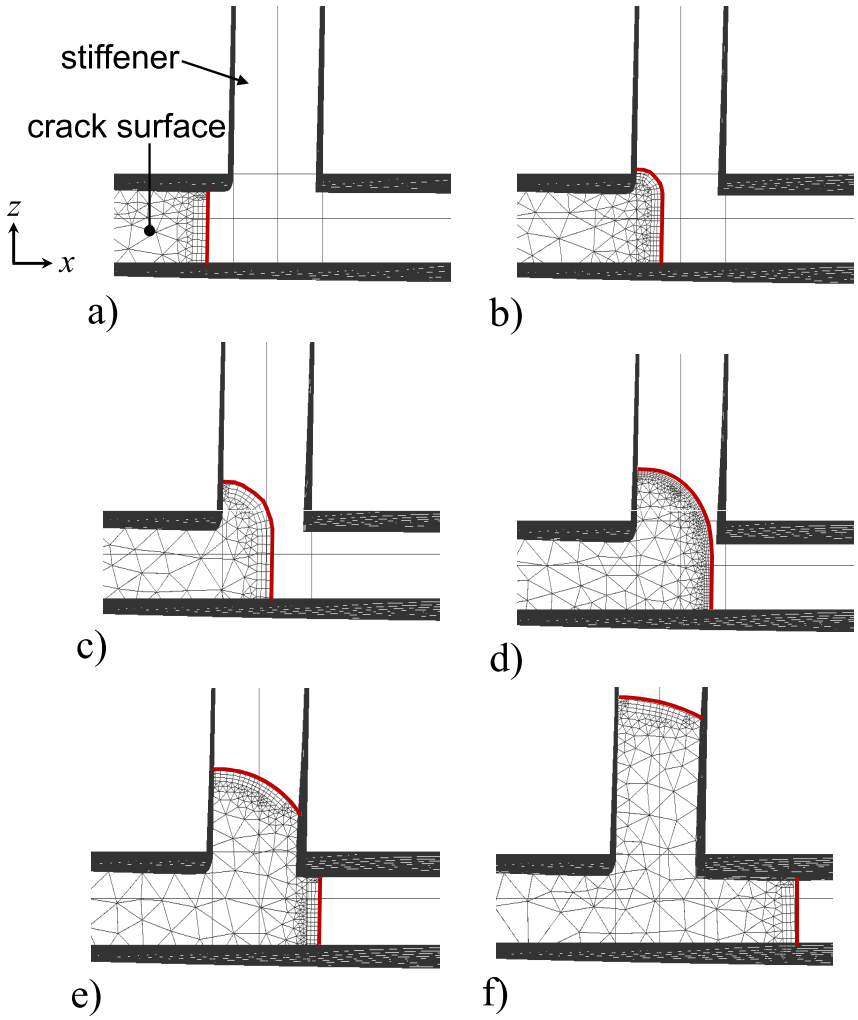

Figure 1.19: Cross-sectional views of ISP mesh model taken at the crack plane and magnified at one stiffener. A thickened line is overlaid along the crack front(s) at each step of crack growth. Views show lead bay crack before entering stiffener(a); transition crack evolution within stiffener (b,c,d); and complete branching into two distinct crack fronts (e,f).

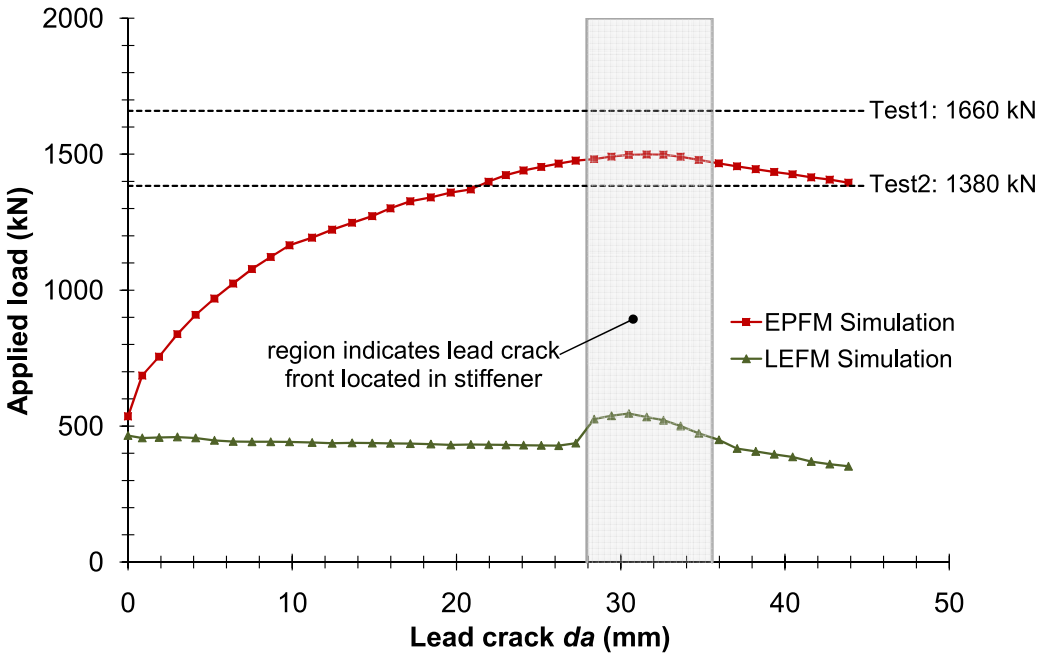

Figure 1.20: Applied load (traction P, Fig. 1.16(b), integrated over applied area) versus half-crack extension, da, from ISP simulation. Maximum applied load is indicated for two corresponding tests conducted at Alcoa Technical Center. Shaded region indicates initially-intact stiffener.

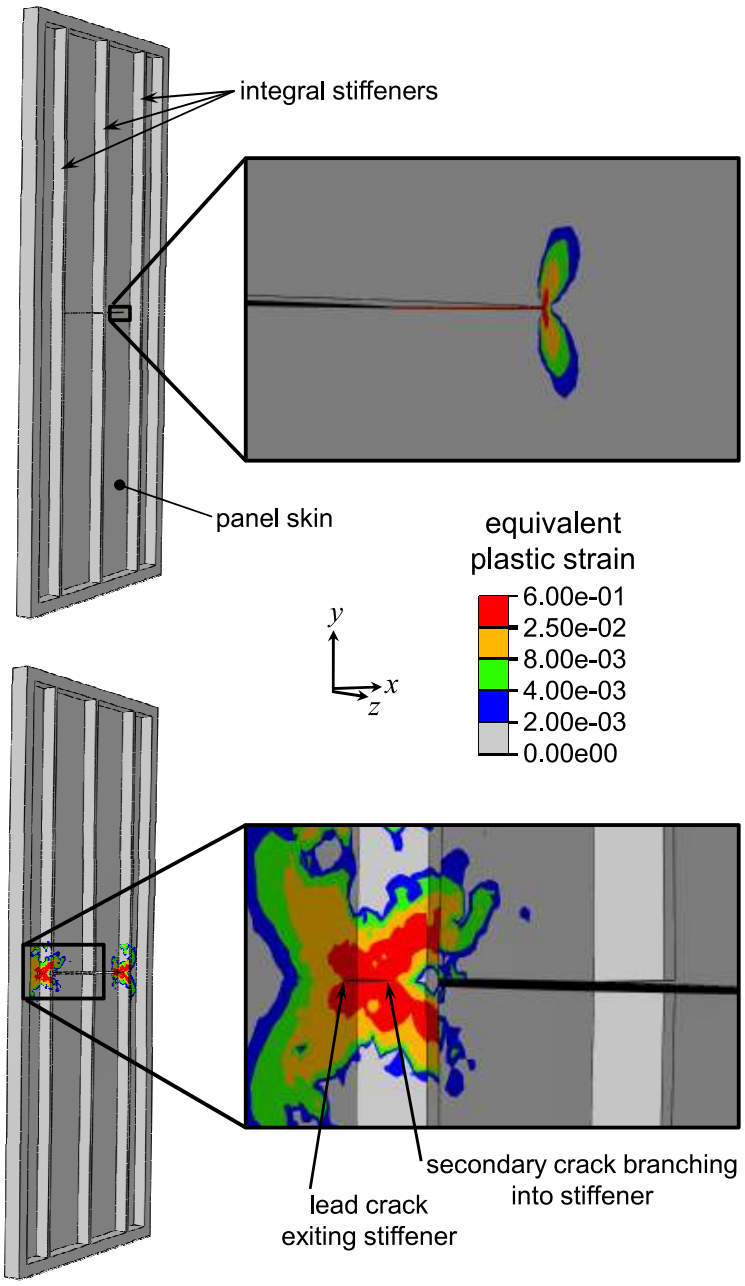

Figure 1.21: Magnified views of simulated crack growth in ISP at half-crack extensions da=0 mm (top) and da=44 mm (bottom). Contours show evolution of equivalent plastic strain fields with crack growth. Deformation is not scaled. FE mesh is not shown for better contour visualization. Complete simulation can be viewed at *www.cfg.cornell.edu*.

CHAPTER 2

EXPERIMENTAL CHARACTERIZATION OF THE EFFECT OF CHEMICAL MILLING ON FATIGUE-CRACK INITIATION IN AN AL-MG-SI ALLOY

2.1 Introduction

Chemical milling is a process that has been in use since the 1950s, whereby structural components (historically, aircraft components) are dimensionally reduced by exposure to specific chemical solutions [71]. Advantages of the chemical milling process compared to conventional machining processes include ability to reduce weight of geometrically complex structures, ability to mill very thin sections without causing warping, ability to maintain tight dimensional tolerances, and considerable savings in cost. For a given chemical solution, the surface finish of a structure after chemical milling depends on a number of factors, including metal-removal rate, surface finish before milling, material grain structure, heat treatment, and alloying chemistry [71].

In general, the effect of surface finish can be imperative depending on the intended application of a structure. For example, many researchers have studied the effect of mechanically induced surface roughness on fatigue life of metals. In the absence of residual stresses, increased surface roughness generally has a deleterious effect on fatigue life among a variety of metals [72, 73, 74, 75]. Even for relatively low roughness (R_a values ranging from 0.5-1.4 μm), a decrease in the fatigue-endurance limit was observed in ground, stress-relieved, steel when compared to polished specimens (R_a values ranging from 0.1-0.3 μm) [76]. This deleterious effect has been attributed to local stress concentrations at

micro-notches, which can give rise to localized plastic strain and subsequent crack initiation [72, 77, 78, 79]. In general, (1) surface roughness tends to affect the initiation portion of fatigue life [80], and (2) the initiation portion of fatigue life constitutes less of the total life in the high-strain, low-cycle fatigue regime compared to that in the low-strain, high-cycle fatigue regime [81]. Thus, it is reasonable to expect that the effect of initial surface roughness on fatigue life is less significant at high-strain ranges than at low-strain ranges. Nonetheless, initiation life can still be considerable for smooth specimens in the low-cycle-fatigue regime. This could explain why some have found a notable reduction in fatigue life of specimens with initally roughened surfaces even in the high-strain, low-cycle-fatigue regime [73, 74, 82].

In addition to mechanical surface treatments, significant efforts have been made to understand the effects of chemical surface treatments on fatigue, typically in the context of corrosion. The effects of various types of corrosion on fatigue behavior is quite complex and depends on a number of material, environmental, and loading factors. For example, Bray et al. [83] showed that for two very similar 2XXX-series aluminum alloys with equivalent fatigue properties in the uncorroded condition, the fatigue lives of the alloys differ considerably after pre-corrosion in $NaCl/H_2O_2$ solution. According to the authors, the difference is due in part to different severities of corrosion-pit configurations, hypothetically resulting from different quantities of large-second-phase particles in the alloys. Reduction in fatigue life for pre-corroded specimens is often attributed to local-stress concentrations at corrosion pits [84, 85, 86]. Recent work by Burns et al. [87] showed that fatigue-crack formation in acidic-exfoliation-corrosion pits in an aluminum alloy is due to a combination of elastic-stress concentra-

tion due to pit macro-topography and local plastic-strain concentration due to pit micro-topography. They also point out that for broadly corroded surfaces, above a threshold applied-stress level, the crack-formation life should tend to zero due to the distribution of local driving forces on the surface. Many studies suggest that the most significant reduction in fatigue life occurs after some initial amount of exposure to corrosive solutions and that the incremental effect of additional exposure thereafter is minimal [88, 89, 90]. This observed plateau in fatigue life with increasing corrosion time might be related to other observations that pit density decreases with increased exposure time due to pit coalescence (e.g. [91]). While the majority of corrosion studies focus on corrosive environments expected for aircraft and marine structures, where the chemical solutions are typically chloride-bearing [83, 88, 89, 90, 91, 92, 93] and where the high-cycle[1] fatigue regime is of particular interest [83, 84, 88, 89, 90, 92, 93, 94], few studies have addressed the potential effects of corrosion in an alkaline solution for structures that experience low-cycle fatigue.

In this study, we consider the application of alkaline-based chemical milling to aluminum-alloy liners of composite-overwrapped pressure vessels (COPVs). COPVs are used extensively to transport and store pressurized fluids in both commercial and space-flight applications [95, 96]. The structures comprise a light-weight composite material (e.g. carbon/epoxy) overwrapping a metallic liner (e.g. aluminum). Sufficiently thin metallic liners are expected to experience a considerable range of plastic strain during autofrettage and subsequent pressurization/depressurization cycles [96]; in such cases, the loading regime for the COPV liners can be regarded as one of low-cycle fatigue. Chemical milling in

[1] As distinguished from low-cycle fatigue, we regard high-cycle fatigue as cyclic fatigue in the absence of macroscopic yielding, where total fatigue life of smooth specimens is typically on the order of 10^5 cycles or greater.

an alkaline solution (NaOH) is currently considered state-of-the-art for reducing thickness of Al-Mg-Si liners used in ultralight propellant tanks [97]. This is due in large part to difficulties associated with machining ultrathin liners by traditional, mechanical methods. Achieving the ultrathin liner dimensions generally requires on the order of hours of exposure to the NaOH solution. Work by Savas and Earthman [98] showed that severe corrosion pitting occurred after only 120 seconds of exposing aluminum 7075-T73 specimens to a caustic, alkaline solution. Thus, the amount of time required to substantially reduce the thickness of a COPV liner is expected to produce widespread pitting and, consequently, increased surface roughness. It is unclear, however, what effect the resulting surface finish will have on the low-cycle-fatigue behavior of the metallic liners.

The objective of this chapter is to report findings on the effect of an alkaline-based chemical milling treatment on the high-strain, low-cycle fatigue behavior of an Al-Mg-Si alloy used in ultrathin COPV liners.

2.2 Experimental Method

The material used in this study is an Al-Mg-Si alloy (Table 2.1) received in the form of a COPV liner, as shown in Fig. 2.1. The liner was manufactured by Samtech International, Inc., Carson, California, according to the following high-level steps: (1) an Al-6061 "O"-condition circular sheet was deep drawn into a cup-like configuration (cylinder with one closed end); (2) the structure was then cold worked by flowforming over a mandrel, causing significant (greater than 50%) thickness reduction and elongation of the cylinder; (3) the open end was spun closed with no internal mandrel to create the port-end dome; (4) the

seamless liner was then heat-treated to achieve a recrystallized, "T6" condition. Mechanical properties of the material were determined according to standardized tensile tests [99] using subscale dogbone specimens machined from the cylindrical portion of the COPV liner (see B.0.4 of the Appendix). The resulting stress-strain curve is provided in Fig. 2.2. The elastic modulus, tensile yield strength (0.2% offset), and ultimate tensile strength of the COPV-liner material oriented in the longitudinal (z) direction are 70.0 GPa, 299.3 MPa, and 346.9 MPa, respectively.

Table 2.1: Chemical composition of AA 6061-T6, wt% [100].

Al	**Mg**	**Si**	**Cr**	**Cu**	**Fe**	**Mn**	**Zn**	**Ti**
Balance	0.8-1.2	0.4-0.8	0.04-0.35	0.15-0.4	≤0.7	≤0.15	≤0.25	≤0.15

Prior to fatigue testing, the material grain sizes were measured midway along the length of the cylindrical portion of the liner. The grain structure is relatively equiaxed as compared to typical rolled-sheet material, and the average grain diameter is approximately 22 μm with a relatively large standard deviation ($\sigma \approx 18$ μm).

2.2.1 Specimens

Fatigue specimens were designed such that: (1) gauge-region thickness is representative of "ultrathin" COPV-liner thickness, (2) the occurrence of corner

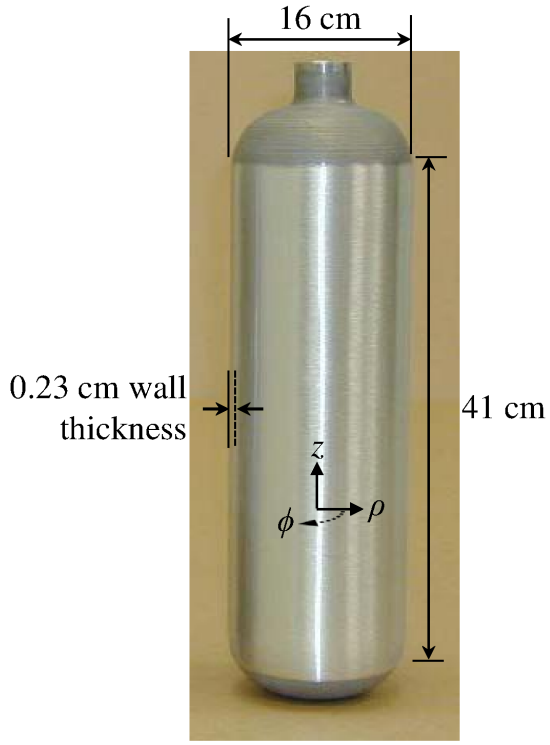

Figure 2.1: As-received COPV liner showing approximate dimensions. Cylindrical coordinate system: z, longitudinal; ρ, radial; ϕ, circumferential.

cracks is minimized, and (3) the region of concentrated stress facilitates observation of naturally initiated cracks. The specimen geometry depicted in Fig. 2.3 is motivated by the designs used in [101, 102] and satisfies these criteria. Specimens were machined from the COPV liner using wire electric discharge machining (EDM). The specimens were aligned lengthwise with the z-direction of the cylinder. The z-ϕ surfaces of each specimen were planed by mechanical milling. Finally, wire EDM was used to create a single, shallow notch, thereby reducing the minimum thickness in the gauge region to 500 μm. It is noted that the wire EDM procedure followed by sufficient chemical milling results in a similar sur-

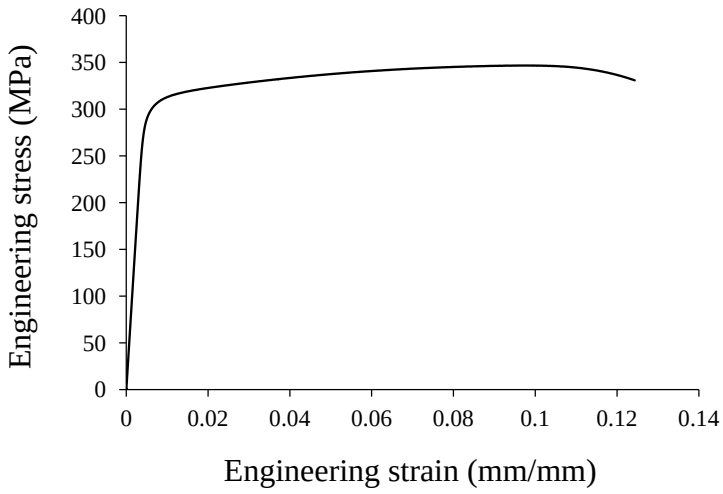

Figure 2.2: Engineering stress-strain curve determined according to standardized tensile tests [99] using subscale dogbone specimens machined from the central region of the AA 6061-T6 COPV liner.

face topography compared to that of as-received COPV-liner material that has been chemically milled under similar conditions; this is likely because the EDM-affected layer is effectively removed during the chemical milling procedure.

Note that under uniaxially applied tension, a small amount of out-of-plane displacement occurs due to the eccentricity induced by the single-shallow-notch geometry. To assess the biaxiality resulting from this specimen design, a three-dimensional finite-element analysis was performed in ABAQUS® using the geometry in Fig. 2.3 and the material behavior shown in Fig. 2.2. Boundary conditions were applied to simulate one-half cycle of loading in the experiment (i.e. one "grip end" was fixed entirely while the other was permitted to move only in the direction of loading, z-direction). The converged mesh comprised $\approx$ 22,000 quadratic elements. Prior to material yielding, a biaxial-stress ratio (i.e.

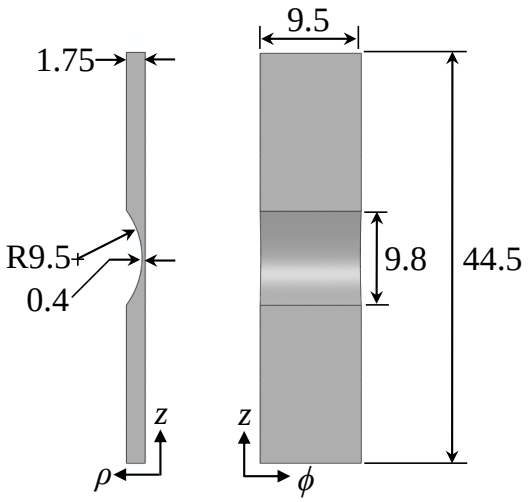

Figure 2.3: Dimensions (mm) of the single-shallow-notch specimens (after surface treatments).

$\sigma_{\phi\phi}$: σ_{zz}) of 0.22:1 was computed in the notch region; $\sigma_{\rho\rho}$ was negligible. It is noted that while some biaxiality is achieved through this design, the stress state does not accurately represent that expected from an ultrathin COPV liner. The validity of such simplified, "uniaxial" specimens for assessing ultrathin, COPV-liner behavior remains the topic of ongoing studies.

After machining, specimens were either electropolished or chemically milled. During each treatment, specimen dimensions were incrementally measured using optical microscopy to ensure that the final, minimum thickness in the gauge region was 400 μm(±10 μm). An electropolishing treatment was considered as the baseline treatment in this study. The treatment involved submerging each specimen in an electrolytic solution of 25% HNO_3 and 75% CH_3OH at a temperature of -30°C for ≈ 5.5 minutes and with 12.5 V applied. The macroscopic appearance of the specimens after electropolishing was bright and shiny compared to the chemically milled specimens (see Fig. B.3 in B.0.2 of the Appendix).

The chemical milling treatment used in this study was similar to that used by the Jet Propulsion Laboratory of the National Aeronautics and Space Administration (NASA) for reducing thickness of aluminum liners to achieve ultralight, COPV, propellant tanks [97]. Each specimen was submerged in a caustic, alkaline solution of 1 g NaOH per 100 mL of water (etchant 2 listed in Table 3 of reference [103]) at a temperature of 55°C for a total submersion time of ≈ 30 minutes. Specimens were desmutted in an aqueous deoxidizing solution of 5% HF and 45% HNO_3. The macroscopic appearance of the chemically milled specimens was dull and light grey in color compared to the electropolished specimens.

2.2.2 Surface Topography Measurements

Prior to fatigue testing, surface topography of each specimen was quantitatively assessed using a topographical scanning electron microscopy (SEM) technique [104, 105, 106]. The technique is based on stereology and, in this case, utilizes backscattered-electron detection signals from a four-way divided detector to map the 3-D surface topography of an object. The SEM micrographs for the topography measurements were taken using a Hitachi S-3700N SEM. For all specimens, the SEM micrographs were collected in the center of the notch region at a working distance of 10.0 mm, an accelerating voltage of 20.0 keV, and a magnification of 500x, resulting in a 200 x 250 μm^2 scanned region for each specimen. Surface measurements were calibrated using a slanted aluminum calibration sample with a surface of known slope that was imaged using the aforementioned parameters.

2.2.3 Fatigue Testing and Fractography

A preliminary set of monotonic-load tests was conducted using digital-image correlation to determine the peak-applied load levels required to achieve particular strain levels in the gauge region of the specimens (see also section B in the Appendix). Figure 2.4 shows an example of field data measured at a particular applied-load level. From the digital-image correlation tests, applied-load levels that resulted in maximum-principal notch strains, ϵ_{zz}, of 1.0%, 1.6%, and 2.0% were selected for the peak-applied load levels in the fatigue tests. These strain levels were selected because they represent potential hoop strains in thin COPV liners during autofrettage and/or maximum expected operation pressures. The corresponding applied-load levels normalized by the load at which notch yielding occurred[2], P_{max}/P_{yield}, were determined to be 1.25, 1.47, and 1.64, respectively. In other words, the peak-applied loads selected for fatigue testing were 25%, 47%, or 64% above the load that caused yielding in the notch region.

All specimens were tested in air in load control at constant amplitude (R=0.1) until failure using a servohydraulic load frame. Additional details are provided in B.0.3 of the Appendix. Thirteen specimens were tested in total, two at each combination of applied-load level and surface treatment. An additional chemically milled specimen was tested at the highest applied-load level based on the percent difference of fatigue life observed between the first two chemically milled specimens at that load level.

Following fatigue failure, four specimens were selected (one for each type of

[2] P_{yield} is defined as the load at which averaged ϵ_{zz} (based on digital-image correlation data) in a 1x1 mm^2 region centered in the shallow notch is equal to the 0.2% offset yield strain that was determined from standardized tensile tests [99] of the cylinder material.

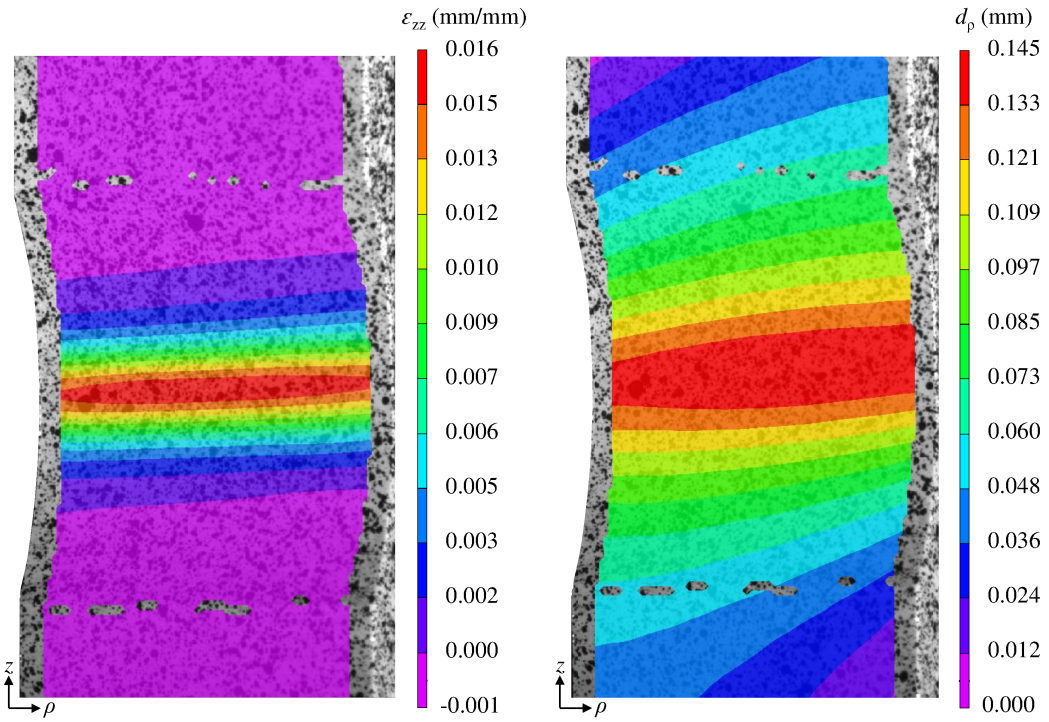

Figure 2.4: Maximum-principal strain data, ϵ_{zz}, (left) and out-of-plane displacement data, d_ρ, (right) measured using digital-image correlation. Results are shown with P_{max}/P_{yield}=1.47 uniaxial tension applied.

surface treatment from the highest and lowest peak-applied loads) for detailed fractographic analysis using a Zeiss EVO 60 SEM. High-magnification micrographs were taken along the entire area of the failure surface of each specimen. Crack initiation sites were identified by the appearance of river-like patterns and, in some cases, fatigue striations approximately perpendicular to the direction of crack growth.

2.3 Results

2.3.1 Surface Topography

The electropolishing and chemical-milling treatments resulted in notably different surface topographies. Note from Fig. 2.5(b) that the pits formed by exposure to the caustic NaOH solution are widespread and somewhat hemi-spherical with relatively smooth edges as compared to typical corrosion pits caused by exposure to lower-pH, chloride-bearing solutions (e.g. see [90, 91, 98]). Depending on the difference in potential between constituent particles and the matrix in aluminum alloys, exposure to neutral or slightly acidic chloride-bearing environments tends to cause localized pitting at the constituent particles or their peripheries [107]; whereas, exposure to alkaline environments tends to cause generalized corrosion over the entire surface due to a breakdown of the unstable passive film on the specimen surface during exposure [108, 109]. For a given exposure time, alkaline solutions tend to be much more aggressive than lower-pH solutions [98, 108, 109], leading to the widespread attack and consequential surface roughness evident in Fig. 2.5(b). On the other hand, the electropolished surface shown in Fig. 2.5(a) has a much smoother topography due to anodic leveling [110].

There are several ways to quantify the difference in surface texture or topography [111, 112]. An example is the parameter S_{dr} (defined in [113]), which is the ratio of "developed" surface area (i.e. three-dimensional surface area, S_3, less the two-dimensional scanned area, S_2) to the two-dimensional scanned area,

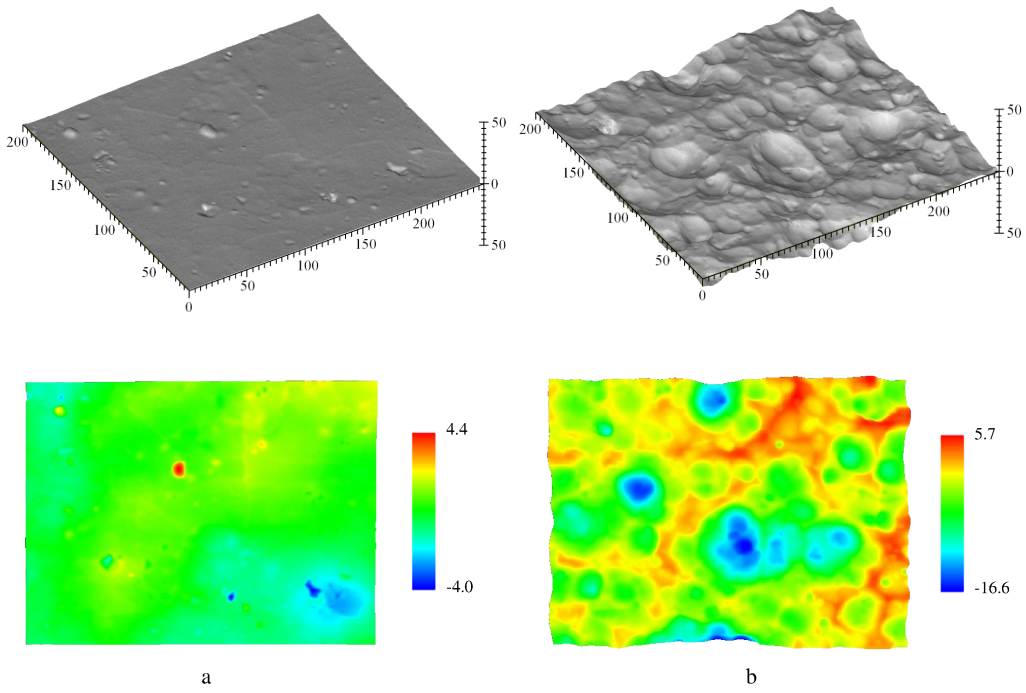

Figure 2.5: Surface topographies and corresponding contour maps of surface height: (a) electropolished surface; (b) chemically milled surface. Dimensions in μm.

S_2:

$$S_{dr} = (S_3 - S_2)/S_2. \tag{2.1}$$

Average values of S_{dr} along with average surface roughness values, R_a, for the two surface treatments are provided in Table 2.2.

Table 2.2: Average topographical surface parameters.

Surface Treatment	R_a	S_{dr}
Electropolished	0.78 μm	0.008
Chemically Milled	2.37 μm	0.094

In addition to homogenized measures of surface topography, individual pit morphologies were examined in detail using the SEM-based topography maps. Four samples (two from each surface treatment) were selected for the detailed characterization. Characterizing corrosion pits in the chemically milled samples was non-trivial in the cases where multiple pits coalesced or where smaller, sub-pits formed within larger pits. To facilitate systematic characterization of pits, pit depth was defined as the difference between the minimum point within a pit and the average of two local-maximum points extracted from a two-dimensional profile intersecting the minimum point of the pit. Measurements of individual-pit parameters (depth and diameter) were made, and the measurements were used to generate projected distributions of pit depth and aspect ratio expected in a 1x1 mm^2 region of material after either surface treatment, shown in Fig. 2.6. For a given surface area, chemical milling compared to electropolishing results in a 738% increase in the number of pits and an increase in average pit depth from 1.87 μm to 4.23 μm with a significantly larger standard deviation; however, the values of pit aspect ratios are similar among chemically milled and electropolished specimens.

2.3.2 Fatigue Life

Results from the fatigue tests are presented in Fig. 2.7. At each of the three applied-load levels, the average fatigue life of the chemically milled specimens was reduced by approximately 50% compared to that of the electropolished specimens. Results from Student's t-tests at each applied-load level indicate that the difference in mean fatigue life between chemically milled and elec-

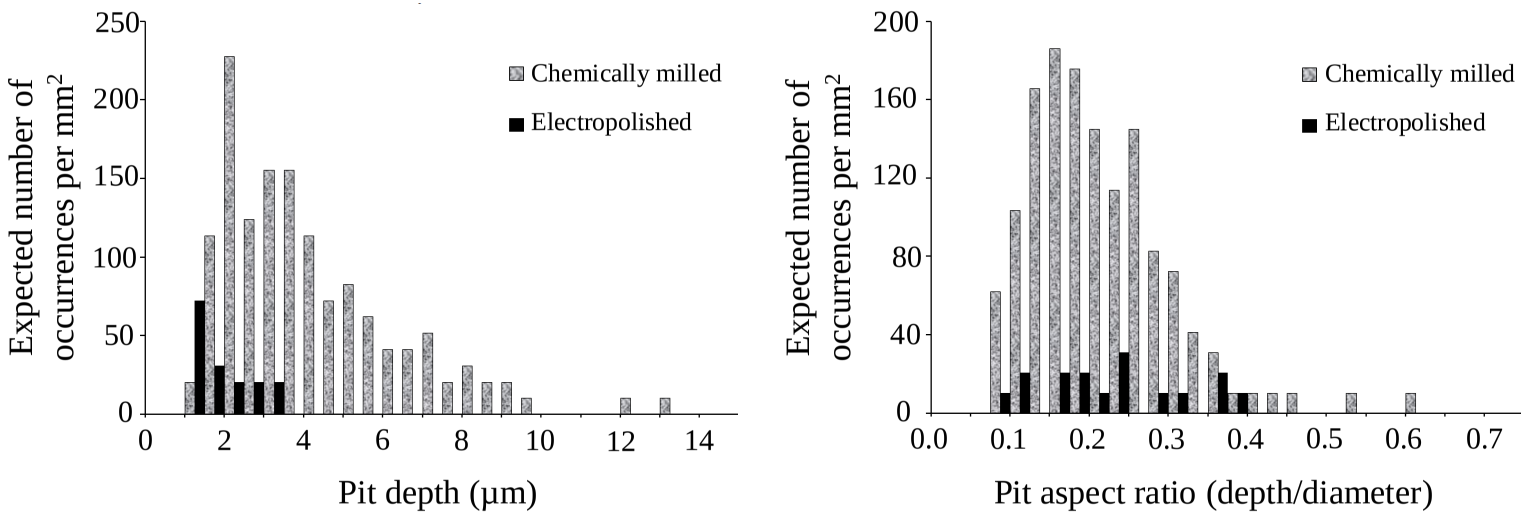

Figure 2.6: Distributions of pit characteristics for the electropolished and chemically milled specimens.

tropolished specimens is statistically significant for a confidence interval of 95%. Moreover, a two-way analysis of variance performed using the R programming language [114] for the entire data set shown in Fig. 2.7 indicates that there is a statistically significant effect ($p < 0.001$) of surface treatment on fatigue life.

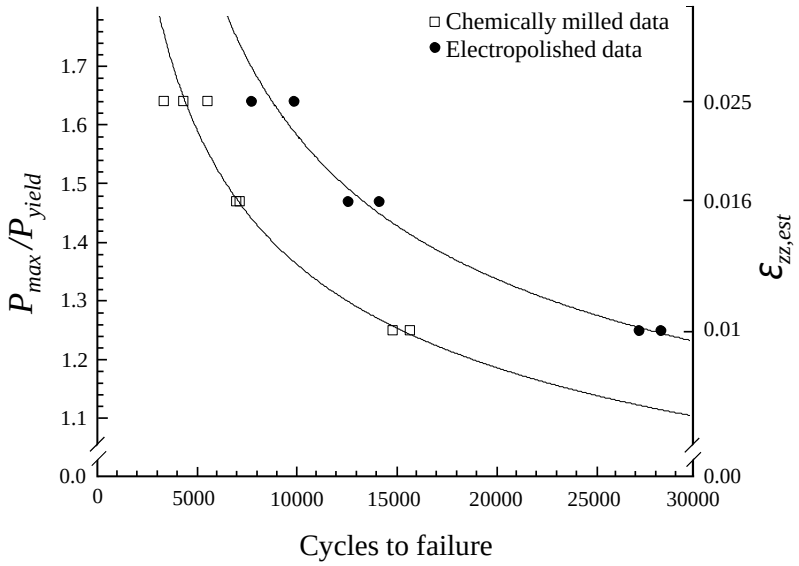

Figure 2.7: Normalized peak-applied load, P_{max}/P_{yield}, versus fatigue life for tests performed at R=0.1. The right vertical axis shows the estimated maximum-principal-notch strain, $\epsilon_{zz,est}$, corresponding to each peak-applied-load level as determined from the digital-image correlation tests. Note that no error bars are plotted, as P_{yield} varied by less than 1% among the preliminary digital-image correlation tests.

2.3.3 Fractography

Crack-initiation sites were characterized for four samples, one for each type of surface treatment at the highest and lowest peak-applied load levels. For the 15.2 mm^2 of total fracture-surface area that was imaged at high magnification, a total of 273 crack-initiation sites were observed and cataloged. Somewhat surprisingly, as shown in Table 2.3, there does not appear to be an obvious trend in the number of observed crack-initiation sites with surface treatment or applied-load level. As discussed in section 2.4, this observation could indicate that, for the high-strain ranges considered, reduction in fatigue life is not necessarily attributed to an increased number of crack-initiation sites, but could instead be attributed to shorter initiation lives for individual crack-inita tion sites.

Table 2.3: Number of observed crack-initiation sites per mm^2 (total number).

Surface Treatment	P_{max}/P_{yield}**=1.25**	P_{max}/P_{yield}**=1.64**
Electropolished	17 (66)	21 (78)
Chemically Milled	18 (69)	16 (60)

Three distinct crack-initiating features are evident upon observation of the 273 initiations sites: (1) pit, (2) flat facet, and (3) subsurface feature (typically a void, occasionally containing remnants of possible constituent particles). Micrographs exhibiting the various characteristics of the observed crack-initiation sites are presented in Fig. 2.8. A histogram of the observed initiation features is shown in Fig. 2.9. Note that the majority of crack-initiation sites exhibit one

or both of the first two features listed above (i.e. pit and/or flat facet). For all crack-initiation sites with associated pits, the apparent depth and diameter of the primary initiating pit was measured. Histograms showing the distribution of crack-initiating-pit aspect ratios and depths are shown in Figs. 2.10 and 2.11, respectively, where the data are segmented into pit-only crack initiation and pit-and-facet crack initiation.

To elucidate the cause of the flat facets that are apparent at many crack-initiation sites, a technique was used that combines SEM-based stereology and electron-backscatter diffraction (EBSD) [115, 116, 117], whereby facet normals are determined first in the sample reference coordinates and are subsequently transformed into the crystal coordinates using the rotation matrix, $\mathbf{g}$. The method involves capturing SEM images of each facet at two different global tilt angles and determining the spatial coordinates of three fiducial points on the facet surface [118]. Two vectors are then formed using the spatial coordinates of the three points, and the cross product of the two vectors yields the facet normal, $\hat{n}$, in the sample reference frame. Euler angles are determined from EBSD data collected on a polished surface immediately adjacent to the facet. Finally, the facet normal in the crystal coordinate system, $\hat{n}'$, is determined by the transformation:

$$\hat{n}' = \mathbf{g}(\phi_1, \Phi, \phi_2) \cdot \hat{n}, \tag{2.2}$$

where ϕ_1, Φ, ϕ_2 are the Euler angles of the grain containing the facet. Ro et al. [119] found the uncertainty of facet crystallography using this methodology to range from less than 3° to $\approx 5^\circ$ depending on several factors.

The current implementation of this method was validated by using models of "grains" with inclined facets of known normal vectors (in both the reference and

crystal coordinate systems). Once the implementation was validated, thirteen facets near crack-initiation sites were analyzed on an electropolished specimen. Figure 2.12 shows an example of one facet that was analyzed using the technique described above. All of the facet normals that were analyzed on the electropolished specimen were oriented between 38° and 54° from the loading axis, with an average orientation of 46°. Additionally, all of the facet normals were within 5° of ⟨111⟩ poles. Nine additional facets were analyzed on a chemically milled specimen; although EBSD data could not be collected on the adjacent surface due to poor surface quality, the facet normals were nonetheless determined in the sample reference frame using only SEM stereology. For all nine facets that were analyzed on the chemically milled specimen, the orientation of normals with respect to the loading axis ranged from 39° to 55°, with an average orientation of 48°.

2.4 Discussion

The observed 50% decrease in fatigue lives among the chemically milled specimens can likely be attributed to local, pit-induced, stress concentrations that cause early initiation of fatigue cracks. This explanation is supported by others who have found that reduced fatigue lives among specimens with mechanically-induced surface roughness [73, 74, 80] or with surfaces pre-corroded in chloride-bearing solutions [83, 90, 93] are caused by reduction in the initiation portion of life. As suggested by Shahzad et al. [86] and Sankaran et al. [84] the observed early initiation in acidic-pre-corroded specimens is due to the increased local stress concentration at corrosion pits. This explanation is

also supported by finite-element analyses, where stresses were computed using the measured surface topography of pre-corroded aluminum 5059 [85]. The finite-element results showed local stress concentrations within the pits of the pre-corroded surface, which, in some cases, could be sufficient to cause micro-cracking. Burns et al. [87] also found from finite-element analyses that driving forces caused by the macro- and micro-topography of exfoliation-corrosion pits promoted crack formation in aluminum 7075-T651 pre-corroded in acidic solution.

The argument for early crack initiation in chemically milled specimens is also supported by the observed number of crack-initiation sites (see Table 2.3). Based on detailed observations of the failure surfaces, it appears that chemical milling does not result in significantly more crack-initiation sites than electropolishing for the Al-Mg-Si alloy cycled at comparable load levels above macroscopic yield. This implies that given the same number of crack-initiation "opportunities", and given that surface condition does not significantly affect subsurface propagation [73, 74, 80, 83, 90, 93], then the reduced fatigue lives among chemically milled specimens must be attributed to reduced crack-initiation life. For example, there is a similar distribution of locations available for preferred-crystallographic crack initiation in both the chemically milled and electropolished specimens, because the chemical milling does not change the distribution of grain orientations for a sample; however, the existence of a stress concentration due to a corrosion pit in the neighborhood of a preferred crystallographic orientation drives the initiation event to occur earlier in the fatigue life of the chemically milled specimen. The observed 50% fatigue-life reduction suggests that, even in the high-strain, low-cycle-fatigue regime considered in this work,

crack initiation accounts for a considerable portion of total life in the smooth, electropolished specimens.

Among the observed crack-initiation features (see Figs. 2.8 and 2.9), the majority of crack-initiation sites in the chemically milled specimens exhibit either a pit or a combination of a pit and a flat facet; whereas, the majority of crack-initiation sites in the electropolished specimens exhibit flat-faceted features only. Results from SEM-based stereology coupled with EBSD data for faceted crack-initiation sites on an electropolished specimen indicate that the flat facets correspond to {111}-slip planes, or stage-I cracking [120]. Similar flat facets, oriented between 39° and 55° from the loading axis, are evident on chemically milled specimens. Recent work by Takahashi et al. [121] shows very similar {111}-related flat facets occurring at initiation sites in polished specimens of the same aluminum alloy (6061-T6) but in the high-cycle-fatigue regime. Similar to the current work, the flat facets observed in [121] occur nearly exclusively at the specimen surface because, as the authors suggest, the resistance to crystallographic slip is higher in the bulk of the material due to increased constraint from surrounding grains. Lamark et al. [75] also found that for polished aluminum 6061-T6 specimens under variable-amplitude loading (in both the high- and low-cycle fatigue regimes), the dominant crack-initiation mechanism was slip-plane cracking, manifested by smooth facets inclined at 45° to the tensile loading axis.

The histograms in Figs. 2.10 and 2.11 represent the observations of all pit-related, crack-initiation sites among the chemically milled and electropolished specimens included in the fractographic study. The correlation between pit

depth and crack initiation is more evident than that between pit aspect ratio and crack initiation. As illustrated in Fig. 2.11, for pit depths less than 8 μm, the majority of crack-initiation sites involve the additional mechanism associated with flat facets (i.e. crystallographic slip). However, for pit depths greater than 8 μm, pits are, more frequently, sufficient to initiate cracks independently of the crystallographic-slip mechanism associated with flat facets. The distributions in Fig. 2.11 clearly show that as the pit depth increases, the mechanism of crack initiation changes from predominantly crystallographic slip to predominantly pit-induced-stress concentration, though the two often act in combination.

Lamark et al. [75] observed similar "competing" crack-initiation mechanisms in specimens of the same alloy (aluminum 6061-T6) with smooth and mechanically roughened surfaces. They found that the smooth specimens exhibited stage-I slip-plane crack initiation; whereas, the specimens with rough surfaces exhibited stage-II initiation influenced by tiny grooves on the surface caused by grinding. Presumably, the tiny grooves act as stress concentrations. In the study, there were a few instances where smooth facets similar to those observed on the failure surfaces of the smooth specimens were also observed on the failure surfaces of the rough specimens. Additionally, they found that under low-cycle fatigue conditions, the average fatigue life of the rough specimens was reduced from 9629 to 5172 cycles, which is very similar to the percent reduction in fatigue life due to chemical milling observed in this study. Given the similarities in observed crack-initiation mechanisms and reduction in fatigue lives between the current study and the study by Lamark et al. [75] it is reasonable to suggest that the effect of mechanically induced surface roughness is similar to the effect of chemical milling on fatigue behavior of the Al-Mg-Si alloy.

Based on the above discussion, the findings herein strongly suggest that a greater number of cycles is required to initiate a crack in the *absence* of a stress concentration induced by a pit, in which case initiation occurs solely by {111} slip-plane cracking. In the presence of a sufficiently large pit, the resulting local stress concentration can cause early initiation either independently of or in conjunction with crystallographic slip. This finding is consistent with two-parameter life models. For example, Hochhalter et al. [122] recently showed through detailed, microstructural, finite-element analyses that fatigue-crack nucleation from second-phase particles in aluminum-alloy 7075-T651 depended on both maximum-tangential stress and slip-based damage accumulation near second-phase particles; they found that as the local maximum-tangential stress increased, both the crack-nucleation life and the amount of critical, slip-based-damage accumulation decreased. This is analagous to findings in this work, where the driving stress herein appears to be derived from corrosion pits. A schematic of this idea, adopted from [122], is shown in Fig. 2.13. Although the findings from this work support this hypothesis, further investigation is required to quantify the relationship among critical slip-based damage, local-stress concentration, and crack-initiation life.

While the results presented in Fig. 2.7 are not intended to serve as a fatigue-life prediction tool for full-scale, ultrathin, COPV liners, the finding that chemical milling causes a notable reduction in low-cycle fatigue life due to early onset of crack initiation can be an important consideration in the design of COPV liners. This is particularly true in the case of commercially used COPVs, which tend to have service lives on the order of those shown in Fig. 2.7. COPVs used by

NASA for space-flight applications, on the other hand, typically have limited service lives on the order of hundreds of cycles or fewer [123].

2.5 Conclusions

A study was conducted to determine the effects of a chemical milling process on the low-cycle-fatigue behavior of an Al-Mg-Si alloy used for ultrathin, metallic liners in composite-overwrapped pressure vessels (COPVs). Comparisons of fatigue life and crack-initiation mechanisms were made among specimens that were either electropolished or chemically milled in an alkaline solution (NaOH). From the study, the following conclusions are made:

- At each of three applied-load levels above macroscopic yield, average fatigue life of chemically milled specimens is approximately half that of electropolished specimens.
- The fatigue-life reduction of the chemically milled specimens is not attributed to an increased number of sites for crack initiation; rather, the reduction is more likely due to early onset of crack initiation for a similar number of crack-initiation sites compared to electropolished specimens.
- The majority of crack-initiation sites for the electropolished specimens are associated with flat facets that are quantitatively determined to be {111}-slip planes; the majority of crack-initiation sites for the chemically milled specimens are associated with either a pit or a combination of a pit and a flat facet similar to those observed in the electropolished specimens.
- Among all pit-associated crack-initiation sites observed in both electropolished and chemically milled specimens, flat facets indicative of crystallo-

graphic slip typically accompany pits if pit depths are less than a certain threshold (8 μm in this study); whereas, pits with depths greater than the threshold are, more frequently, sufficient to initiate cracks independently of the slip-based mechanism associated with the flat facets. This could indicate a transition in the crack initiation mechanism (crystallographic slip, pit-induced-stress concentration, or some combination thereof) depending on the severity of local stresses induced by pitting.

- By following chemical milling (or replacing it altogether) with a treatment that reduces surface roughness (e.g. electropolishing), and thereby decreases pit depths on the surface, improved fatigue lives are expected for Al-Mg-Si structures, including ultrathin COPV liners.

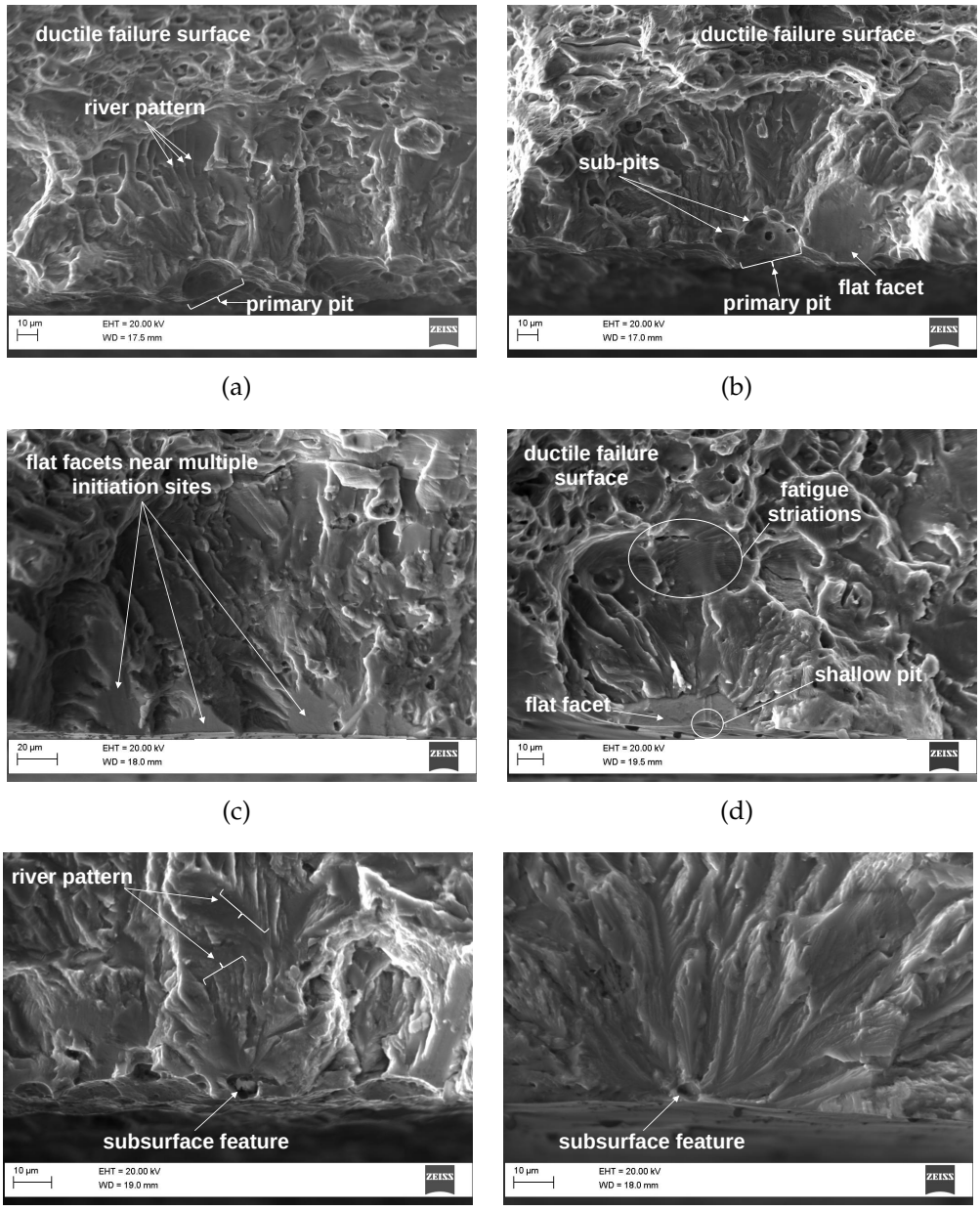

Figure 2.8: Scanning-electron micrographs depicting the range of crack-initiation characteristics (pits, facets, and subsurface features) in chemically milled specimens (a,b,e) and electropolished specimens (c,d,f) observed in the current study.

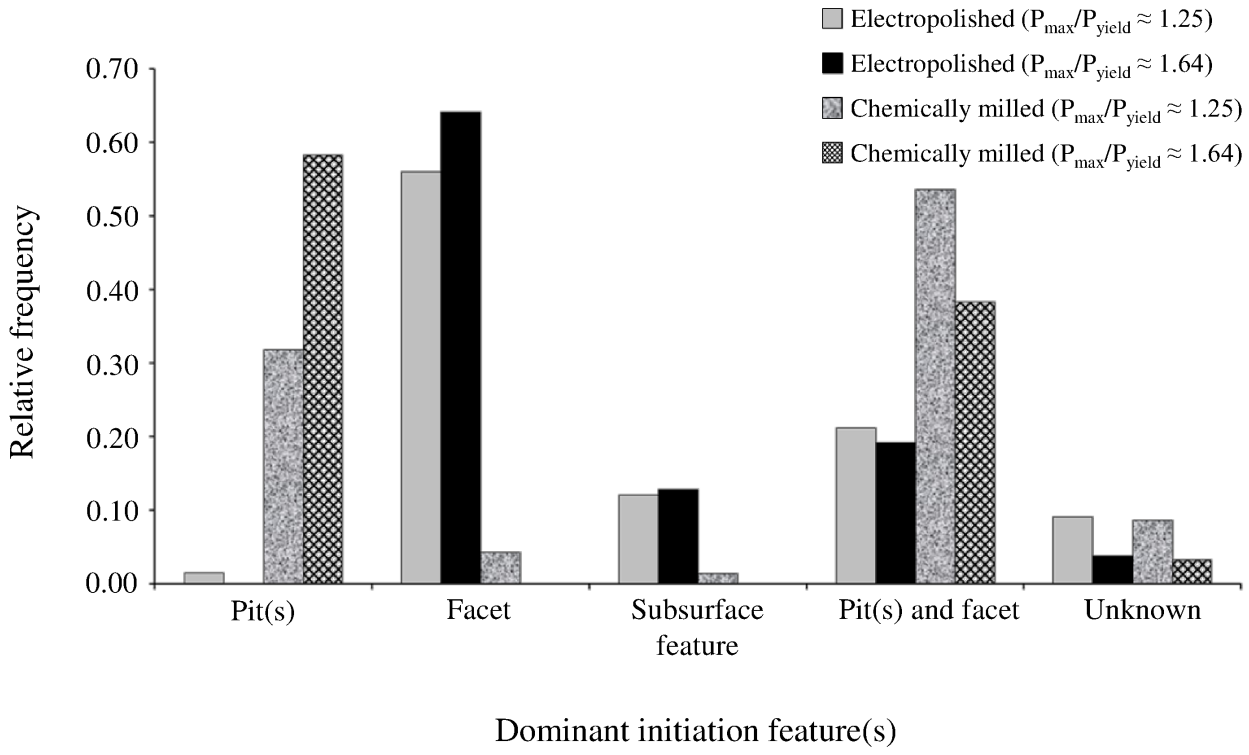

Figure 2.9: Histogram of observed initiation characteristics for four specimens with different combinations of surface treatment and peak-applied load. Relative frequency is the number of observed initiation sites having a particular characteristic divided by the total number of observed initiation sites for each specimen.

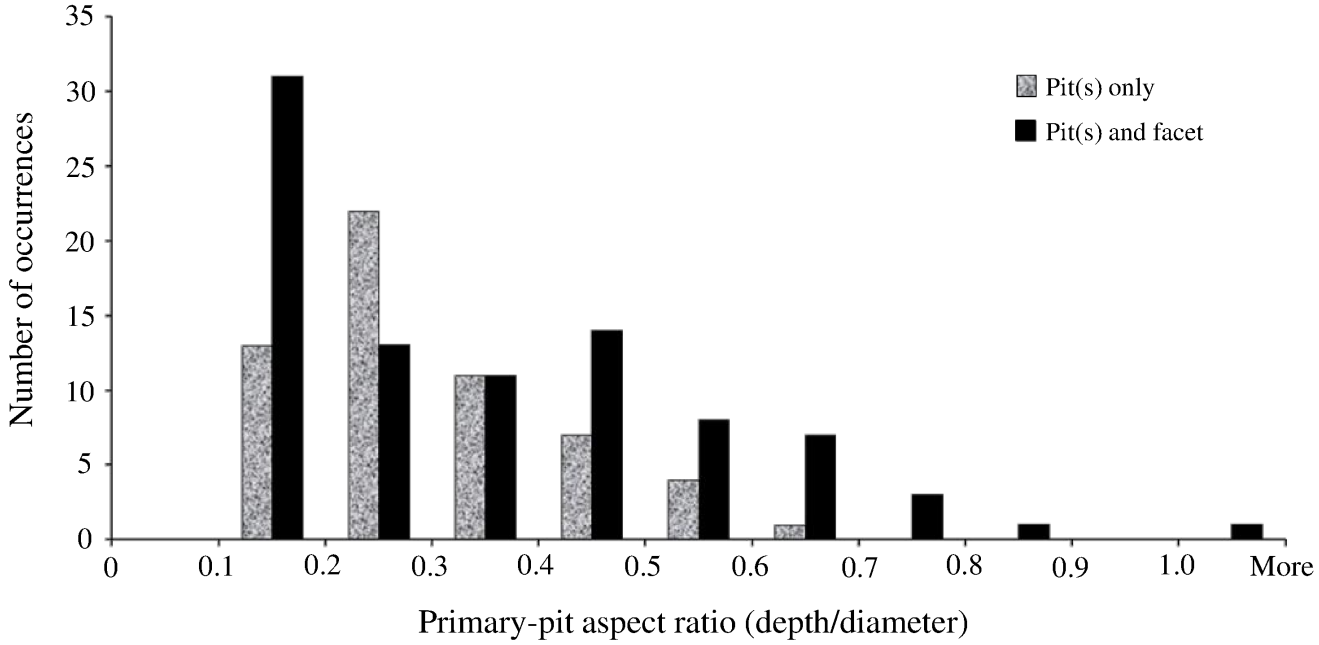

Figure 2.10: Histogram showing aspect ratios of crack-initiating pits for all pit-related initiation sites observed among four specimens. Data are segmented into two types of pit-related initiation. If subpits are present at an observed initiation site, only the primary pit is measured.

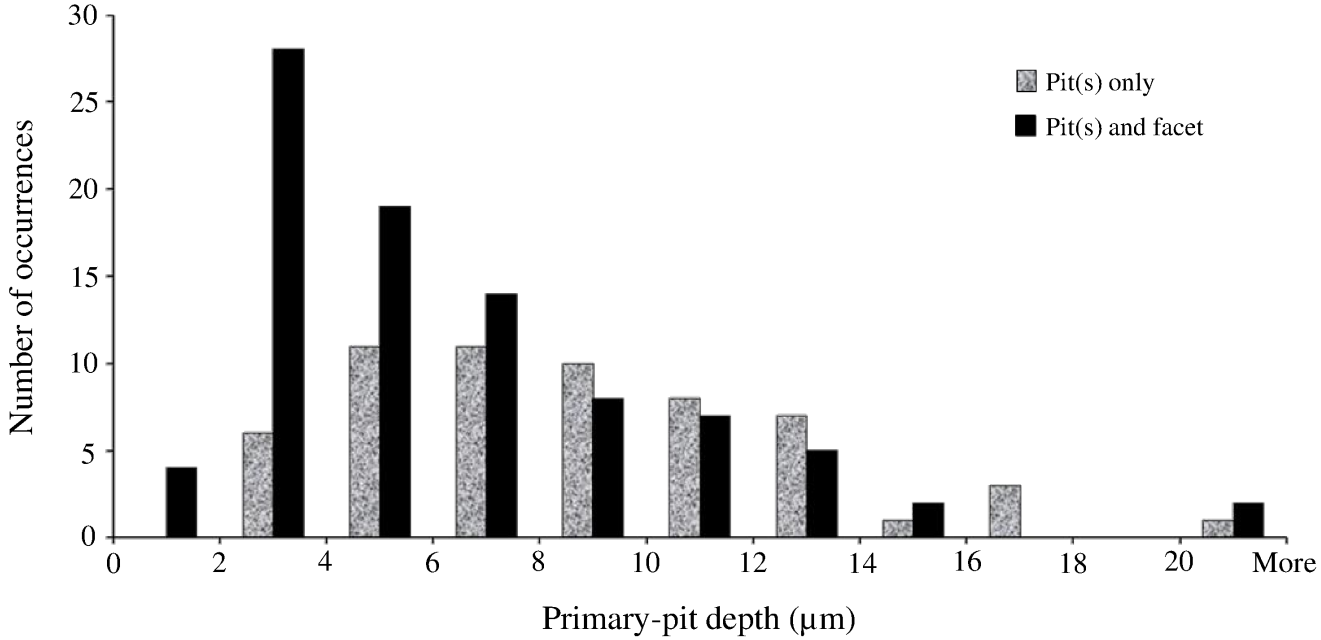

Figure 2.11: Histogram showing depths of crack-initiating pits for all pit-related initiation sites observed among four specimens. Data are segmented into two types of pit-related initiation. If sub-pits are present at an observed initiation site, only the primary pit is measured.

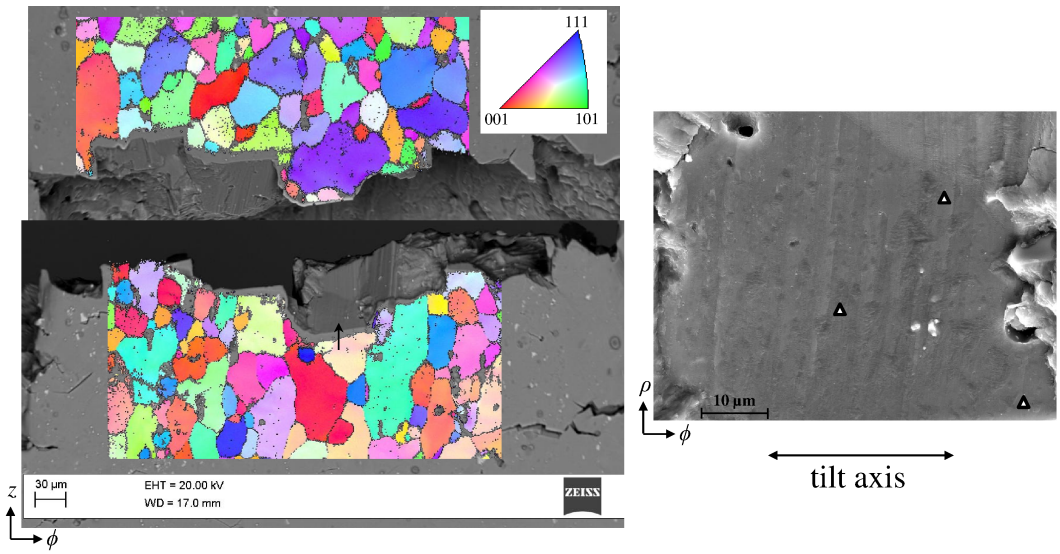

a b

Figure 2.12: (a) Inverse-pole-figure maps adjacent to crack-initiation sites exhibiting flat facets; maps show raw data and are plotted with respect to the [100] direction, which is parallel to the loading (z) direction. The facet indicated by the black arrow is shown in the micrograph in (b). (b) Micrograph used in the SEM-based stereology technique to determine the facet normal. The technique involves imaging the facet at two distinct tilt angles about the tilt axis shown. Triangles indicate small features on the facet surface used for calculating the facet normal. The facet shown was found to have a normal oriented 50.7° from the loading axis and 3° from the $[\bar{1}\bar{1}1]$ direction.

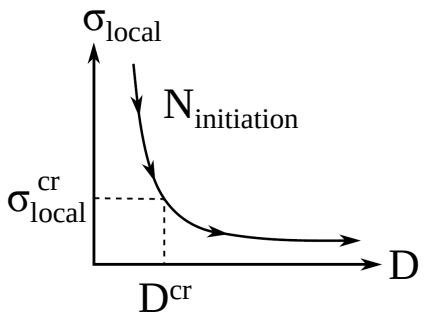

Figure 2.13: Modified schematic adopted from [122]. The current work suggests that as pit-induced driving stress, σ_{local}, increases, the critical slip-based damage, D, and crack-initiation life, $N_{initiation}$, decrease.

CHAPTER 3

THREE-DIMENSIONAL EXPERIMENTAL CHARACTERIZATION OF MICROSTRUCTURALLY SMALL FATIGUE-CRACK EVOLUTION IN AN AL-MG-SI ALLOY

3.1 Introduction

Over the past several decades, researchers have placed considerable emphasis on understanding mechanisms governing the evolution of microstructurally small fatigue cracks (MSFCs), i.e. cracks with dimensions on the order of microstructural features of the material (e.g. grains) [124, 125]. To that end, many techniques have been developed to observe and characterize the evolution of MSFCs in polycrystalline materials. The reader is referred to a review article by Chan [126] and a book by Krupp [127] describing efforts to characterize MSFC initiation and propagation.

The majority of MSFC-characterization techniques involve 2D measurements (i.e. observations made on the free surfaces of fatigue specimens), which have been well documented throughout the literature [128, 129, 130]. With advances in automated acquisition of high-resolution electron-backscattered diffraction (EBSD) data, many studies over the past decade have coupled imaging techniques with EBSD to study MSFC evolution relative to crystallographic orientation [129, 131, 132]. However, complex crack-surface morphology, underlying 3-D crystallography, and variability in local propagation rates cannot be described sufficiently using just free-surface measurements, which provide only trace-related information (e.g. lines created from the intersection of a 3-D crack

surface with the viewing surface). In order to understand and eventually predict the evolution of MSFCs, e.g. using high-fidelity numerical models [133], there is a need for quantitative characterization methods that extend beyond free-surface observations. Some such methods are described in the following two subsections.

3.1.1 Fractography-based MSFC Characterization Techniques

Many researchers have used fractography techniques to gain information from exposed fatigue-crack surfaces, resulting in pseudo 3-D characterization methods. For example, rather than relying on 2D-trace analyses to determine *possible* crystallographic planes on which MSFCs evolve, some have used fractography with diffraction-based methods to determine quantitatively the precise crystallography of individual facets on fatigue-crack surfaces [5, 115, 116, 117, 119, 134, 135, 136].

Methods for measuring facet crystallography on fatigue-crack surfaces can be categorized as direct or indirect. Direct methods involve collecting diffraction data directly from the facet on the fatigue-crack surface, e.g. by electron beam [134] or X-ray [137]. This requires careful alignment of the facet relative to the incident beam, and the specimen must be re-aligned for each unique facet to be characterized. The measurement difficulty increases with increasing fracture-surface roughness and damage (i.e. plastic deformation). Indirect methods, on the other hand, rely on grain-orientation information collected on a prepared surface adjacent to the faceted fatigue-crack surface [5, 115, 116, 117, 119, 135, 136]. For the indirect methods, quantitative facet crys-

tallography involves first determining the facet normal, $\hat{n}$, in the spatial reference frame using SEM-based stereology [118]. Subsequently, $\hat{n}$ can be resolved into the crystal normal, $\hat{n}'$, by the transformation:

$$\hat{n}' = \mathbf{g}(\phi_1, \Phi, \phi_2) \cdot \hat{n}, \tag{3.1}$$

where $\mathbf{g}$ is the orientation matrix and ϕ_1, Φ, ϕ_2 are the Euler angles of the grain containing the facet. Use of indirect methods is generally limited to facets that are adjacent to the specimen free surface, where grain-orientation data can be collected. Obtaining facet crystallography for interior grains requires serial sectioning, which is inherently destructive. While quantitative facet crystallography provides important information regarding the crystallographic nature of MSFC evolution, it does not, in practice, provide crystallographic information at high resolutions over an entire fatigue-crack surface. Nor does it provide information pertaining to the *rate* of MSFC propagation.

Subsurface crack-growth rates can be measured in a retroactive manner using a technique known as *marker banding* [87, 90, 138, 139, 140, 141], whereby a loading spectrum is designed to imprint unique patterns on the fatigue-crack surface that demarcate the crack-front shape at programmed cycle intervals. Following failure, crack-front profiles (marker bands) are identified using fractography. This information can then be used to quantify rates of crack propagation below the free surface. Although marker banding has typically been used for self-similar, long-crack growth, recent studies [140, 90, 87, 141] have used marker banding to characterize crack propagation near crack-initiation sites (within 20 μm) in an aluminum alloy. Traditional marker-band analyses [87, 90, 138, 139, 140, 141] do not account for the true 3-D nature of crack propagation since 2D projections of the marker bands are used to calculate crack-

growth rates.

Though quantitative facet crystallography and marker-band analyses provide much more information than the free-surface observations described earlier, these methods do not, in their usual implementation, describe completely the 3-D evolution of MSFCs within their local microstructural environments.

3.1.2 3-D MSFC Characterization Techniques

Over the past decade, advances in synchrotron radiation techniques have enabled non-destructive, high-resolution, 3-D characterization of MSFCs in a number of different polycrystalline alloys. Work by Ludwig et al. [142] represents one of the early efforts to image the 3-D morphology of an MSFC within a polycrystalline volume using X-ray tomography at the European Synchrotron Radiation Facility (ESRF). In that work, grain boundaries in an aluminum alloy were decorated using liquid gallium such that the morphology of individual grains in the crack-containing volume could be observed (a similar approach was later used in [143, 144]). Additionally in [142], EBSD measurements were made to obtain information regarding crystallographic orientations on specific planes of the material. Since that time, there have been a number of efforts to characterize the morphological evolution of MSFCs using interrupted X-ray tomographic imaging (often deemed "in-situ" characterization) [143, 145, 146, 147].

By combining high-resolution X-ray tomography with 3-D X-ray diffraction microscopy (or diffraction contrast tomography [148]), a number of researchers

have gained unprecedented insight into the interaction between 3-D MSFC morphology and local 3-D crystallography (which includes grain morphologies and orientations). For example, King et al. [149] used diffraction contrast tomography followed by interrupted X-ray tomography at the ESRF to study intergranular stress corrosion cracking in austenitic stainless steel. More recently, King et al. [150] and Herbig et al. [151] used the same techniques at the ESRF to study 3-D propagation of MSFCs from focused-ion-beam starter cracks in magnesium and titanium alloys, respectively. The reader is referred to a recent review article by Withers and Preuss [152] for a more complete description of studies involving X-ray tomography, with or without X-ray diffraction methods, to characterize MSFC evolution.

3.1.3 Scope of Current Work

The purpose of this chapter is to describe a methodology to characterize the 3-D morphological evolution and underlying crystallography of naturally nucleated MSFCs using a combination of "post-mortem" (i.e. after failure) observations, including quantitative fractography, X-ray computed tomography, and near-field high-energy X-ray diffraction microscopy (HEDM). The method described herein serves as an alternative to in-situ characterization techniques (i.e. 3-D X-ray diffraction with interrupted X-ray tomography) and has fewer restrictions in terms of size and geometry of fatigue specimen, frequency of loading, and duration of mechanical testing (e.g. due to beam-time allocations).

The method is described by its application to an Al-Mg-Si alloy extracted from an engineered structure. The structure of interest is the liner component of a

composite-overwrapped pressure vessel (COPV). COPVs are used extensively to transport and store pressurized fluids in both commercial and space-flight applications [153, 154]. They typically comprise a metallic liner overwrapped by a light-weight composite material. Recent focus has been placed on "ultrathin" (e.g. wall thickness ≈0.15-0.75 mm) COPV liners [5, 97], in which the number of grains through the thickness varies from tens of grains to just several grains. Hence, the majority of through-thickness crack evolution in an ultrathin COPV liner is likely to occur within the MSFC regime.

Section 3.2 describes the experimental and post-processing methods that enable post-mortem quantification of the 3-D rate of propagation and underlying crystallography for a naturally nucleated MSFC. Section 3.3 is divided into two subsections: one that provides a general discussion of the post-mortem MSFC-characterization method and its salient features followed by a second, more pointed discussion of results from the Al-Mg-Si specimen. Finally, conclusions are provided in section 3.4.

3.2 Experimental Method

The material used in the study is an Al-Mg-Si alloy (Table 2.1) received in the form of a cylindrical COPV liner with a wall thickness of 2.3 mm. EBSD data collected at several locations reveal significant microstructural variation along the length of the liner, as shown in Fig. 3.1. Manufacturing details of the liner are provided in 2.2.

The fatigue-specimen geometry shown in Fig. 2.3 was used in the present study.

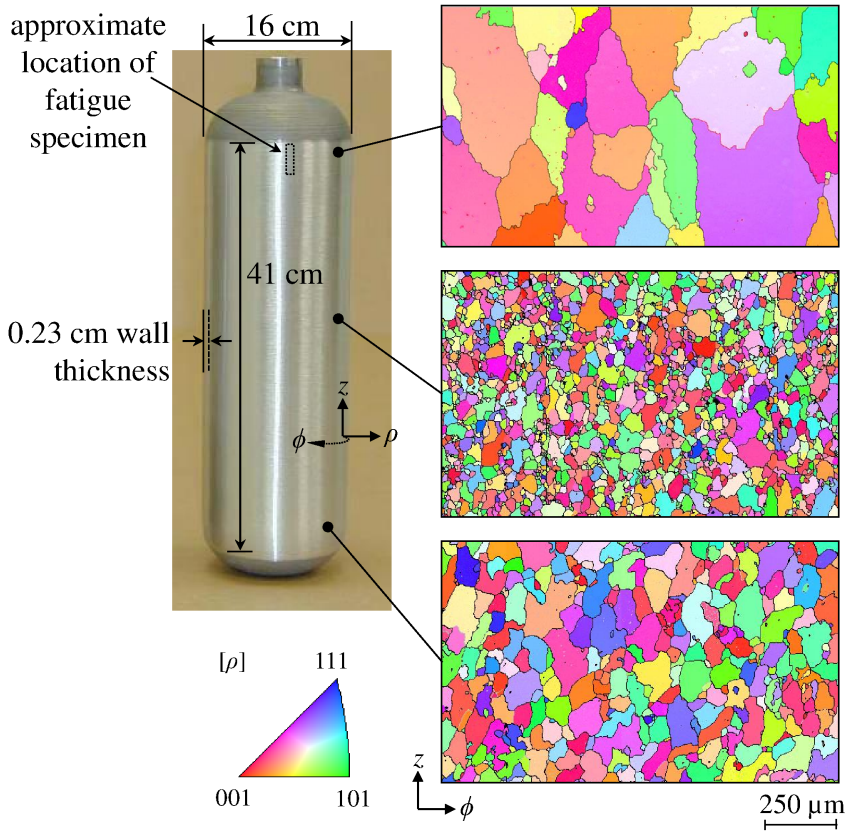

Figure 3.1: As-received COPV liner showing approximate dimensions and microstructural variation along length of cylindrical region. A cylindrical coordinate system is used as reference: z, longitudinal; ρ, radial; ϕ, circumferential.

The specimen was extracted from the cylindrical region near the port-end of the liner using wire EDM. The average grain size in that region of the liner is on the order of 100 µm. After machining, the specimen was chemically milled[1] and subsequently electropolished to a final gauge-region thickness of 400 μm, removing any damage left by the wire EDM process. EBSD measurements were made on the shallow-notched surface in a 1 mm-high band spanning the thinnest region, where crack nucleation was expected.

[1]The chemical milling procedure and its effect on fatigue-crack initiation and total life are detailed in Chapter 2.

3.2.1 Fatigue Testing

The fatigue specimen was cycled in lab air under load control using a loading spectrum designed to generate marker bands on the fatigue-crack surface. The loading spectrum is similar to that used in [141] for an Al-Zn-Mg-Cu alloy. Constant-amplitude loading was applied in the z direction with a loading ratio, R, of 0.5 and a frequency of 10 Hz. A maximum load, P_{max}, of 1.0 kN was applied, resulting in a maximum-principal notch strain around 1.0% (based on previous digital image correlation measurements [5]). Constant-amplitude baseline loading was interrupted every 10,000 cycles by groups of 25-cycle load blocks that alternated between $R = 0.1$ and $R = 0.5$, while P_{max} remained constant. A schematic of the loading spectrum is provided in Fig. 3.2, where the constant-amplitude baseline loading is shown in black and the marker-load blocks are shown in gray. The marker-load blocks served to demarcate the crack front every 10,000 cycles by imprinting either eight, six, or four marker bands, as shown in the micrographs of Fig. 3.2. In [141], the effect of interrupting baseline loading with cycles that had a lower R value but maintained the same P_{max} was determined to be inconsequential compared to the overall crack growth due to baseline loading. This is presumed to be true in the current example as well, especially considering that the marking cycles account for just 2.0% to 3.8% of the total number of loading cycles applied during any given interval.

The marker-banding technique was supplemented by periodically (typically every 50,000 cycles) interrupting the fatigue test, carefully bracing then removing the specimen from the load frame, and imaging the specimen using SEM. Doing so provided images of the surface-crack trace at known cycle counts, which were later used to register marker bands on the fatigue-crack surface.

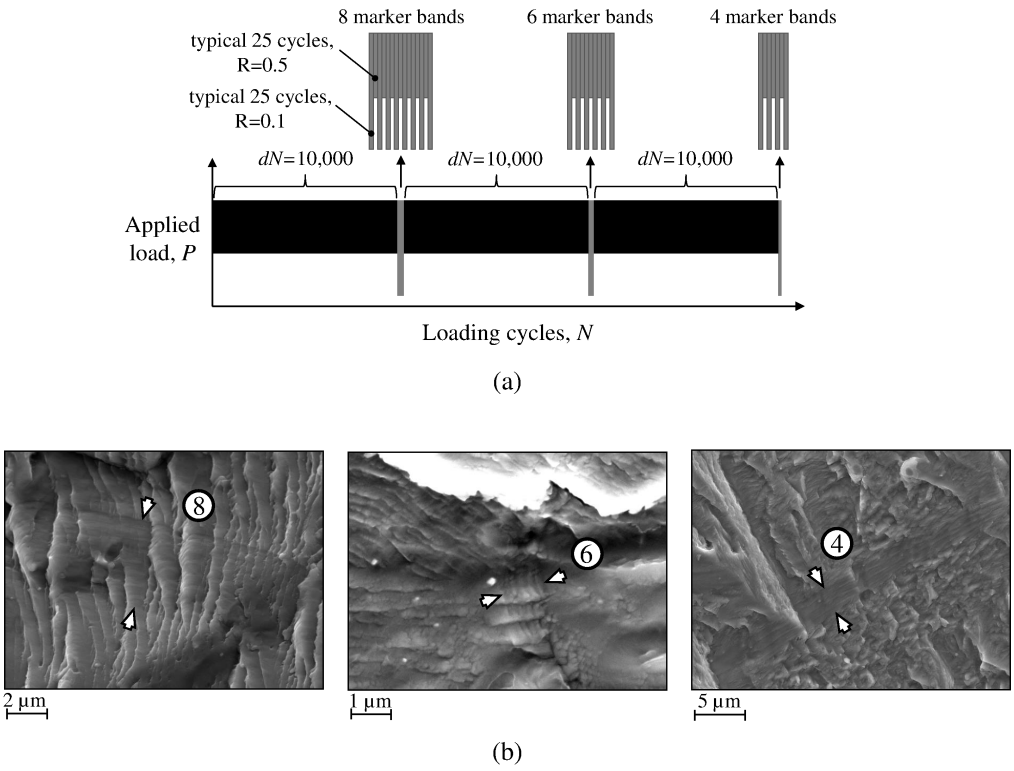

Figure 3.2: Fatigue loading spectrum (repeated until failure) and corresponding marker bands produced on fatigue-crack surface. a) Black blocks represent baseline loading at $R = 0.5$; gray blocks represent marker-band loading. A detailed view of each marker-band loading pattern is shown above each corresponding gray block. b) Eight, six, and four marker bands shown under high magnification.

Following fatigue failure, wire EDM was used to machine a 1-mm-wide strip from each half of the broken specimen (see Fig. 3.3). The strips were centered about the dominant crack-nucleation site, which was clearly identified by the appearance of river-like features emanating from the site on the fatigue-crack surface. The 1-mm-wide strips were extracted from the larger fatigue specimen to ensure that an entire volume containing the fatigue-crack surfaces could be

characterized using synchrotron radiation, which is described in a later subsection.

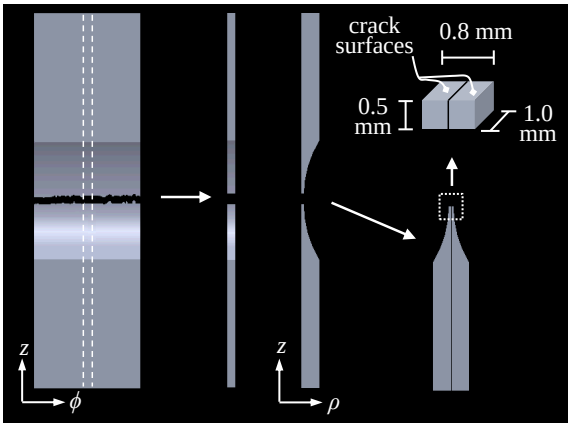

Figure 3.3: Schematic of broken fatigue specimen with dashed machining lines indicating 1 mm-wide strip containing the dominant crack-nucleation site. The halves of the 1 mm-wide strip were placed back-to-back for measurement using synchrotron radiation. Upper-right inset shows volume of material adjacent to crack surfaces characterized using X-ray tomography and near-field HEDM.

Fractography and Marker-band Identification

Fractography and marker-band analyses were performed using SEM-based imaging. The fractograph in Fig. 3.4 shows the periodic crack front profiles distinguished by the identification of marker bands. The image below the fractograph shows the trace of the crack on the notch surface that had been imaged at 250,000 load cycles, prior to failure; the crack trace is superimposed on a pristine-condition inverse pole-figure map. The crack-trace image was used to

register the cycle count of the corresponding marker band. In other words, the outermost marker band (crack front) shown in the fractograph was known to correspond to 250,000 load cycles since its intersection with the notch surface corresponds to the crack tips in the crack-trace imaged at 250,000 load cycles. Once the outermost marker band was registered, remaining marker bands were identified in reverse chronological order until the first-detectable marker band was identified nearest the crack-nucleation site.

Post-mortem X-ray Tomography and High-energy X-ray Diffraction Microscopy

Following SEM-based fractography and marker-band identification, X-ray computed tomography and near-field HEDM were used to characterize the volume of material adjacent to the exposed crack surfaces. Prior to measurement, the 1-mm-wide strips were bonded back-to-back (see Fig. 3.3) such that both halves could be measured simultaneously, which reduced the required beam time by a factor of two. The measurements were performed at the Advanced Photon Source 1-ID beamline at Argonne National Laboratory. A monochromatic beam with an energy of 50 keV was used for each measurement technique. The bonded strips were mounted such that the z axis (loading axis) was perpendicular to the incident X-ray beam.

For the X-ray tomography measurements, approximately 900 tomograms were collected over a 180° rotation of the specimen. Filtered backprojection was used to reconstruct each image in the stack of 2D images. The 2D images were then

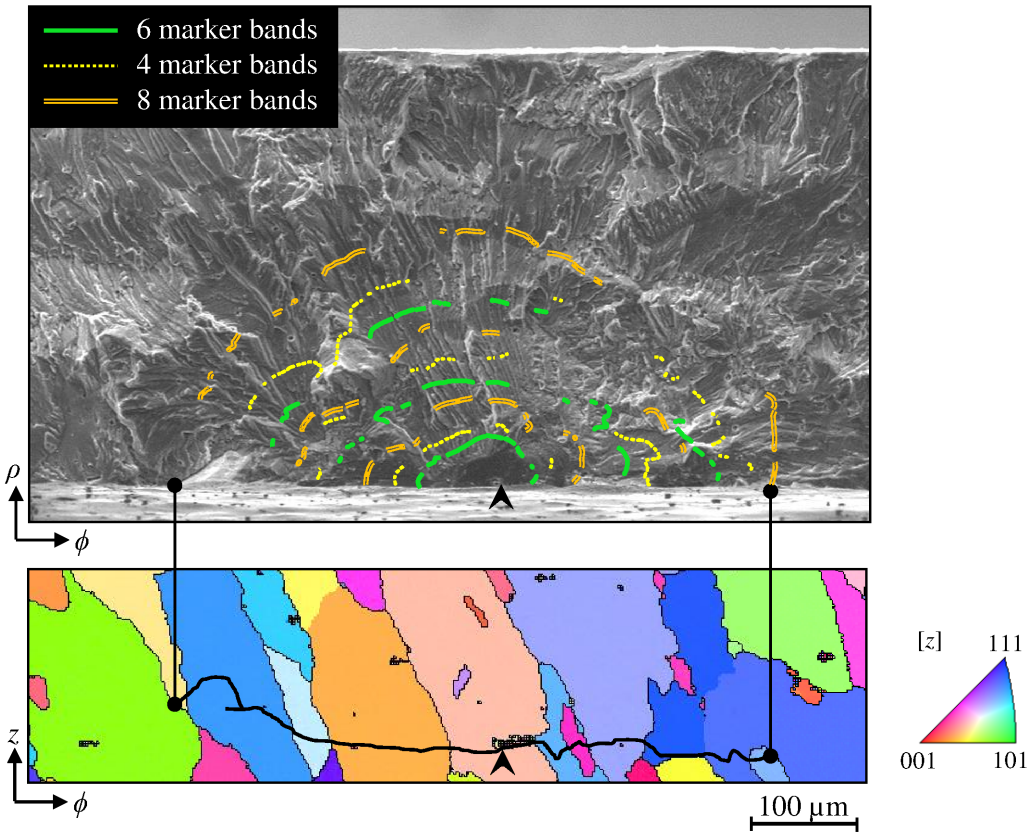

Figure 3.4: 2-D measurements in ρ-ϕ and z-ϕ planes. Top: fractograph with marker bands identified using post-mortem SEM-based imaging. Bottom: crack trace at 250,000 load cycles shown superimposed on pristine-condition inverse pole-figure map (bottom). Crack tips in the crack-trace image correspond to the intersection of outermost markerband with free surface, as depicted.

binarized using a thresholding macro written in the image processing software, Image J (http://rsb.info.nih.gov/ij/). Reconstruction of the exposed fatigue-crack surfaces proceeded directly from 3-D reconstruction of the stacked 2D images. Spatial resolution of the tomographic reconstruction was 1.47 μm. The fatigue-crack surfaces were meshed using triangular facets with edge dimensions near the tomographic resolution. These triangular facets were later used

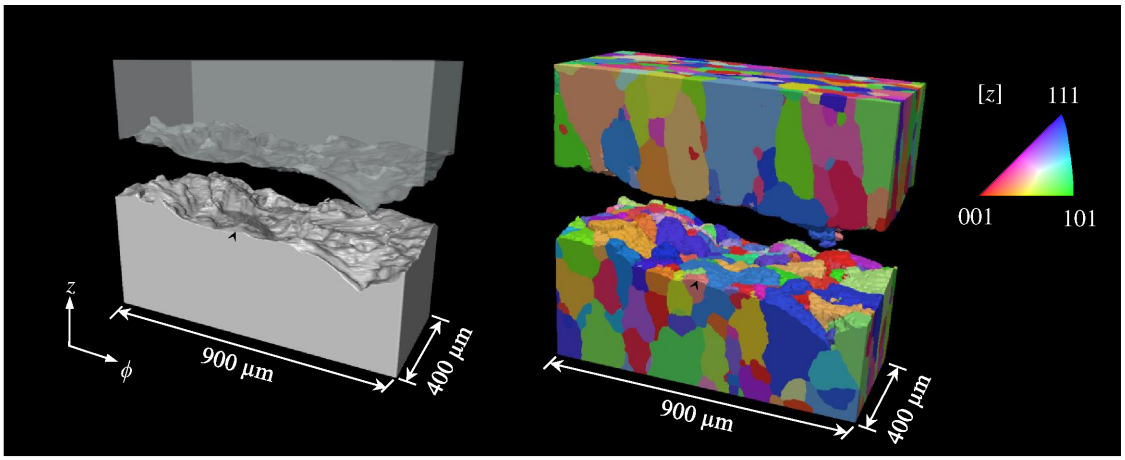

Figure 3.5: Volumetric reconstructions from X-ray tomography (left) and near-field HEDM (right). Grain orientations are depicted using inverse pole-figure maps plotted relative to the global loading direction, z. Black arrows in all images indicate location of crack nucleation.

to quantify crack-surface crystallography, described in the next subsection.

Near-field HEDM measurements were collected as follows. For a given cross section of the specimen illuminated by the monochromatic X-ray beam, X-ray diffraction spots were detected for grains satisfying the Bragg condition. Diffraction spots were captured at 180 contiguous, 1°-integration intervals as the specimen rotated about the z axis. The specimen stage was then translated vertically 6 μm along the rotation axis, and a new set of diffraction images was collected in the newly illuminated plane of the specimen. The process was repeated over the height of material to be measured (see measured volume in Fig. 3.3). In the near-field HEDM technique, individual diffraction spots are related to the orientation, spatial position, and geometry of the diffracting grains, thus enabling reconstruction of grain orientations and 3-D morphologies in a non-

destructive manner. The spatial resolution in the current application was 2 μm in the ρ-ϕ plane and 6 μm in the z direction. The reader is referred to [155] and [156] for complete descriptions of the near-field HEDM technique and forward-modeling algorithm used to reconstruct the polycrystalline volume from raw diffraction images.

Renderings of the 3-D reconstructions from post-mortem X-ray computed tomography and near-field HEDM measurements for the Al-Mg-Si specimen are presented in Fig. 3.5. In the figure, the top half of the tomographic reconstruction is shown with slight transparency to enable visual comparison of the mating fracture surfaces. In total, 794 unique grains were reconstructed from the near-field HEDM measurements.

3.2.2 Quantification of 3-D Fatigue-crack Propagation Rates

The first step in quantifying the 3-D MSFC-propagation rates was to digitize the marker-band projections identified from SEM-based fractography (i.e. from Fig. 3.4). The digitized points were then carefully fit using splines to create complete, continuous, crack-front projections in the ρ-ϕ plane. As described next, X-ray tomography-based data were incorporated to account for the 3-D crack-surface morphology in the quantification of MSFC-propagation rates.

The following algorithm was implemented for calculating 3-D MSFC-propagation rates along radial directions from the crack-nucleation site. First, for a ray at a given angle θ to the ϕ axis (see Fig. 3.6), intersection points were identified with each projected marker band. Next, the *total path length* traversed between adjacent intersection points was calculated by taking into account the z

dimension of the crack surface, which was ascertained from X-ray tomography data. This total path length was taken as da. The number of loading cycles applied between marker bands, dN, was known based on the programmed loading spectrum. Thus, calculation of crack-propagation rate, da/dN, was trivial after finding da. This procedure was repeated for 1000 values of θ ranging from 0° to 180°.

3.2.3 Quantification of Fatigue-crack Surface Crystallography

The first step involved in quantifying the crack-surface crystallography was to rotate the data for one half of the specimen by 180° about the ϕ axis (recall that prior to making the measurements, one of the strips was rotated such that the two halves could be placed back-to-back). Subsequently, landmarks throughout the fracture surface were used to align the two halves. This alignment procedure resulted in updated spatial coordinates for both the X-ray tomography and HEDM reconstructions. Additionally, the HEDM-derived Euler angles for the rotated data were updated to account for the 180° rotation of the reference frame about the ϕ axis.

After the specimen halves were aligned, crystallographic information was assigned to every triangular facet in the crack-surface mesh derived from the X-ray tomography reconstruction. The method invoked a range-tree search over the HEDM data set that associated every triangular facet in the crack-surface mesh with its "parent" grain from both the upper and lower halves of the specimen. Based on a misorientation threshold of 15° between the parent grains,

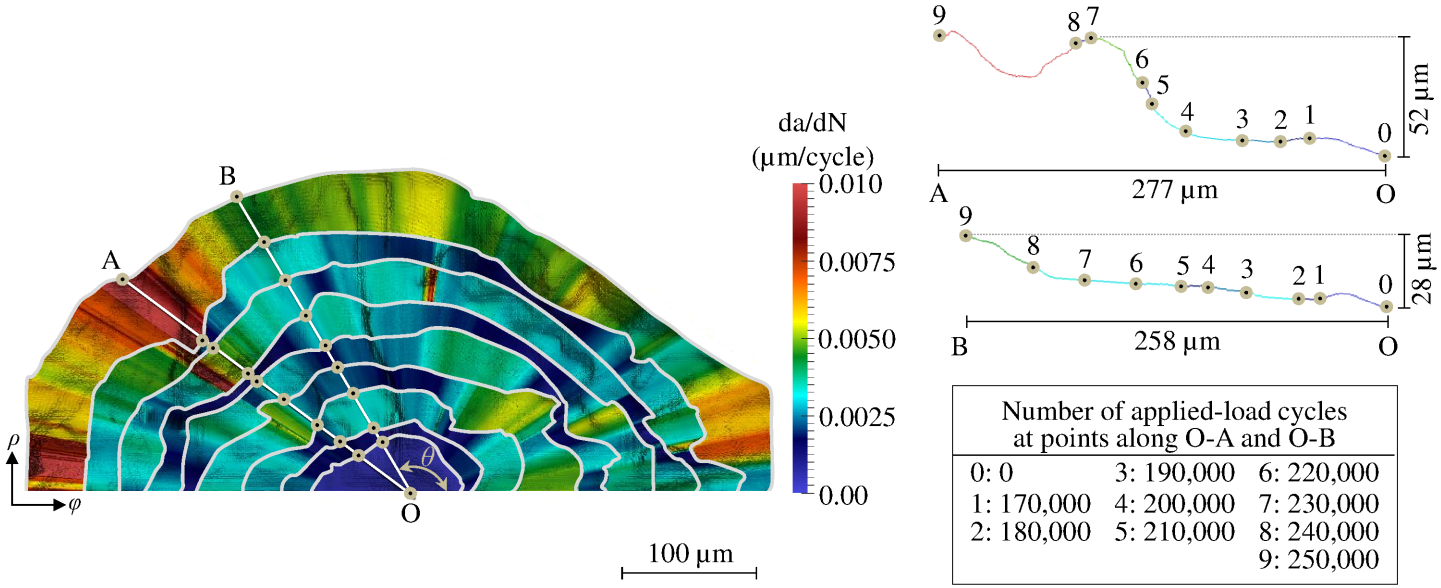

Number of applied-load cycles at points along O-A and O-B		
0: 0	3: 190,000	6: 220,000
1: 170,000	4: 200,000	7: 230,000
2: 180,000	5: 210,000	8: 240,000
		9: 250,000

Figure 3.6: 3-D fatigue-crack propagation rates based on quantitative fractography coupled with X-ray tomography measurements (maximum = 0.017 µm/cycle, minimum = 0.00035 µm/cycle). Elevation views along sections O-A and O-B are shown at right. The number of loading cycles corresponding to discrete points along O-A and O-B are provided in the table.

each triangular facet could then be identified as either intergranular or transgranular. In the latter case, the facet crystallography was quantified using a method akin to the indirect methods described in subsection 3.1.1. That is, for every triangular facet representing transgranular growth on the crack surface, the facet normal, $\hat{n}$, was calculated using the spatial coordinates of the facet's vertices. Then, $\hat{n}$ was resolved in the crystal reference frame to $\hat{n}'$ using equation 3.1 and the known Euler angles of the associated grain. In contrast to the facet-crystallography methods described in subsection 3.1.1, the current method enables quantification of crack-surface crystallography over an entire, 3-D, fracture surface at high resolutions and without having to section the specimen to interrogate internal facets.

3.3 Results and Discussion

The following subsections provide a general discussion of the post-mortem, 3-D MSFC-characterization method followed by a discussion of the specific results obtained for the Al-Mg-Si specimen.

3.3.1 3-D MSFC Characterization Using Post-mortem Measurements

Compared to traditional projection-based marker-band analyses, which restrict the measurement of crack-propagation rates to a planar projection of the crack surface [87, 90, 138, 139, 140, 141], the method described herein incorporates X-ray tomography measurements to account for the effect of 3-D crack-surface

morphology on the rate of crack propagation. To quantify this effect, the two measurement techniques were compared using the Al-Mg-Si fatigue specimen. MSFC-propagation rates were determined using the algorithm described in subsection 3.2.2, with and without incorporating the z dimension of the crack surface from X-ray tomography. The results are presented in Fig. 3.7, which show both the z-elevation deviation (dz) on the MSFC surface along with the percent increase in MSFC-propagation rates by incorporating the z dimension. The increase in MSFC-propagation rates by accounting for the 3-D morphology of the crack surface was 11% on average, with multiple regions exceeding 100%. Comparisons between the two approaches along different sections of the crack surface, O-A and O-B, are also presented in Fig. 3.8. As shown in the plot, the rates of MSFC propagation along section O-B are similar whether the z dimension is accounted for or not; whereas, the rates of propagation are underestimated along O-A when the z dimension is not considered. This can be explained by looking at the elevation views in Fig. 3.6, which show that crack growth is relatively planar along O-B but quite tortuous along O-A. The quantitative comparison between the two methods highlights the importance of including 3-D information in MSFC-propagation measurements, which will be especially necessary for the development of high-fidelity models capable of predicting local variability in complex MSFC evolution.

Compared to interrupted, "in-situ" X-ray tomographic imaging [146, 147, 150, 151], the post-mortem technique for quantifying MSFC-propagation rates presented herein yields qualitatively similar information, albeit by different approaches. In both the post-mortem and in-situ tomographic methods, the temporal resolution of the crack-front mapping depends on the frequency at which

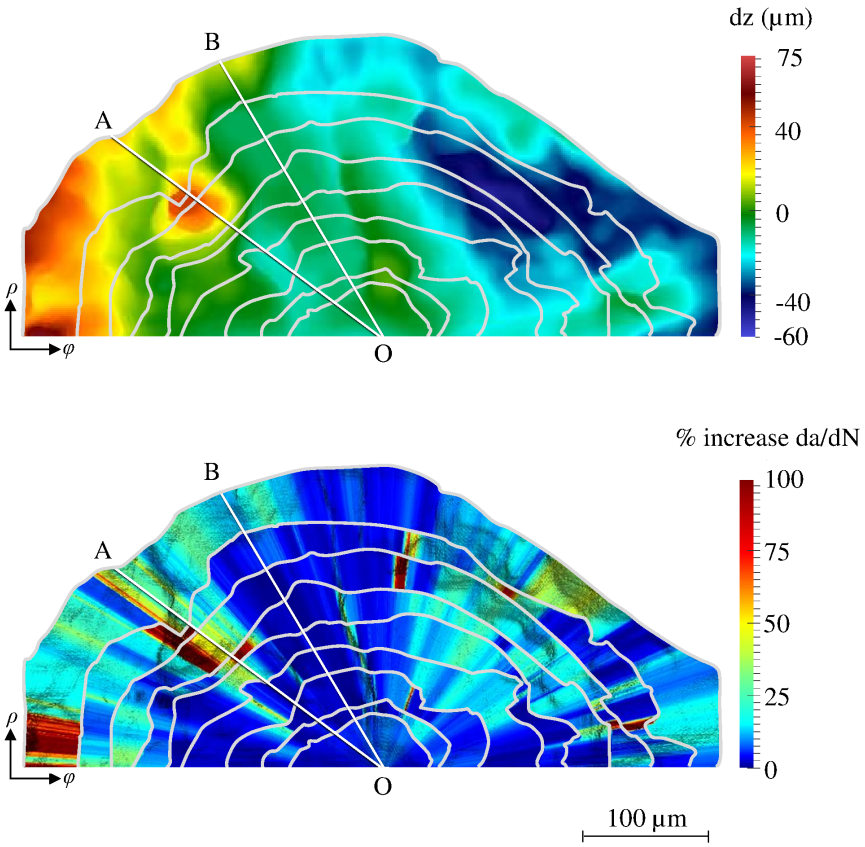

Figure 3.7: Top: contour map of fatigue-crack surface depicting *dz*, the deviation of local *z*-elevation from mean *z*-elevation on the surface. Bottom: percent increase in fatigue-crack propagation rates by incorporating X-ray tomography-based measurements versus using only SEM-based projection in the ρ-ϕ plane. Marker-band projections and sections O-A and O-B are indicated for reference.

cyclic loading is interrupted. The accuracy with which MSFCs can be reconstructed using in-situ X-ray tomography depends largely upon the following: the quality of the attenuation contrast near the crack front, where the crack opening is quite small; the resolution of the X-ray tomographic imaging; and the image-processing algorithms used to distinguish cracked and uncracked regions. In some cases, automated thresholding algorithms have been deemed

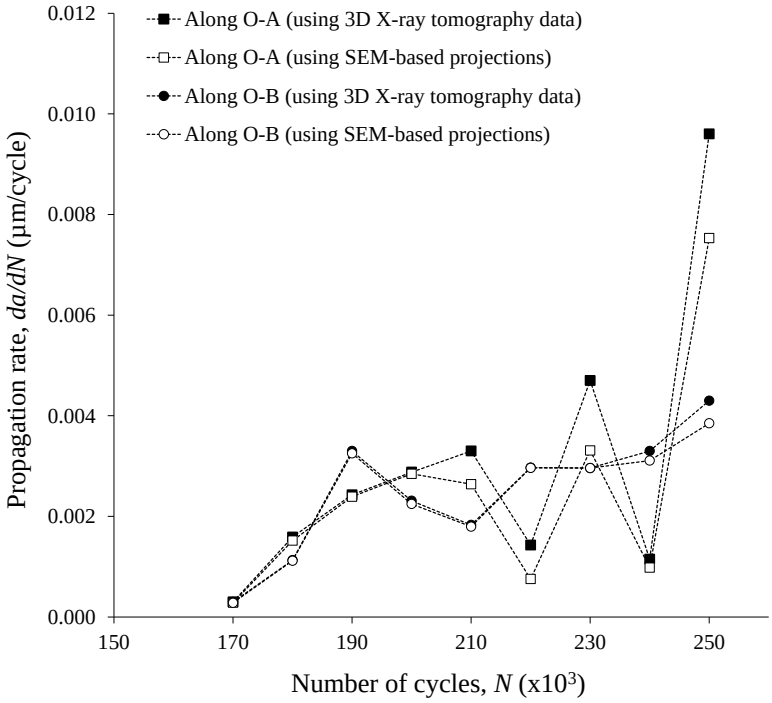

Figure 3.8: Fatigue-crack propagation rate versus number of loading cycles along sections O-A and O-B. Two different measurements are compared: 1) by incorporating X-ray tomography data to account for 3-D crack-surface morphology and 2) by using only SEM-based projection in the ρ-ϕ plane. Lines connecting the data points are meant to help visualize the four sets of data and should *not* be interpreted as crack-growth rates between data points.

insufficient to map the shape of in-situ MSFCs. In [147] and [150], for example, manual intervention was needed to trace the shape of the crack front due to difficulties associated with automated crack-front detection using image-processing algorithms. Because the post-mortem method described herein relies on SEM-based imaging of the exposed crack surface to identify crack-front profiles, the spatial resolution is comparable to, if not better than, interrupted X-ray tomography. However, it is noted that marker bands are not always distinguish-

able in some regions on the crack surface. In that case, splines can be fit through the identifiable crack-front locations. Regions where crack-front locations cannot be identified unambiguously are expected to result in greater uncertainty in their associated measurements.

To assess the accuracy with which post-mortem measurements can be used to approximate pristine-condition grain orientations, quantitative comparisons were made between post-mortem grain orientations from near-field HEDM and pristine-condition grain orientations from EBSD. Although reconstructions from near-field HEDM measurements yield a single orientation for each voxel in the volume, a post-processing step was performed on the Al-Mg-Si specimen such that a single, average, grain orientation was assigned to all voxels belonging to the same grain, which greatly reduced the overall complexity of the final reconstruction. After this post-processing step, grain-by-grain comparisons were made between EBSD data collected on the notch surface prior to loading (see pristine-condition inverse pole-figure map in Fig. 3.4) and the post-mortem near-field HEDM reconstruction (see Fig. 3.5). Of all the comparisons between corresponding grains in the two data sets, the minimum, maximum, and average disorientations were 1.57°, 4.17°, and 3.07°, respectively. For the grain in which crack nucleation occurred, the disorientation between the pristine-condition and post-mortem orientation measurements was 3.00°. Considering that the maximum surface strain exceeded macroscopic yielding on the free surface where the comparisons were made (based on previous digital-image correlation measurements [5]), the relatively small disorientation values suggest that the post-mortem measurements provide a reasonable approximation of the average grain orientations prior to mechanical loading. One possible

reason for the similarity between the pristine-condition and post-mortem grain-orientation measurements is that regions with enough permanent deformation to cause weak scattering might not be indexed and thus do not contribute to the average grain orientation measurement, as described in [91].

Overall, the method for characterizing 3-D MSFC evolution described herein has a number of salient attributes and potential for future applications. The method offers an alternative to using combined diffraction and interrupted X-ray tomography techniques, as described in section 3.1.2. One of the salient features compared to in-situ MSFC-evolution characterization is that fewer restrictions are placed on the loading conditions and geometry of the fatigue specimen since all synchrotron-based measurements in the current method are "static" and are performed on a subvolume of the original specimen upon completion of the mechanical testing. Furthermore, in the event that long-duration fatigue tests preclude the use of in-situ techniques due to limited beam-time allocation, for example, the current method offers a viable alternative. Another noteworthy feature is that the current method enables, in a relatively straight-forward manner, studies of natural fatigue-crack nucleation, thus obviating the need to insert artificial starter cracks. The method also presents a potential approach to performing detailed, comprehensive failure analyses of real structures.

3.3.2 Discussion of Results from Al-Mg-Si Specimen

The color contour map in Figure 3.6 depicts the 3-D MSFC-propagation rates over the entire MSFC surface of the Al-Mg-Si specimen. Elevation views of the crack surface for two different sections (O-A and O-B) are also shown on the

right side of Fig. 3.6, along with a table indicating the number of load cycles that correspond to discrete points along each crack path. The crack paths for the two sections originate from the crack-nucleation site, labeled "O". The elevation views along O-A and O-B provide snapshots of the variability in the crack path at different locations on the crack surface. Section lines indicating O-A and O-B are also shown in subsequent figures for reference.

A number of observations are made from Fig. 3.6 regarding the nucleation life and 3-D rates of propagation for the MSFC in the Al-Mg-Si specimen. As evidenced in the figure, the fatigue crack nucleated between 0 and 170,000 loading cycles, the latter corresponding to the earliest-distinguishable marker band on the crack surface. Failure of the specimen occurred after 279,000 loading cycles. Thus, fatigue-crack nucleation accounted for less than 61% of the total fatigue life of the specimen. Following MSFC nucleation, the 3-D rate of MSFC propagation through the specimen varied by two orders of magnitude; the minimum and maximum propagation rates were 0.00035 μm/cycle and 0.017 μm/cycle, respectively.

Regions of retardation and acceleration contributed to the significant variability in MSFC-propagation rates both between and along individual crack fronts. There were a number of instances where crack retardation at points during one interval (i.e. at points along one crack front) were followed by crack acceleration in the next interval. For example, as shown in Figs. 3.6 and 3.8, crack-growth along O-A decelerated between 210,000 and 220,000 cycles; followed by accelerated growth until 230,000 cycles; then slow growth until 240,000 cycles; followed by rapid growth until 250,000 cycles. The crack retardation along O-A

between 230,000 and 240,000 cycles occurred near an inflection point in the elevation of the crack. This can also be observed in the elevation contour map of Fig. 3.7, where the impediment occurred at the observed apex of the peak in that region. The other instance of retardation along O-A (between 210,000 and 220,000 cycles) does not correspond to an inflection in the crack-surface elevation and appears to correlate with the intersection of a grain boundary, as evidenced in Fig. 3.9.

This observed behavior of alternating retardation and acceleration has been described elsewhere for different alloys [146, 157, 158]. Through simulation of subsurface MSFC evolution in different aluminum alloys, Cox and Morris [157, 158] described this effect in terms of stress intensity factor, whereby a temporarily pinned or arrested region along a crack front experiences an amplification of the local stress intensity factor compared to its neighboring crack-front regions. The amplified local-driving force results in a subsequent local acceleration during the next interval of crack extension. Quantification of such local-driving forces (whether stress-, strain-, slip-, or energy-based) requires numerical simulation and is the topic of Chapter 4.

In the literature, crack nucleation and early propagation in aluminum alloys have been shown to occur by a number of different mechanisms, depending largely on the alloy, heat treatment, surface treatment, environment, and loading conditions. For many aluminum alloys under certain conditions, crack nucleation and early propagation have been associated with a {111} slip-based mechanism identified as Stage I cracking [120, 121, 159, 160, 161]. Alternatively, a number of studies have revealed non-slip-based mechanisms in aluminum al-

loys, often with crack paths near parallel to {001}, {101}, or high-index planes [117, 132, 135, 136, 162]. These non-slip-based observations have been attributed to environmental hydrogen-assisted cracking.

The complex evolution of the crack-surface morphology and crystallography for the Al-Mg-Si fatigue specimen are detailed in the maps shown in Fig. 3.9. Crack-surface morphology is described in terms of θ_z, the angle between the local crack-surface normal and the global loading direction, z. In the lower map describing crack-surface crystallography, black and colored regions correspond to intergranular crack propagation (i.e. crack growth along grain boundaries) and transgranular crack propagation, respectively. The colored regions represent the local crack-surface normal resolved in the crystallographic reference frame. Marker-band projections and grain-boundary traces are superimposed on each map for reference. As evidenced in Fig. 3.9, crack nucleation occurred toward the center of a grain on a near-{001} crystallographic plane with the crack-surface normal inclined 28° from the global loading direction. The observed crack nucleation on a near-{001} plane rather than a {111}-slip plane seems to be consistent with observations of environmental hydrogen-assisted fatigue cracking [117, 132, 135, 136, 162]; though, the precise mechanism cannot be substantiated from the current study.

Following crack nucleation, the 3-D MSFC-propagation behavior in the Al-Mg-Si fatigue specimen was quite complex. As shown in Fig. 3.9, there are many grains through which the crack propagated on multiple crystallographic planes, including near-{001}, near-{101}, near-{111}, and, most frequently, high-index planes. Additionally, there are regions where the crack propagated entirely

along a grain boundary, and yet other regions where crack propagation occurred both within a grain *and* along that grain's boundary. In fact, 41.0% of the entire crack surface depicted in Fig. 3.9 was intergranular (within the resolution of the HEDM reconstruction), while 59.0% was transgranular. Of the transgranular regions, approximately 25.6%, 23.0%, and 10.1% was near-parallel (within 20°) to {001}, {101}, and {111}-slip planes, respectively. The remaining 41.3% of transgranular crack surface formed along high-index planes. The intensity map shown in Fig. 3.10 depicts the distribution of facet normals for all of the transgranular surface area, plotted within the irreducible stereographic triangle of crystal space. Though there is not an overwhelming preference of the crack to grow along any particular set of crystallographic planes, Fig. 3.10 nonetheless shows slight intensities of crack facets near-parallel to {001} and {101} planes, with fewer crack facets near-parallel to {111}, which is consistent with observations from Fig. 3.9 and the quantities described above.

Of the entire crack surface shown in Fig. 3.9, 31.8% evolved approximately normal (within 20°) to the global loading direction, which corresponds to dark-blue regions in the colored map of θ_z. Much of the crack path along section O-B, for example, spanned multiple grains yet remained approximately normal to the z direction. The elevation view of O-B in Fig. 3.6 depicts the relatively planar growth normal to the z direction in this region between 170,000 and 240,000 load cycles.

Inherently, features on the crack surface that have spatial dimensions below the resolution of the tomographic reconstruction, e.g. nano-scale crystallographic facets or steps, cannot be resolved using the current technique. This implies

that the local crystallography and morphology described above represent values averaged over each triangular facet in the crack-surface mesh, which has been discussed elsewhere by Herbig et al. [151]. Though it may not be possible using the current measurements to assess the physics of crack evolution operating below this resolution limit, the quantitative results that have been obtained for the Al-Mg-Si alloy will be very useful in grain-scale modeling efforts [133]. More detailed and quantitative analyses relating the 3-D rates of propagation to the underlying microstructure are the topic of parallel studies by the authors and will be detailed in forthcoming publications.

3.4 Conclusions

An experimental method along with post-processing techniques are presented for quantitatively characterizing the 3-D evolution of naturally nucleated microstructurally small fatigue cracks (MSFCs) in an Al-Mg-Si alloy using a combination of post-mortem measurements. A specially designed loading spectrum periodically demarcates the shape of the crack-front on the fatigue-crack surface. Following specimen failure, SEM-based quantitative fractography is combined with X-ray tomographic reconstruction of the crack-surface morphology to quantify 3-D rates of MSFC propagation. Reconstructions from post-mortem high-energy X-ray diffraction microscopy (HEDM) enable quantification of crack-surface crystallography. Based on results from the study, the following conclusions are made regarding the post-mortem MSFC-characterization method:

- Compared to fractography-based techniques that rely on SEM-based stere-

ology (coupled with diffraction data) to quantify crystallography of individual facets on crack surfaces, the current method enables quantification of crystallography over entire 3-D crack surfaces at high resolutions (1.47 μm resolution in the current application).

- Compared to fractography-based techniques that rely on planar projections of the crack surface to quantify subsurface crack-growth rates (e.g. marker-band analyses using SEM-based imaging), the current method provides a more complete and detailed description of local crack-growth rates by accounting for the 3-D crack-surface morphology. Results from the Al-Mg-Si specimen show that projection-based measurements underestimate MSFC-propagation rates and that, by accounting for the 3-D crack-surface morphology, the increase in local MSFC-propagation rates was 11% on average, with multiple regions on the crack surface exceeding 100%.
- Compared to "in-situ" methods that use interrupted X-ray tomographic imaging to characterize crack morphology at discrete load-history intervals, the post-mortem technique described herein offers a number of salient benefits, including fewer restrictions on fatigue-specimen geometry, type and frequency of loading, and duration of mechanical testing. Additionally, the post-mortem technique avoids issues related to resolving the precise geometry of in-situ cracks having openings below the limits of detectability.

To the author's knowledge, application of the current method yielded unprecedented measurements of a 3-D MSFC in an aluminum alloy in terms of local, 3-D, rates of propagation combined with local crystallography (based on 3-D grain morphologies and orientations).

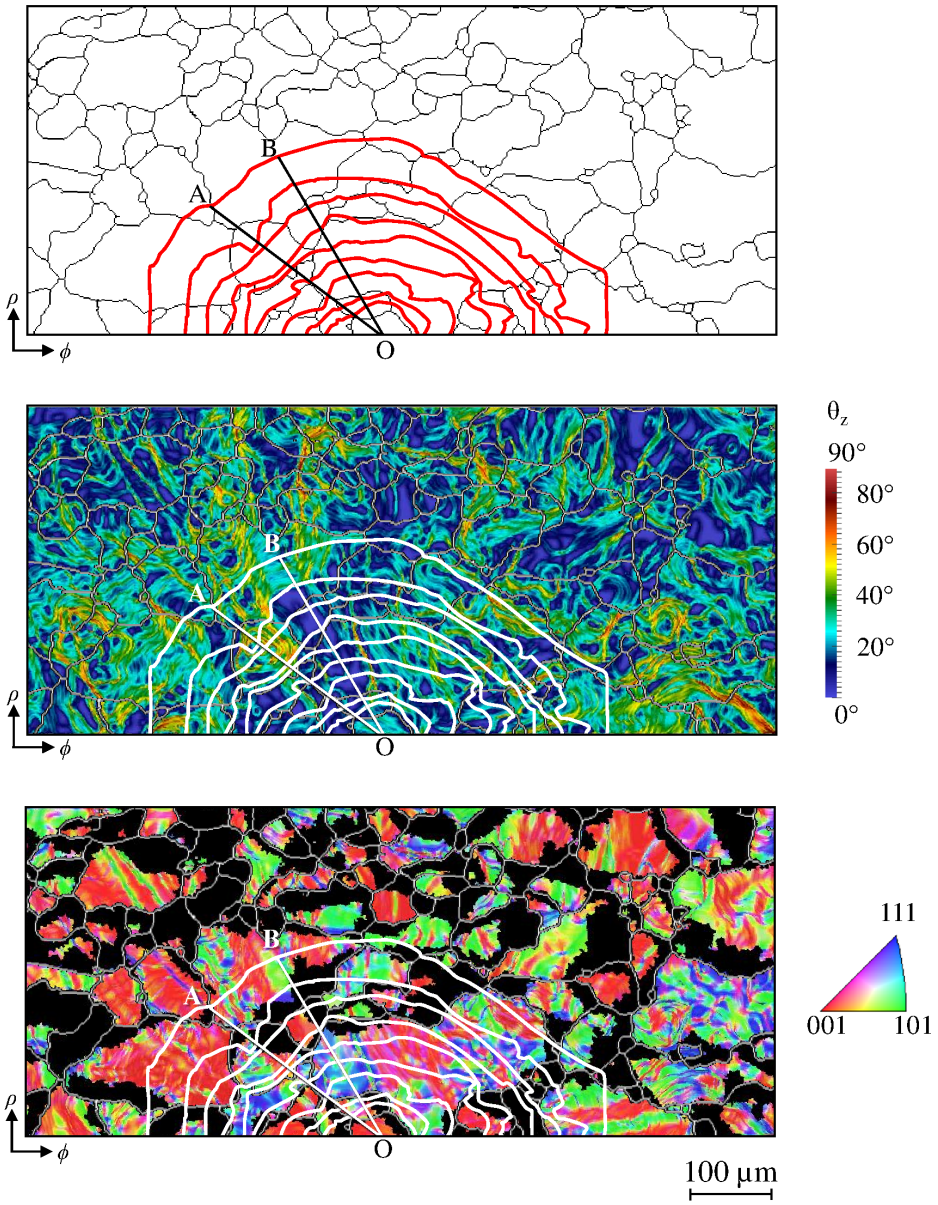

Figure 3.9: Top: grain-boundary intersections with crack surface and marker-band projections superimposed in red. Middle: detailed crack-surface morphology with color contours representing θ_z, the angle between local crack-surface normal and global loading direction, z. Bottom: detailed crack-surface crystallography with color contours representing local crack-surface normals resolved in crystal reference frame for transgranular crack propagation; black regions correspond to intergranular crack propagation.

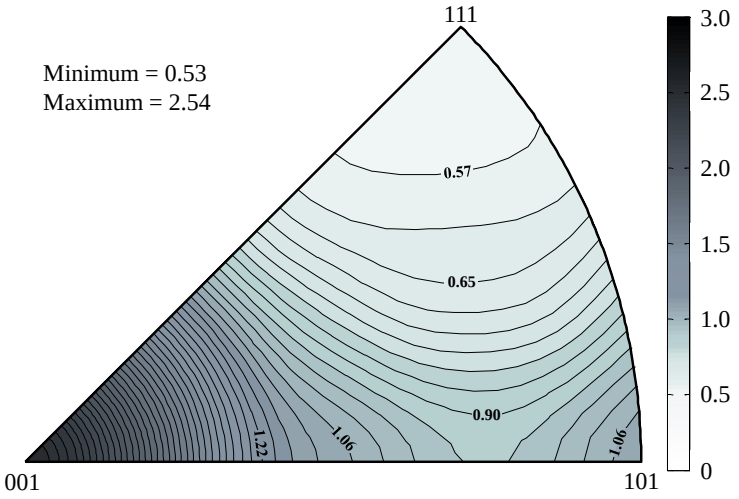

Figure 3.10: Facet-normal distribution (in crystal reference frame) for transgranular regions shown in Fig. 3.9. Intensity expressed in multiples of random.

CHAPTER 4

THREE-DIMENSIONAL NUMERICAL MODELING OF MICROSTRUCTURALLY SMALL FATIGUE-CRACK EVOLUTION IN AN AL-MG-SI ALLOY

4.1 Introduction

Within the past decade, combined improvements in parallel computation, constitutive models, and high-resolution materials characterization have enabled high-fidelity modeling of material deformation and cracking across multiple length scales [163, 164]. A common motivation for such modeling efforts is to facilitate the development of advanced structural-prognosis/health-monitoring systems and to enable materials design and optimization. A significant hindrance to achieving these objectives, however, is that most existing relationships or "rules" for predicting fatigue-crack growth (e.g. based on Paris law) are applicable in limited cases and only at a length scale where cracks are relatively large compared to the underlying microstructure. Such relationships cannot capture the evolution of a fatigue crack within the microstructurally small regime, where the formation and early propagation of a fatigue crack can account for a significant portion of, and can contribute much scatter to, the total fatigue life of structural components. While there has been some work to develop relationships to predict crack propagation at the microstructural length scale (e.g. based on cyclic crack-tip displacement [165, 166]), such relationships are semi-empirical and remain largely untested, especially in 3D. Thus, there remains a great need to discover and validate physics-based rules that govern fatigue-crack propagation within real materials at the microstructural length

scale. The reader is referred to McDowell [163] and McDowell and Dunne [164] for a description of the current state of modeling in terms of multiscale plasticity and microstructurally small fatigue crack (MSFC) formation, respectively.

Until recently, a lack of 3-D data at the grain scale for polycrystalline materials has limited numerical models of MSFCs to: strictly 2-D replications (e.g. [167]); 2-D replications extruded in the third dimension (e.g. [122, 129, 168, 169, 170]); synthetic or virtual microstructures, either in 2D (e.g. [171]) or 3D (e.g. [172, 173]); or single-crystal replications (e.g. [174, 175]). Many researchers have found that MSFC observations and computations made on the free surface are not indicative of the subsurface behavior due to effects of both constraint and crystallography. For example, as described by both Cuitiño and Ortiz [174] and Flouriot et al. [175], the strain fields in single-crystal four-point-bend and compact-tension specimens, respectively, were found to be highly three-dimensional and dependent on the orientation of the single crystal; consequently, fields on the free surface were not indicative of fields through the thickness. Another important point to make here is that a trace observed on the free surface (e.g. caused by a slip plane, grain boundary, or crack) is insufficient to characterize uniquely the plane from which that trace is formed. Thus, as mentioned in [164], there is a tremendous need for 3-D measurements of MSFC evolution at the microstructural length scale to support and validate MSFC modeling efforts, especially for the regime of MSFC propagation.

A particularly exciting development within the last decade in the area of 3-D materials characterization is that of near-field high-energy X-ray diffraction microscopy (HEDM), a non-destructive synchrotron-based imaging technique that

enables mapping of 3-D grain morphologies and orientations for relatively bulk volumes of polycrystalline materials [91, 155, 156, 176, 177]. Work involving near-field HEDM (or a similar technique called diffraction contrast tomography [148]) to characterize MSFCs in polycrystalline alloys is described by King et al. [149, 150], Herbig et al. [151], and in Chapter 3 of this work.

The objective of this chapter is to extend the work from Chapter 3 by generating 3-D finite-element (FE) models that explicitly represent the measured 3-D microstructure (including grain morphologies and orientations) and MSFC geometry at particular instances during the load history of the Al-Mg-Si specimen described in Chapter 3. A concurrent multiscale model is created to link the measured polycrystalline region with the macroscale specimen. Simulated loading is applied, and fields are computed that could not otherwise be measured from the experiment (e.g. stress, strain, slip). To the author's knowledge, this is the first time that a naturally nucleated MSFC has been modeled numerically within a measured, 3-D microstructure (including grain morphologies and orientations) for a polycrystalline material.

4.1.1 Review of Previous Work

Recall, in Chapter 3, a combination of 3-D measurement techniques was used to quantitatively characterize MSFC evolution in a polycrystalline volume of an Al-Mg-Si alloy. An existing approach known as marker banding was used to imprint the shape of sequential crack fronts on a fatigue-crack surface at specified intervals during the loading history. Following specimen failure, the crack-front profiles were identified using SEM-based fractography, which provided

intervals of crack-growth rates on a projected 2-D plane of the crack surface. To quantify MSFC propagation in a 3-D sense, the marker-band projections were combined with a 3-D description of the fatigue-crack surface obtained using post-mortem X-ray computed tomography. The results revealed a wide range of fatigue-crack growth rates over the observed fatigue-crack surface. In addition to X-ray computed tomography, near-field HEDM was used to quantitatively characterize the 3-D grain morphologies and orientations in a volume adjacent to the exposed crack surfaces of the broken fatigue specimen. The near-field HEDM and X-ray tomography data sets were combined to provide a high-resolution, quantitative description of the crystallography over the entire 3-D crack surface. The work described in Chapter 3 provides both a demonstrated method for obtaining 3-D MSFC data as well as a novel data set for 3-D MSFC propagation in an aluminum alloy.

The reader is referred to a number of relevant figures from Chapters 2 and 3. Figure 2.3 provides dimensions of the Al-Mg-Si fatigue specimen, which is modeled in the current work. Figure 3.3 shows the volume of material that was characterized in Chapter 3 using X-ray tomography (1.47 μm spatial resolution) and near-field HEDM measurements (2-6 μm spatial resolution). Figure 3.5 depicts the results from those measurements. In total, approximately 794 unique grains were measured in the volume shown. Finally, Fig. 3.6 provides 3-D fatigue-crack growth rates for the specimen based on the experimental procedure developed in Chapter 3. Note that in Fig. 3.6, the measured crack-front profiles (shown in white on the color-contour map) correspond to the cycle counts provided in the accompanying table. The coordinate system adopted in the previous work and shown in Figs. 2.3-3.6 is adopted here for consistency.

4.2 Numerical Modeling Method

The fatigue specimen shown in Fig. 2.3 is modeled using a concurrent multiscale modeling approach, whereby a grain-scale FE model of the measured polycrystalline volume is directly embedded into a macroscale FE model of the larger specimen. The following subsections detail the process implemented to convert the 3-D experimental data set from the broken fatigue specimen described in Chapter 3 into a digital reconstruction: first, by generating a "watertight", fully populated, volume of voxels for the grain-scale region (subsection 4.2.1); then, by converting the voxelized data set into a 3-D FE mesh (subsection 4.2.2); and finally, by merging the grain-scale mesh with a macroscale mesh to complete the multiscale topological description (subsection 4.2.2). Section 4.2.3 describes the material models used at each length scale. Finally, section 4.2.4 provides simulation details, including boundary conditions and model sizes for three instantiations of the measured, 3-D, crack shapes that are numerically reproduced.

4.2.1 Digital Reconstruction of Grain-scale Volume from 3-D Experimental Data

In order to reproduce the observed MSFC evolution using numerical modeling, the synchrotron-based data set from the broken fatigue specimen shown in Fig. 3.5 is first converted to a volume that is fully merged and continuous across the crack interface. The HEDM data from the two halves of the broken specimen are first brought into close alignment with each other as described in Chapter

3, essentially by relying on landmarks over the fracture surface to rotate and translate the halves into coincidence with each other. However, because the two fracture surfaces do not align perfectly[1], a digitized volume is created that is continuous and completely "water tight" across the crack interface. The volume of interest is comprised of voxels, where each voxel is associated with its parent grain ID from the near-field HEDM data. The following algorithm is implemented to generate the merged, voxelized volume.

First, a volume of interest is defined by (1) the bounding-box coordinates and (2) the desired resolution of the volume, or voxel size. Next, for each voxel in the volume, the spatial coordinates are used to determine whether the voxel exists above or below the crack surface. If the voxel is above the crack surface, the near-field HEDM data from the upper half of the broken specimen will define the search domain to be queried; if the voxel is below, the data from the lower half will be queried. Finally, based on the appropriate query space, the voxel is associated with its parent grain by performing a range-tree search for its nearest neighbor. The algorithm requires every voxel in the digital volume to be associated uniquely with a parent grain ID, thus fully populating the voxelized space.

Figure 4.1 depicts the algorithm schematically in 2D. Figure 4.1(a) shows a 2-D grain map representative of data collected for the upper and lower halves of the broken fatigue specimen. Figure 4.1(b) shows the region of interest to reconstruct, which is defined by the bounding box of the region and the resolution of the grid spacing. Each dot in the grid represents a point (voxel in 3-D space) that is, at first, unassociated with any grain ID. Finally, Fig. 4.1(c) shows the digi-

[1]For example, real and artificial gaps may exist at the interface of the two halves as a result of plastic deformation and errors that arise in the HEDM measurements along the crack surface.

tal reconstruction of the fully merged specimen that results from executing the above-described algorithm, where each point is colored based on its associated parent grain ID. Figure 4.2 shows an 800 x 400 x 600 μm^3 digitally reconstructed voxelized volume for the fatigue specimen characterized in Chapter 3; the voxelized reconstruction approximates the merged polycrystalline volume prior to the existence of an MSFC. The resolution of the voxelized volume in Fig. 4.2 is 2 μm.

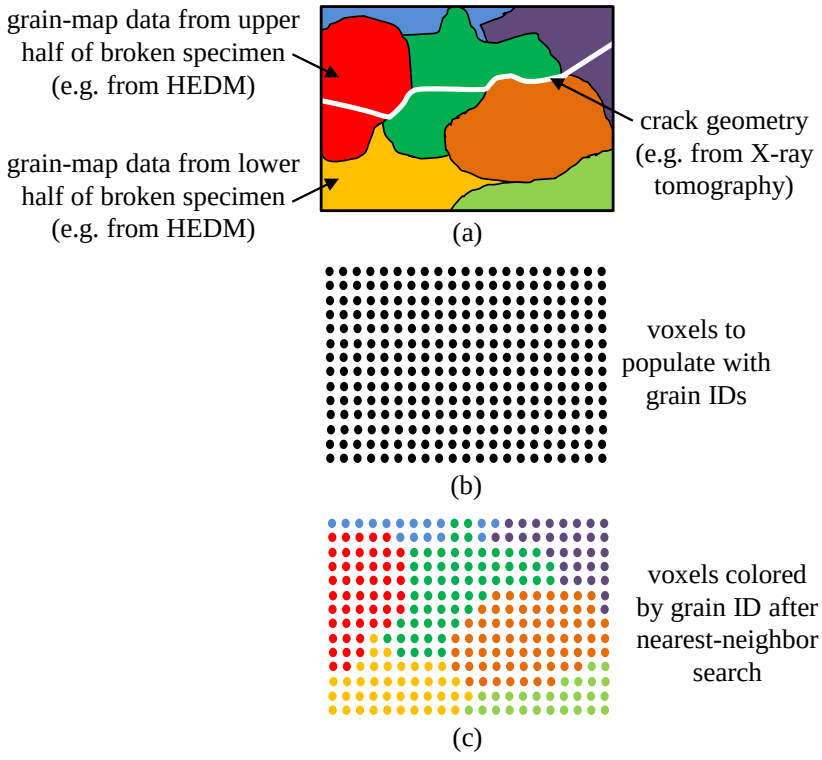

Figure 4.1: 2-D illustration of "merging" broken halves using grain ID-assignment algorithm for a defined space of points (voxels in 3-D space) based on a nearest-neighbor search over the upper-half and lower-half data sets.

The above algorithm is modified to *implicitly* represent, within the voxelized reconstruction, the MSFC geometry measured at a particular cycle count during

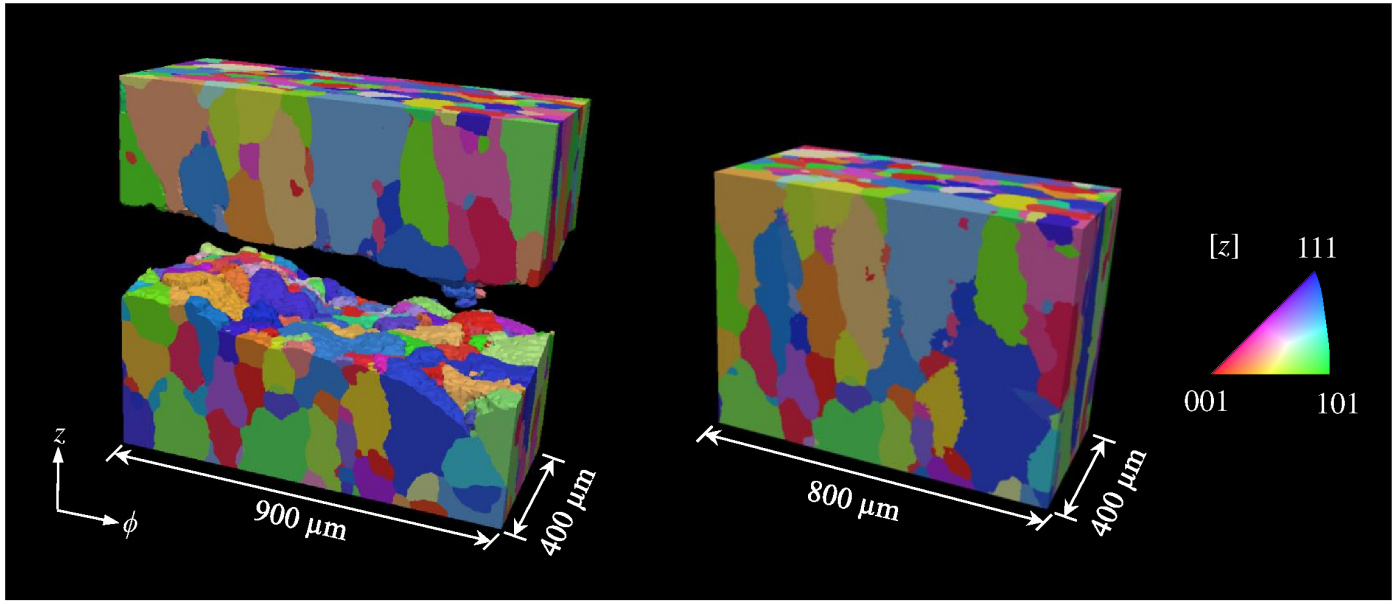

Figure 4.2: Left: experimental data from near-field HEDM measurements of broken fatigue specimen (see Chapter 3). Right: fully populated volume of voxels representing the merged specimen following the algorithm described in 4.2.1. Inverse pole figure coloring relative to global loading direction.

the loading history. The modification is made by assigning special identifiers to the grain IDs of voxels that exist within the cracked region at the cycle count of interest. In particular, each voxel located anywhere in the z direction either below or above the traction-free surface at the cycle count of interest is given a grain ID that begins with '100' or '200', respectively. For example, if grain ID '426' is cracked at the cycle count of interest, the algorithm will assign grain ID '100426' to the voxels of that grain on the lower side of the traction-free surface and '200426' to the voxels of that grain above the traction-free surface (note, the original grain ID '426' will be assigned only to voxels that exist in the uncracked region). A 2-D illustration of the grain-ID renumbering scheme is shown in Fig. 4.3. The purpose of subdividing the voxelized space by grain IDs in this way is to enable subsequent meshing routines to create a boundary along the crack surface, thereby explicitly incorporating the history-dependent MSFC geometry into the FE mesh (described in subsection 4.2.2).

Figure 4.4 provides a 3-D description of the subdomains that are used to renumber grain IDs as described above. In Fig. 4.4, the upper image depicts the voxelized volume of interest with the fatigue-crack surface (derived from X-ray computed tomography in Chapter 3) partitioning the space into subdomains 1 and 2, analogous to the 2-D schematic in Fig. 4.1. The lower image in Fig. 4.4 shows the crack surface with the observed crack-front profile, or marker band, corresponding to 180,000 cycles of loading (from Fig. 3.6). The marker band serves to partition the voxel space into subdomains 3 and 4, i.e. voxels located within the cracked or uncracked regions, respectively. The modified algorithm for implicitly incorporating a specific crack geometry into the voxelized volume is shown in Fig. 4.5. Note that compared to the algorithm described earlier for

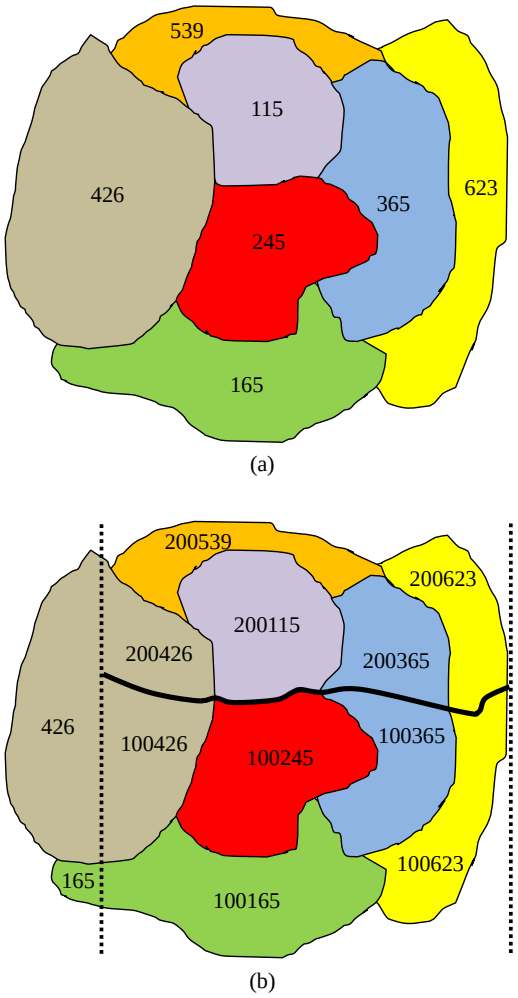

Figure 4.3: 2-D illustration of implicitly representing crack within the voxelized reconstruction based on grain-ID renumbering. (a) Original grain IDs for the merged, uncracked volume. (b) Renumbered grain IDs based on voxel location relative to history-depend crack geometry; all voxels within the traction-free region (i.e. between the dashed lines) for the depicted crack geometry have unique identifiers appended to original grain ID.

reconstructing the merged and uncracked volume, the algorithm shown in Fig. 4.5 simply appends an identifier to the grain ID of a voxel if that voxel is within subdomain 3 for the history-dependent MSFC geometry of interest.

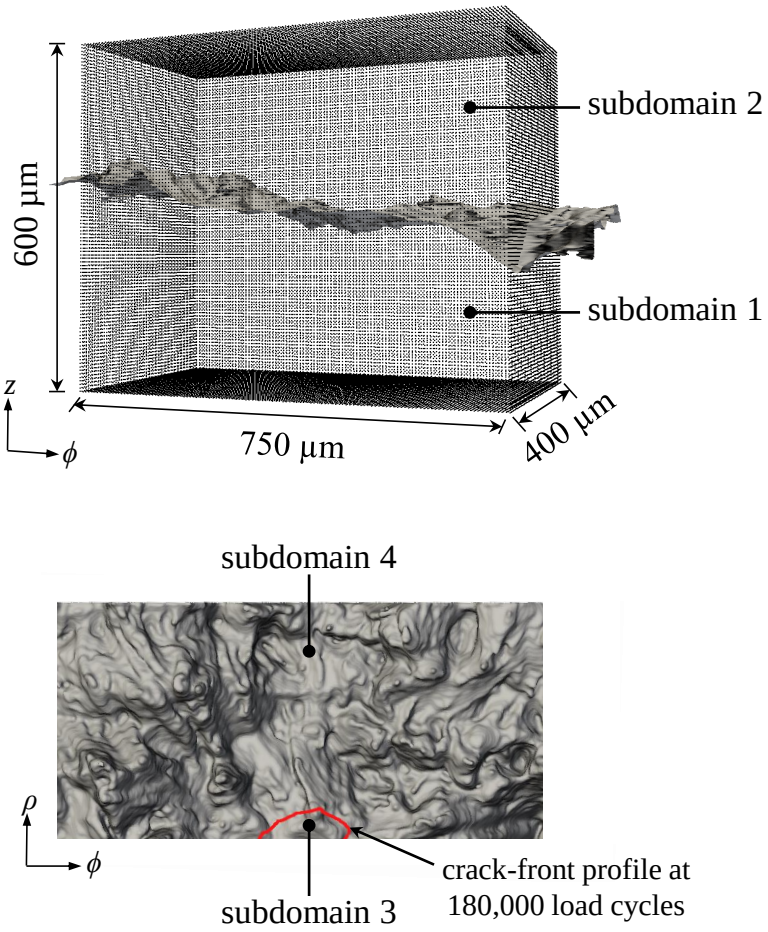

Figure 4.4: Subdomains used to identify and assign grain IDs to each voxel in a volume of interest following the algorithm shown in Fig. 4.5. Subdomains 1 and 2 correspond to data below and above the 3-D crack surface, respectively. Subdomains 3 and 4 correspond to data inside and outside of a particular crack front, respectively.

Figure 4.6 shows the digitally reconstructed voxelized volume that incorporates the renumbered grain IDs based on subdomains for the fatigue crack at 180,000 cycles of loading. Figures 4.6(a) and 4.6(b) depict the voxelized volume colored

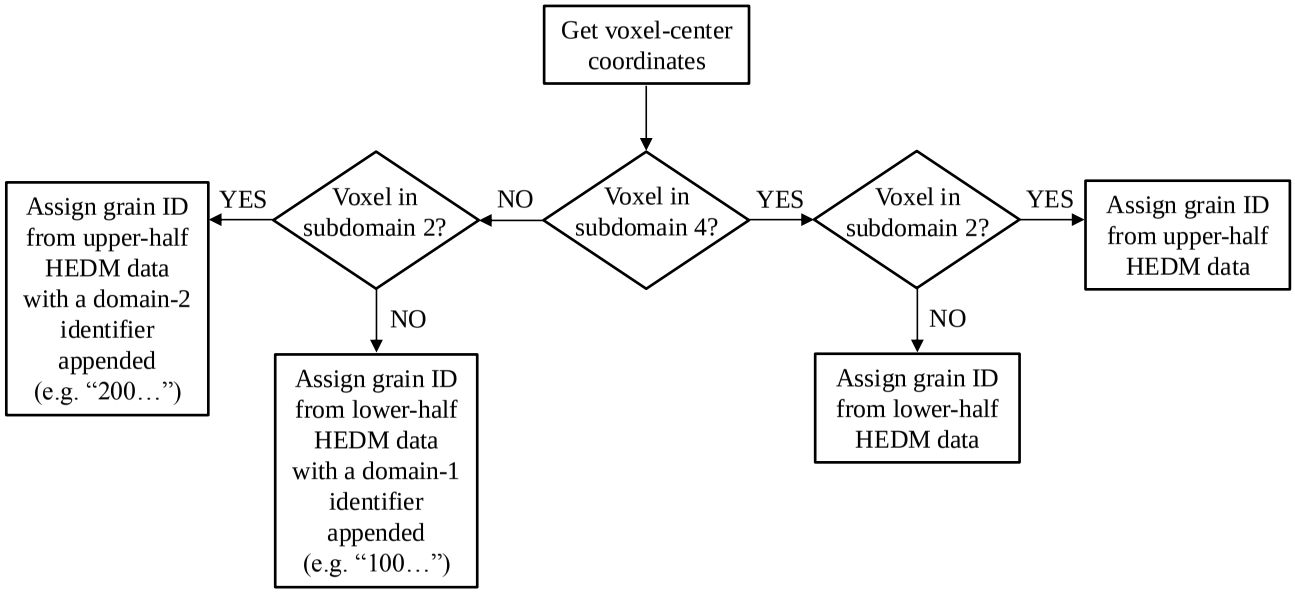

Figure 4.5: Algorithm to implicitly represent a history-dependent MSFC in a fully populated volume of voxels based on grain IDs from the HEDM data sets and on each voxel location relative to the four subdomains shown in Fig. 4.4.

by grain IDs: those that exist in the uncracked region are blue and those that exist above and below the cracked region are red and yellow, respectively. The voxelized volume is shown in the lower image with inverse pole figure coloring. Note that the modified grain IDs corresponding to subdomains $3 \cap 1$ and $3 \cap 2$ (e.g. grain IDs '100...' and '200...') maintain their original grain orientations, as indicated by the inverse pole figure map.

4.2.2 Multiscale Finite-element Mesh Generation

As described in Chapter 2, the geometry of the specimen shown in Fig. 2.3 exhibits out-of-plane displacement, even under a uniaxially applied load. Thus, one way to ensure that the appropriate boundary conditions are transferred to the grain-scale model is by using a multiscale modeling technique. In this work, concurrent multiscale modeling is employed, whereby a volume mesh of the grain-scale model is directly embedded within a volume mesh of the macroscale model.

For a given instantiation of the measured MSFC at a particular cycle count, an FE mesh is generated at the grain-scale using the voxelized reconstruction described in subsection 4.2.1. The software DREAM.3D (http://dream3d.bluequartz.net/) is used to create a surface mesh based on the voxelized data set. The surface mesh is formed between voxels having dissimilar grain IDs. Figure 4.7 shows a surface mesh generated for the merged volume shown in Fig. 4.2.

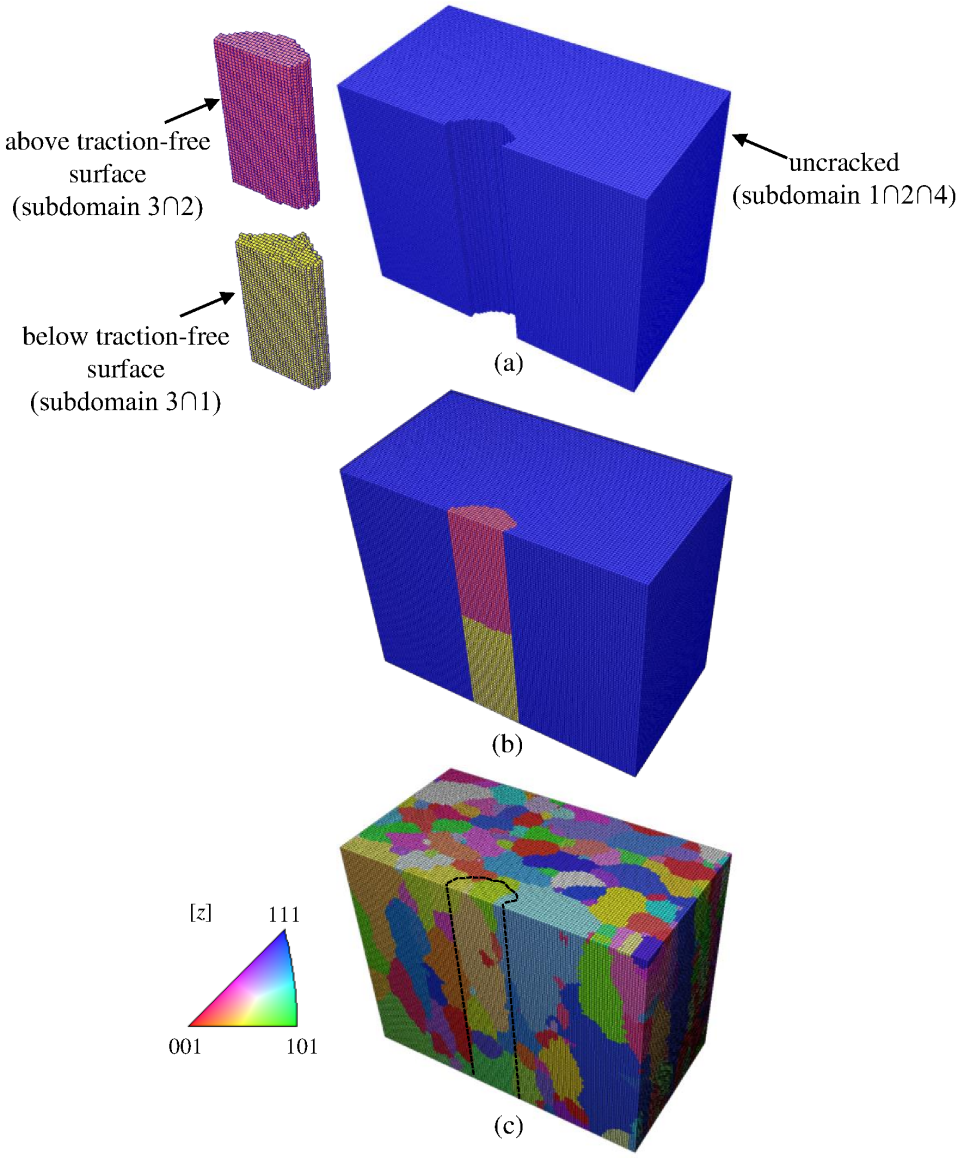

Figure 4.6: Digitally reconstructed voxelized volume for a particular history-dependent MSFC geometry. a-b) Colored by grain-ID subdomains: grain IDs without '100' or '200' appended (1∩2∩4); grain IDs with '200' appended (3∩2); grain IDs with '100' appended (3∩1). c) Inverse pole figure coloring relative to global loading direction, z; subdomain boundary outlined for reference.

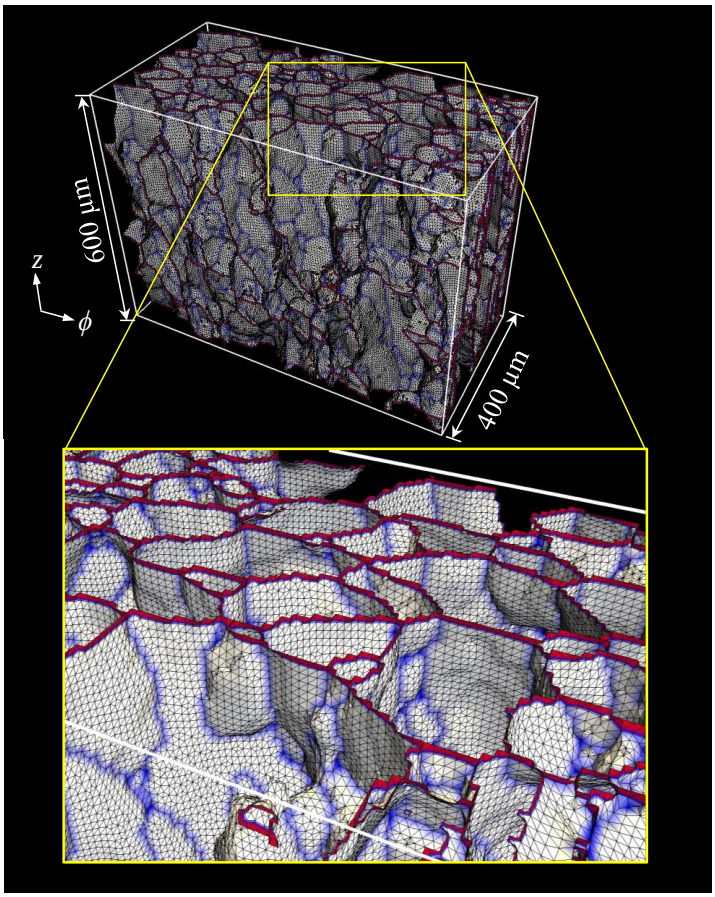

Figure 4.7: Grain-boundary surface mesh generated from voxelized data using DREAM.3D. Red elements intersect free surface of the volume and blue elements intersect other grain boundaries.

Because the algorithm described by Fig. 4.5 results in a distinct set of grain IDs for those voxels residing above and within the cracked region (subdomain 2∩3) and those residing below and within the cracked region (subdomain 1∩3), the meshing algorithm in DREAM.3D automatically forms a surface-mesh boundary at the interface of the two regions, i.e. along the MSFC surface. In this work, the Quick Surface Mesh option is used in DREAM.3D, which, by default, generates a surface mesh structured by the voxelized input data. A Laplacian smoothing option is used during surface meshing on the interior of the volume

to reduce the voxelation of the grain boundaries and the crack front while maintaining the element quality. The outer surfaces of the volume are selected to maintain a structured mesh, which facilitates mesh merging with the macroscale model. Finally, a meshing routine available in ABAQUS® is used to convert the surface mesh to a volume mesh.

After volume meshing, a Python script is executed that identifies nodes on the crack surface, i.e. along the boundary of the '100...' and '200...' grain IDs. The crack-surface nodes (excluding the crack-front nodes) are then duplicated, and the element connectivities are updated accordingly, effectively creating a traction-free surface. *The final result is a 3-D FE mesh that explicitly represents both the measured grain geometries as well as the measured MSFC geometry at a particular instance during the MSFC history.*

An FE model of the macroscale fatigue specimen (excluding the region that contains the grain-scale model) is created using ABAQUS®The mesh at the interior boundary that is to interface with the grain-scale model is "seeded" with the same resolution and structure as the outer mesh boundary of the grain-scale model. Doing so enables the mesh interface between the two models to align and merge, thereby creating one continuous mesh and obviating the need to enforce any constraints at the boundary. Figure 4.8 shows a typical concurrent multiscale FE mesh.

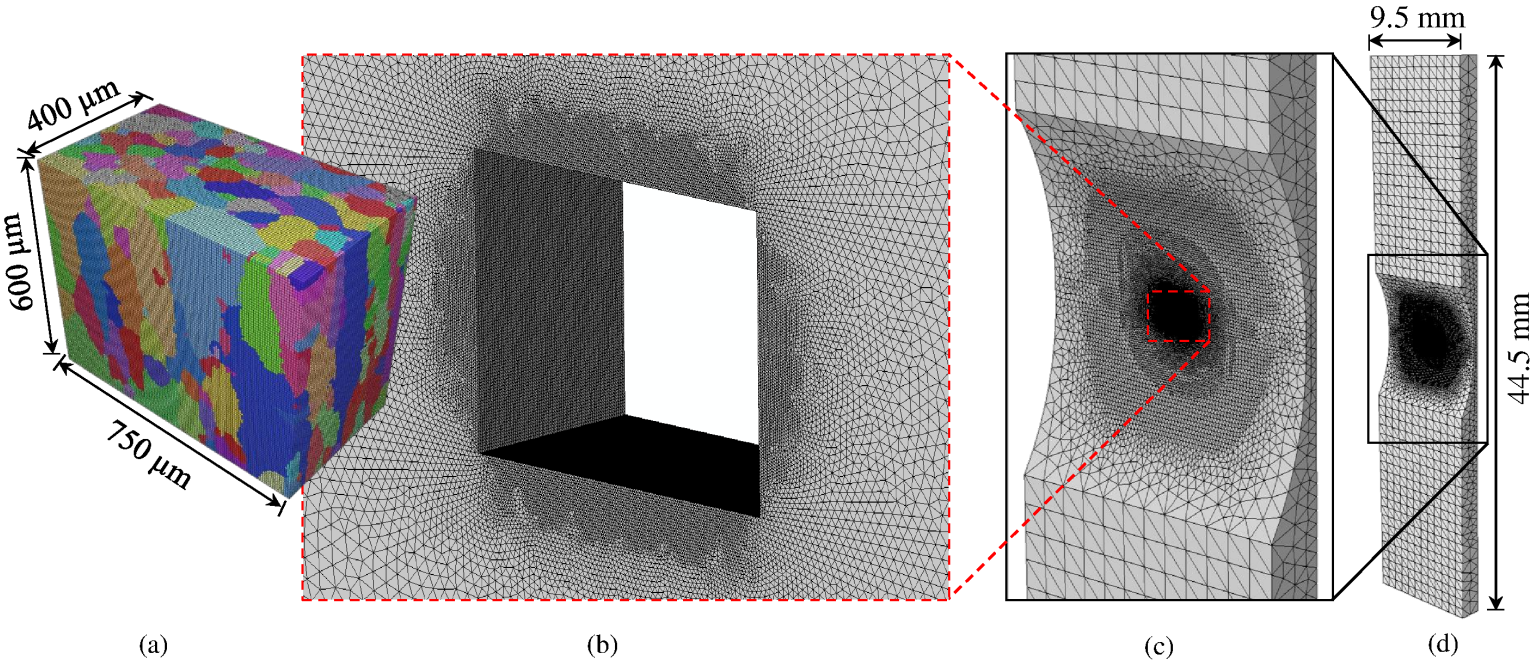

Figure 4.8: FE mesh: a) polycrystalline region, b) macroscale region, c-d) concurrent multiscale model.

4.2.3 Material Model Descriptions

The engineering stress-strain response for the Al-Mg-Si alloy is depicted in Fig. 4.9. The curve is approximated based on data collected in Chapter 2 for the same alloy, where the average grain diameter was 22 μm. The specimen modeled in the current study has an average grain diameter of approximately 110 μm and, thus, is expected to have a lower material yield strength according to the well-known Hall-Petch relationship [178, 179], which can be expressed as:

$$\sigma_y = \sigma_o + k_y d^{-1/2}, \tag{4.1}$$

where σ_y is the yield strength, d is the grain diameter, and σ_o and k_f are Hall-Petch constants that describe the resistance to flow and grain-boundary strengthening, respectively. For a constant value of σ_o, equation 4.1 can be used to express the yield strength of the larger-grained material, σ_{y2}, as:

$$\sigma_{y2} = \sigma_{y1} - k_y(d_1^{-1/2} - d_2^{-1/2}), \tag{4.2}$$

where the subscripts *1* and *2* denote the smaller-grained and larger-grained material, respectively. A value of 0.7 $\mathrm{MN/m^{3/2}}$ is used for the constant, k_y, following work by Evensen et al. [180] for the same alloy and solution-heat treatment as the material used here. For the grain sizes given above, the yield strength of the smaller-grained material from Chapter 2, and the value of k_y from [180], equation 4.2 predicts a yield strength of 182.5 MPa for the larger-grained Al-Mg-Si alloy modeled in the current study. Compared to the measured stress-strain curve for the smaller-grained material in Chapter 2, the curve shown in Fig. 4.9 has the same elastic response but with a flow stress that is simply reduced to reflect the lower yield strength.

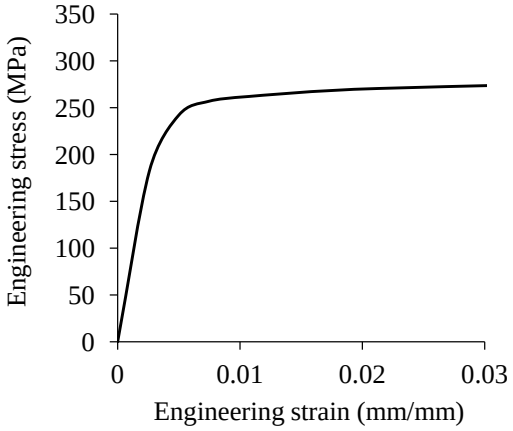

Figure 4.9: Engineering stress-strain response based on measured data from Chapter 2, updated using a Hall-Petch relationship.

Two material models are used to represent the material behavior in the multi-scale FE simulations. The material in the homogeneous, macroscale region is modeled using von Mises plasticity with linear hardening such that the material response shown in Fig. 4.9 is approximately reproduced. The grain-scale region is modeled using a crystal elasto-viscoplastic model implemented in an FE framework as described in [181]. The framework is capable of predicting inhomogeneous deformation and stress fields that arise at the mesoscale as a result of interactions among discrete grains of different crystallographic orientations. The numerical implementation of the constitutive model is described in detail elsewhere [181, 182]; however, a high-level description of relevant details is provided next.

In the grain-scale constitutive model, plastic deformation is manifested by the

evolution of slip on twelve octahedral slip systems ({111} <110>) for face-centered cubic materials. The kinematic description follows Peirce et al. [183] and proceeds from a multiplicative decomposition of the deformation gradient into elastic and plastic parts, where the elastic part accounts for elastic stretching and rotation of the crystal lattice, and the plastic part accounts for the evolution of crystallographic slip.

The slip rate for a given slip system follows a simple power law:

$$\dot{\gamma}^{\alpha} = \dot{\gamma}_0 \frac{\tau^{\alpha}}{g^{\alpha}} \left| \frac{\tau^{\alpha}}{g^{\alpha}} \right|^{\frac{1}{m}-1}, \tag{4.3}$$

where $\dot{\gamma}_0$ is a reference rate of slip, τ^{α} is the resolved shear stress on slip system α, g^{α} is the hardness (resistance to slip) on slip system α, and m is a rate-sensitivity parameter. In the current simulations, a Voce-Kocks type of hardening evolution is specified [184, 185], which assumes an equivalent effect of latent and self hardening (i.e. that all slip systems have an equivalent initial hardness and harden at the same rate). The hardness evolution can thusly be expressed as:

$$\dot{g} = G_0 \left(\frac{g_s - g}{g_s - g_0} \right) \dot{\gamma}, \tag{4.4}$$

where G_0 is a hardening-rate parameter, g_0 is the initial hardness, and $\dot{\gamma}$ is the total slip rate summed over all slip systems.

The procedure for calibrating the material parameters involved in the crystal-plasticity model is described in [8] and in section C.0.6 of the Appendix. The procedure involves using an optimization algorithm (viz. a genetic algorithm) that seeks to minimize error between the simulated and experimental stress-strain response of the polycrystalline aggregate. Table 4.1 provides the parameter values that have been calibrated for the current study.

Table 4.1: Calibrated crystal-plasticity parameters and Lamé constants.

$\dot{\gamma}_0$ (s^{-1})	m	G_0 (MPa)	g_0 (MPa)	λ (MPa)	μ (MPa)
0.05	0.0049	150.0	95.5	50775.0	24800.0

4.2.4 MSFC Simulations

Three MSFC instantiations are modeled that correspond to the MSFC geometry measured in Chapter 3 at 180,000; 190,000; and 200,000 loading cycles. The sequence of crack shapes is shown in Fig. 4.10. An element size of 6 μm is used for the grain-scale FE mesh, which is determined to be adequate based on results from a mesh refinement study described in section C.0.7 of the Appendix. The entire multiscale model is meshed using quadratic tetrahedral elements. The grain-scale and macroscale mesh for each of the models comprises approximately 42.1 million degrees of freedom (10.5 million elements) and 7.5 million degrees of freedom (1.8 million elements), respectively.

Boundary conditions are applied to emulate the experimental conditions from Chapter 3. The grip ends (i.e. outside of the notched region) are constrained from motion in the ρ and ϕ directions. Additionally, one of the grip ends is constrained in the z direction while the other is loaded uniaxially in tension.

For comparison, each of the three concurrent multiscale models is loaded monotonically[2] to a macroscopic notch-surface strain just beyond the elastic limit (ap-

[2]Future simulations will involve cyclic loading.

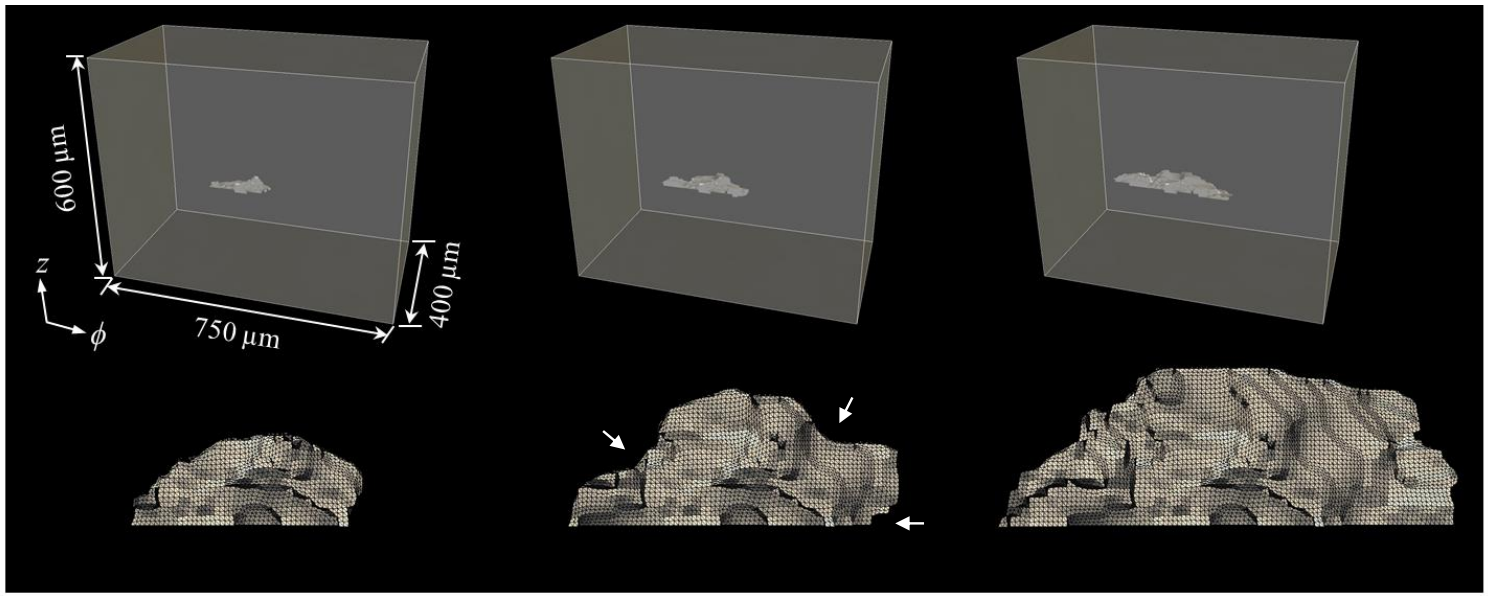

(a) (b) (c)

Figure 4.10: Explicitly represented sequence of crack shapes modeled in the current work. 3-D crack shapes were measured in Chapter 3 and correspond to the following load cycles: a) 180,000; b) 190,000; c) 200,000. White arrows in (b) indicate regions of pinning, which locally accelerate during subsequent propagation.

proximately 0.35%). Each simulation is performed using an in-house parallel FE solver on 1024 processor cores and requires approximately 36 wall-clock hours to reach peak-applied load. Results from the simulations are provided next.

4.3 Results and Discussion

An example of results from one of the concurrent multiscale simulations is provided in Fig. 4.11, in which the color contours correspond to the stress component in the loading direction. It is evident from Fig. 4.11 that the through-thickness gradient along the boundary of the grain-scale region is non-negligible, thus motivating and justifying the use of concurrent multiscale modeling in the current work. As expected, the von Mises material model predicts a continuous stress field over the macroscale specimen; whereas, the crystal-plasticity model predicts a non-continuous stress field that arises due to inhomogeneity at the polycrystalline scale. As shown, the grains in the polycrystalline region experience a wide range of stress values, both well above and well below the surrounding macroscopic stress.

The polycrystalline region is examined in greater detail in Figs. 4.12-4.16. Figure 4.12 again depicts the stress component in the global loading direction, this time for each of the three successive MSFC instantiations from Fig. 4.10. The top row of images shows the polycrystalline volume with the trace of the crack highlighted in white. The bottom row of images omits the regions above and below the traction-free surfaces to expose the fields on the interior of the volume just ahead of the crack front. Points along the crack front are shown in black. A similar set of images is provided in Fig. 4.13 for a slip-based metric defined in

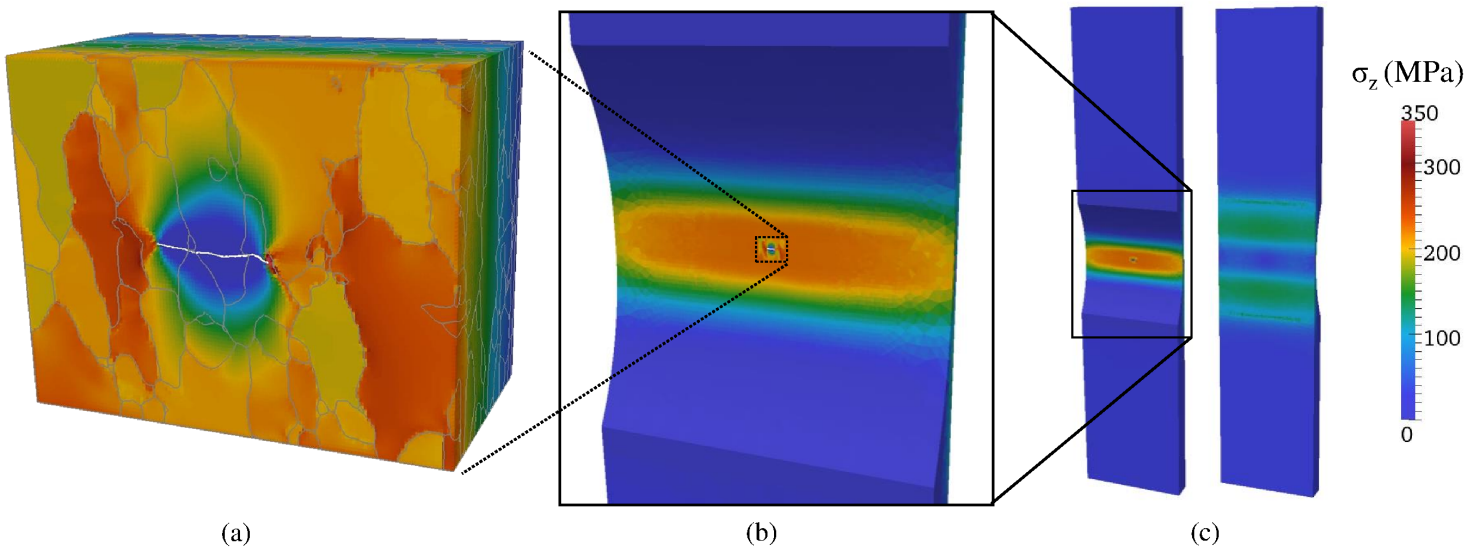

Figure 4.11: Stress component in the global loading direction for multi-scale model with measured MSFC instance from Fig. 4.10(b). a) Non-continuous response predicted at the grain scale using crystal-plasticity model. b) Continuous response predicted at the macroscale using von Mises plasticity model. c) Stress fields on the notched and flat sides of the specimen.

[170]. Following the notation in [170], the metric, D_3, is the total accumulated slip summed over all of the slip systems as follows:

$$D_3 = \sum_{\alpha=0}^{N_s} \Gamma^\alpha, \tag{4.5}$$

where Γ^α is the accumulated slip on slip system α, computed as

$$\Gamma^\alpha = \int_0^t |\dot{\gamma}^\alpha| \, dt. \tag{4.6}$$

As shown in the top rows of Fig. 4.12 and Fig. 4.13, the trace of the measured MSFC on the free surface suggests that the MSFC propagated relatively normal to the global loading direction for the sequence of growth depicted. However, by examining together the shape of each crack instance shown in Fig. 4.10, the interior fields ahead of each crack front shown in the bottom row of Figs. 4.12 and 4.13, and the variability in crack-growth rates shown in Fig. 3.6, it is clear that in 3D the MSFC evolved in a more complex manner. As magnified in Fig. 4.14, the computed fields are quite non-uniform in the neighborhood of and along each crack front. For example, for the first MSFC instantiation, the computed stresses on the free surface just ahead of the crack front shown in Fig. 4.14(a) are much higher near the right crack tip than the left; qualitatively, this region of increased stress (at least for the stress component shown) does not exhibit a marked increase in MSFC-growth rate during the subsequent interval of crack growth.

Figures 4.14(b) and 4.14(e) depict computed fields for the crack geometry shown in Fig. 4.10(b). Note from Fig. 4.10(b) that the crack front experiences three regions of pinning (two along the interior of the volume and one on the free surface), which can also be observed by looking at the marker band corresponding

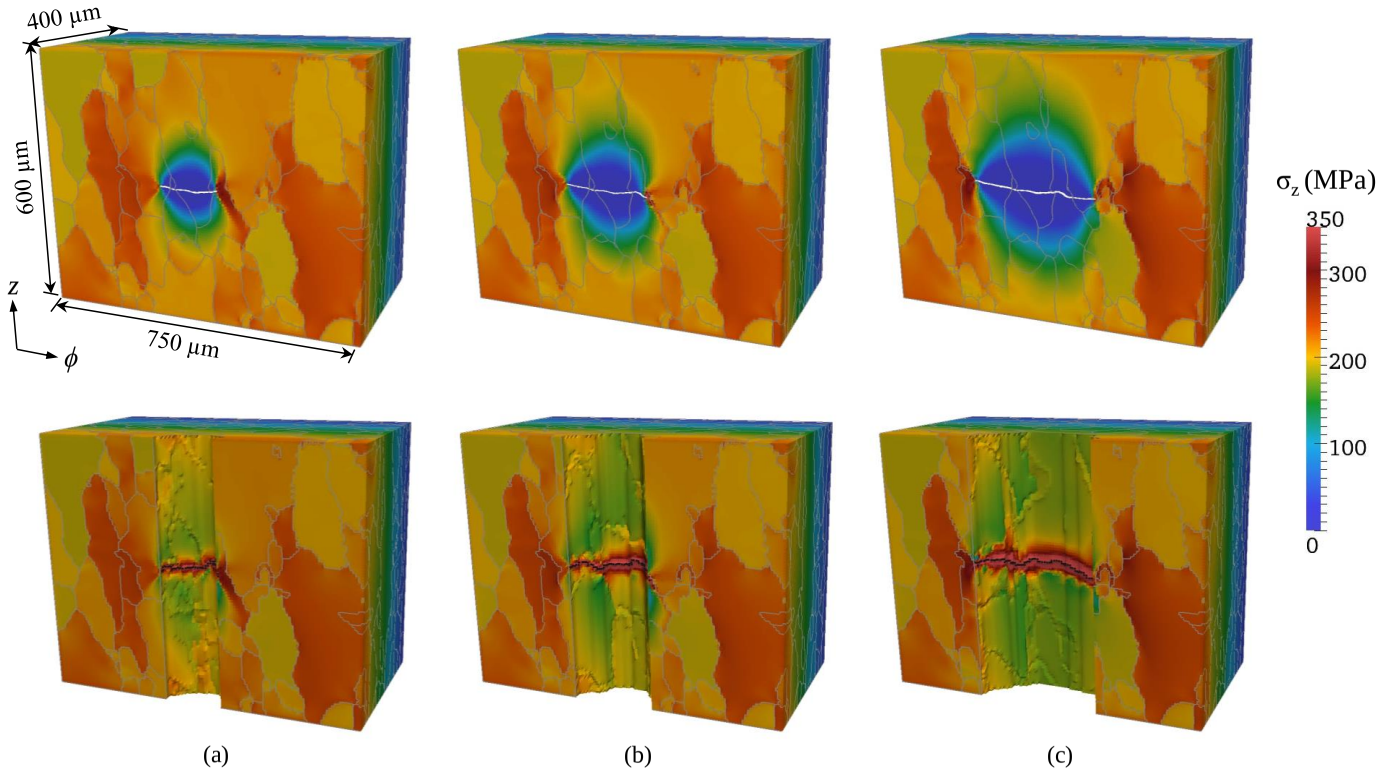

Figure 4.12: Stress component in global loading direction for polycrystalline volume with MSFC shapes corresponding to Fig. 4.10 a-c. Top row depicts full volume with crack trace shown in white on free surface. Bottom row shows interior view with fields just ahead of the embedded crack front (crack-front points are shown in black).

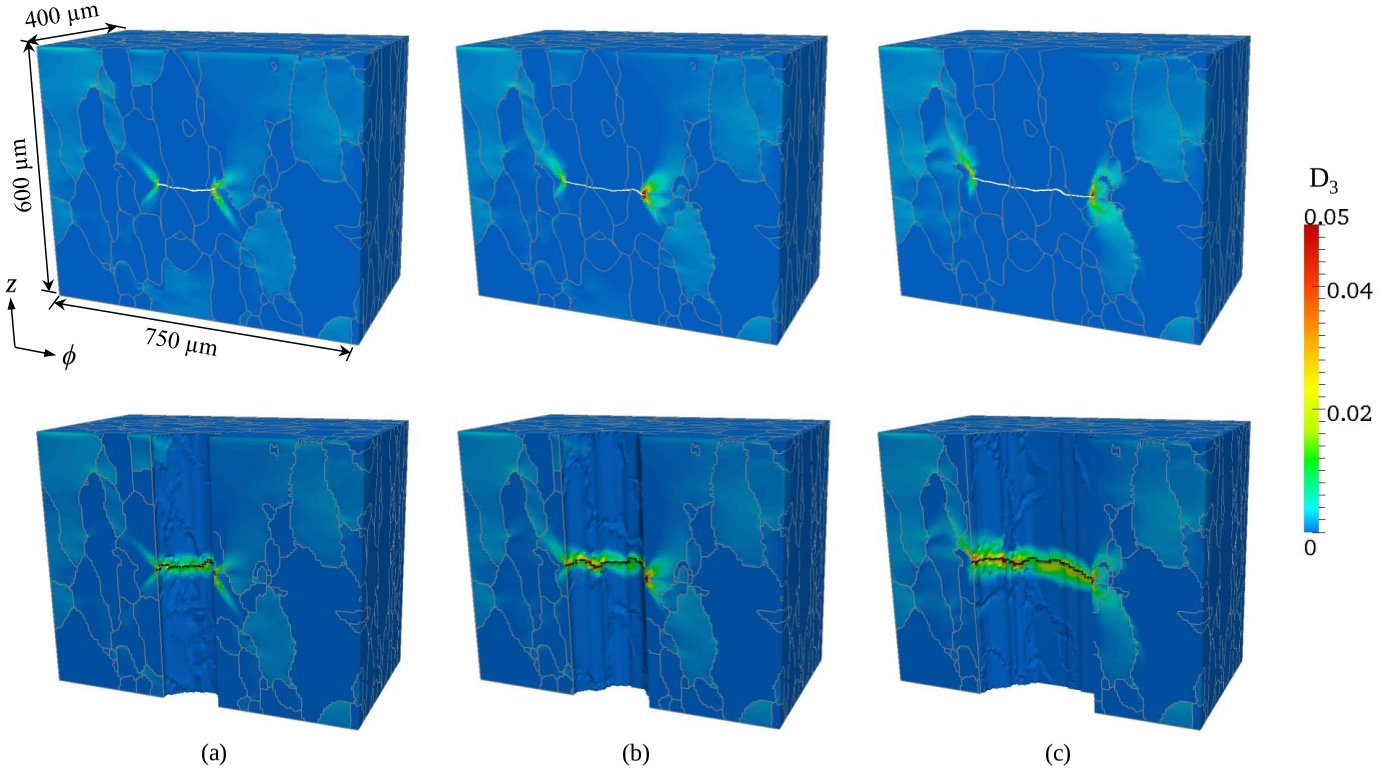

Figure 4.13: D_3 metric for polycrystalline volume with MSFC shapes corresponding to Fig. 4.10 a-c. Top row depicts full volume with crack trace shown in white on free surface. Bottom row shows an interior view with fields just ahead of the embedded crack front (crack-front points are shown in black).

to 190,000 load cycles shown in Fig. 3.6. The pinned regions exhibit local acceleration during subsequent crack propagation, which can be deduced from the successive crack shape shown in Fig. 4.10(c) and from the MSFC propagation-rate map provided in Fig. 3.6. As shown in Fig. 4.14(e), a concentration in the metric D_3 is computed near each of the pinned regions, especially so for the pinned regions on the left (interior) and right (free surface).

To further visualize the fields ahead of the two, interior, pinned regions from the second MSFC instantiation (Fig. 4.10(b)), the results from Figs. 4.12(b) and 4.13(b) are clipped on two planes that intersect the approximate locations of pinning along the crack front. The locations of the two clip planes are shown in Fig. 4.15. The clipped results are presented in Fig. 4.16. Along with the computed fields, the trace of the measured crack surface is depicted in white for reference; the trace represents the subsequent path that the MSFC took within each clip plane as it continued propagating through the remaining ligament of the specimen.

Several interesting features along the subsequent crack trace are called out in Fig. 4.16 for discussion. First, within the entire region labeled 'a' on the left clip plane, the MSFC propagated along or very near to multiple grain boundaries (i.e. within 6 μm, which corresponds to the resolution of both the near-field HEDM measurements in the z direction and the FE mesh refinement level). Interestingly, as the MSFC propagated from the crack-front position modeled in Fig. 4.16 toward the encircled region 'a', the trace of the MSFC in the cutting plane inclined approximately 48° intragranularly. Based on the crack-surface crystallography measured in Chapter 3, the majority of this inclination followed

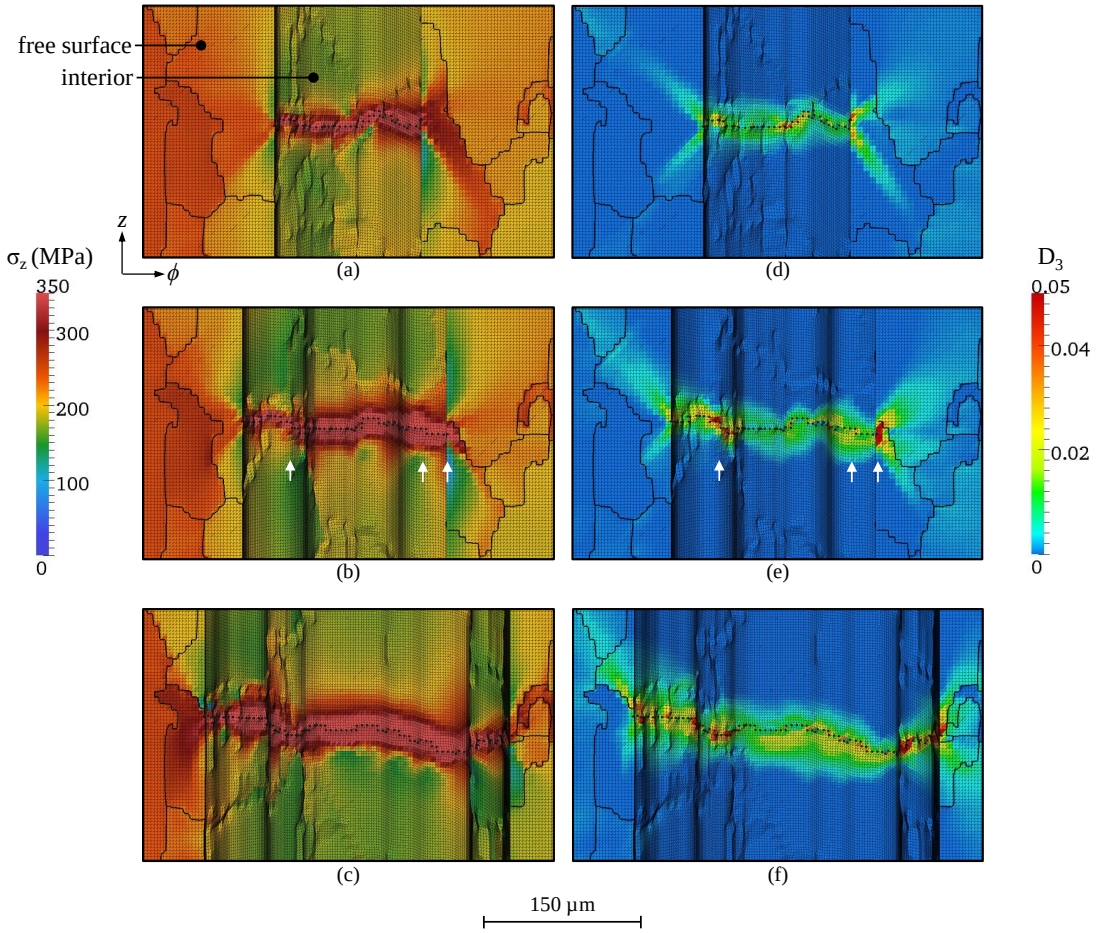

Figure 4.14: Magnified views of MSFC sequence from bottom row of Figs. 4.12 and 4.13 shown under high magnification with FE mesh visible and grain-boundary traces outlined on the free surface. a,d) MSFC shape corresponding to 180,000 load cycles. b,e) MSFC shape corresponding to 190,000 load cycles. c,f) MSFC shape corresponding to 200,000 load cycles. White arrows in (b) and (e) point to approximate locations where crack front is currently pinned and locally accelerates during subsequent propagation (see also Fig. 4.10(b)).

along a near-{001} crystallographic plane. In the clip plane on the right, the meandering crack path displayed within the encircled region labeled 'b' occurred

entirely within one grain and, based on results from Chapter 3, occurred along a wide range of crystallographic planes, including near-{001}, near-{101}, and high-index planes. Finally, the encircled region 'c' highlights crack propagation along a grain boundary whose trace in the cutting plane is nearly perpendicular (within 10 °) to the global loading direction. As mentioned earlier, strictly analyzing results from trace observations is not sufficient to fully characterize crack evolution and its relationship to computed fields. These results, however, are meant to provide the reader with a snapshot of MSFC behavior and computed fields on the interior of the volume ahead of the crack front at a particular instance during the load history.

The above discussion is limited to qualitative observations made from a subset of quantitative fields that have been computed using 3-D numerical simulation. The results depict the complexity of MSFC propagation in 3D as well as the amount of information obtained from simulating the observed MSFC behavior. It has become evident to the author from this study that while there is now a demonstrated method for characterizing, digitally reconstructing, and numerically simulating observed MSFC evolution in 3D, there remains a great need for systematic, comprehensive, and efficient approaches to post-process and analyze the abundant results obtained from such 3-D MSFC simulations, perhaps using learning algorithms not unlike the artificial neural network developed in Chapter 1. Doing so will allow future focus to be placed on discovery of quantitative physical and mechanical relationships that underpin complex 3-D MSFC evolution. Nevertheless, the work presented here represents, to the author's knowledge, state-of-the-art simulation results that have been made possible through state-of-the-art characterization performed in Chapter 3.

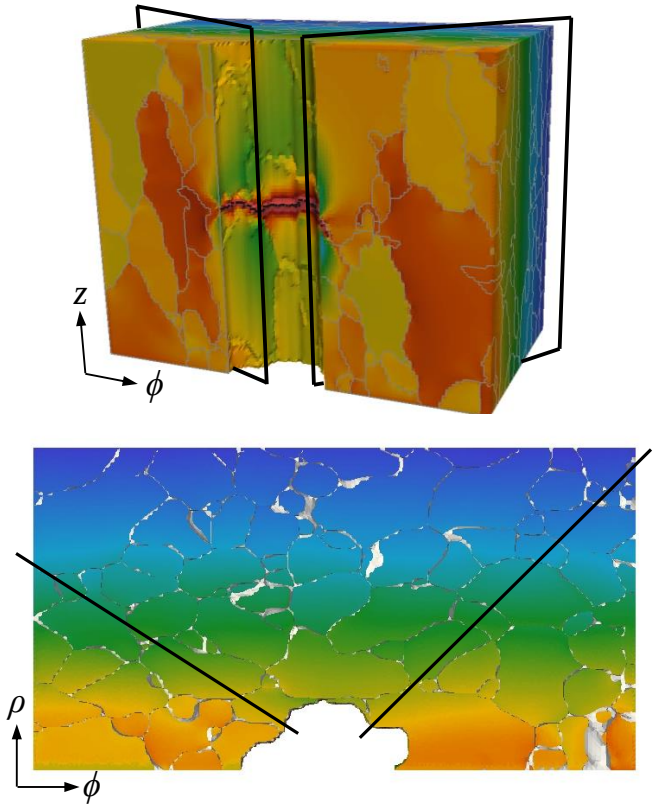

Figure 4.15: Location of clip planes used to visualize interior fields ahead of the approximate locations of pinning called out in Fig. 4.14(b).

4.4 Conclusions

Chapter 3 presented an experimental method to characterize and quantify 3-D rates of MSFC propagation and high-resolution crack-surface crystallography for a naturally nucleated MSFC in an Al-Mg-Si alloy using post-mortem, synchrotron-based measurements. The work described here seeks to reproduce the observed 3-D MSFC behavior from Chapter 3 by using concurrent multi-scale numerical simulations that explicitly represent both the measured MSFC geometry and the measured grain geometries and crystallographic orientations.

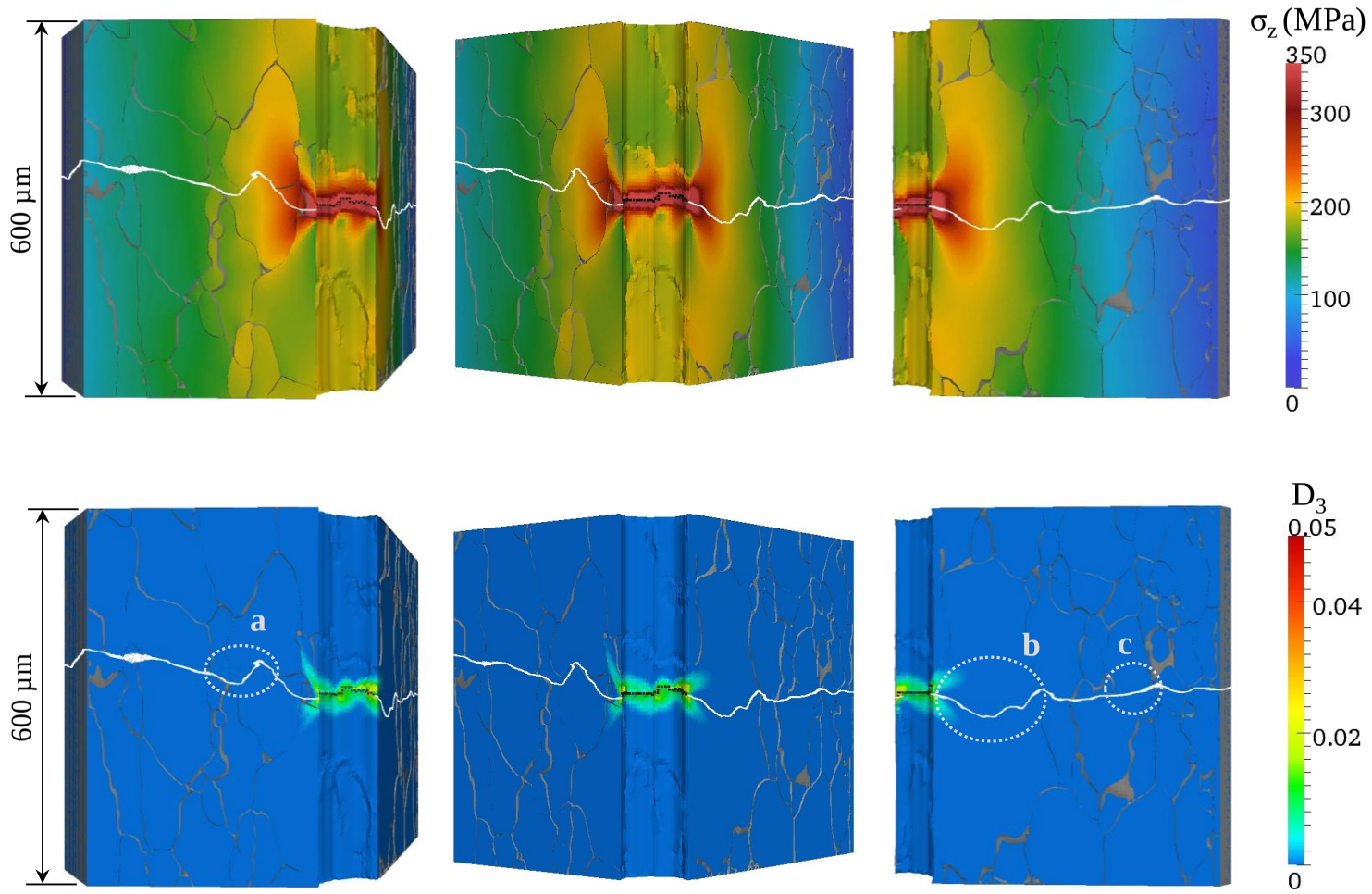

Figure 4.16: Results from Figs. 4.12(b) and 4.13(b) clipped along the planes shown in Fig. 4.15 to visualize fields ahead of the approximate interior pinned locations called out in Fig. 4.14. The trace of the subsequent crack path is overlaid in white for reference.

The following is a succinct summary of the work presented here:

- Geometrically explicit FE models of multiple MSFC instantiations at the grain-scale are generated from voxelized descriptions of the volume. For the MSFC at a particular instance during the load history, the voxelized volume implicitly represents the MSFC geometry by the assignment of grain IDs to each voxel based on that voxel's location relative to the MSFC.
- A concurrent multicale model is constructed by embedding the geometrically explicit, grain-scale model into a 3-D FE model of the macroscale specimen. The models are merged to create a continuous mesh across the interface of the two regions.
- A von Mises material model is used for the macroscale region, which predicts a homogeneous distribution of stress and deformation under an applied load. A crystal elasto-viscoplastic material model is used for the grain-scale region, which predicts inhomogeneous distributions of stress and deformation arising from the underlying grain geometries and orientations.
- Stress and slip-based metrics are computed using parallel FE simulations and are presented for a sequence of 3-D MSFC geometries measured in Chapter 3.

While the study represents the first time, to the author's knowledge, that a sequence of measured, 3-D, MSFC propagation has been digitally reproduced and numerically simulated at the scale of individual grains, there remains a great need for systematic, comprehensive, and efficient approaches to post-process and analyze quantitatively the abundant results obtained from 3-D MSFC simulations like those presented here.

APPENDIX A

APPENDIX FOR CHAPTER 2

Alcoa fabricated several ISPs as part of its test program in 1998. The purpose of the test program was to compare fatigue crack growth and residual strength among ISPs machined from either of two, lower wing skin, aluminum alloys—AA 2024-T351 or C433-T39. Test information has been utilized by others for analysis purposes [22, 68, 70]. Alcoa has provided the author with test details, which are provided here for completeness.

Fatigue crack growth and residual strength tests were conducted at Alcoa for four ISPs, two machined from AA 2024-T351 and two machined from C433-T39. Dimensions of all panels are shown in Fig. 1.16. In each panel, an initial two-bay saw cut of length $2a_{saw} \approx 2.54$ cm was made at mid-height to completely sever the middle stiffener. The initial cut was then pre-cracked to length $2a_0 \approx 5.08$ cm by applying uniaxial cyclic load in the y-direction, where $P_{min} = 31$ kN and $P_{max} = 311$ kN. Subsequently, a modified transport wing standard (TWIST) loading spectrum [186], shown in Table A.1, was applied in the y-direction to propagate the fatigue crack. The applied spectrum had a mean flight stress of $S_{mf} = 68.9$ MPa, truncated to level V, and included a ground-air-ground (GAG) cycle with a reduced ground level stress of $S_{ground} = -34.5$ MPa. Taxi loads were neglected. Depending on the panel, the fatigue crack was propagated until both crack fronts were 2.54 cm short of reaching the intact stiffeners ($2a_i \approx 24.1$ cm) or until both crack fronts just entered the intact stiffeners ($2a_i \approx 30.0$ cm). Subsequently, each panel was loaded monotonically in uniaxial tension until failure occurred by unstable crack growth. A test matrix of the four panels and corresponding residual strengths is shown in Table A.1. The ISP simulated in this

work follows panels 5 and 5A.

Figure A.1: Standard TWIST spectrum scaled to mean flight stress S_{mf} = 68.9 MPa with variable amplitude loads S_a (left). Modified spectrum (right) applied uniaxially to the Alcoa ISP prior to residual strength testing. Courtesy Alcoa.

Standard TWIST profile scaled to S_{mf} = 68.9 Mpa

Block Level	Load Level (S_{mf} ± S_a), MPa	Number of cycles per 4000 flights
I	68.9 ± 110.3	1
II	68.9 ± 103.4	2
III	68.9 ± 89.6	5
IV	68.9 ± 79.3	18
V	68.9 ± 68.6	52
VI	68.9 ± 57.9	152
VII	68.9 ± 47.2	800
VIII	68.9 ± 36.5	4170
IX	68.9 ± 25.9	34800
X	68.9 ± 15.3	358665
GAG	-34.5 (last peak per flight)	4000

Modified TWIST profile applied to ISPs

Block Level	Load Level (S_{mf} ± S_a), MPa	Number of cycles per 4000 flights
I	--	truncate loads to level V
II	--	
III	--	
IV	--	
V	68.9 ± 68.6	78
VI	68.9 ± 57.9	152
VII	68.9 ± 47.2	800
VIII	68.9 ± 36.5	4170
IX	68.9 ± 25.9	34800
X	68.9 ± 15.3	358665
GAG	-34.5 (last peak per flight)	4000

Table A.1: Description of all ISPs and corresponding residual strengths from Alcoa test program. Courtesy Alcoa.

Panel ID	Material	Crack length, $2a_i$, just prior to residual strength test (cm)	Residual strength (kN)
3	2024-T351	24.1 cm	1225
4	2024-T352	30.0 cm	1015
5A	C433-T39	24.1 cm	1660
5	C433-T39	24.1 cm	1385
6	C433-T40	30.0 cm	1295

APPENDIX B

APPENDIX FOR CHAPTER 3

B.0.1 Wire EDM Photographs

Wire electrical discharge machining (EDM) was performed at NASA Langley Research Center by Mr. Johnnie West. Photographs of the machining process are provided in Fig. B.1.

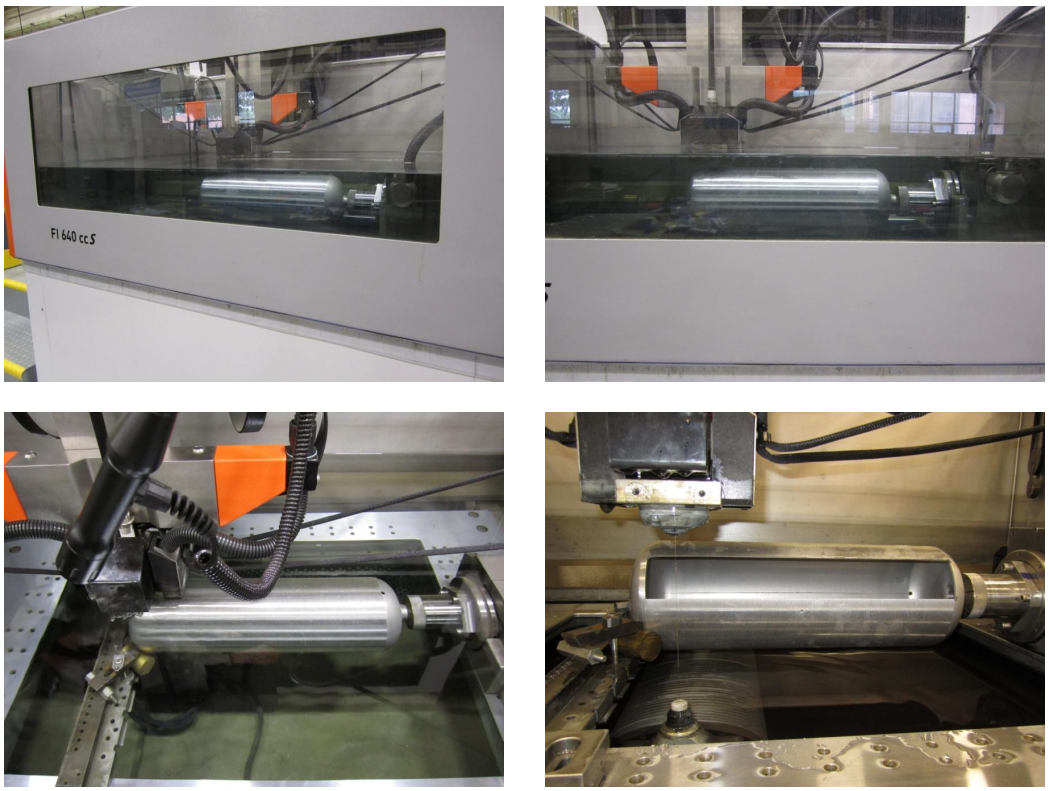

Figure B.1: Material removal from COPV liner using wire EDM.

B.0.2 Electro-chemical Surface Treatments

Chemical milling and electropolishing were performed at NASA Langley Research Center by Mr. Dave Hartman with assistance from the author. Photographs of each setup are provided in Fig. B.2. Figure B.3 shows specimens after the different surface treatments.

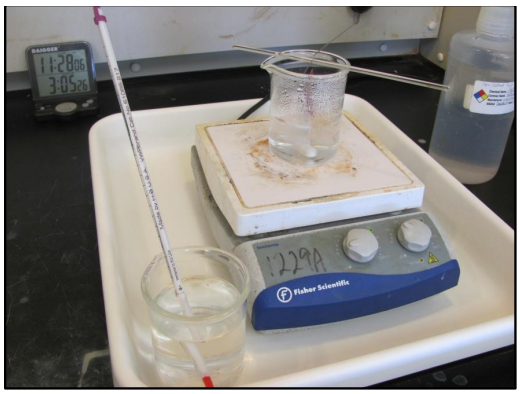

(a)

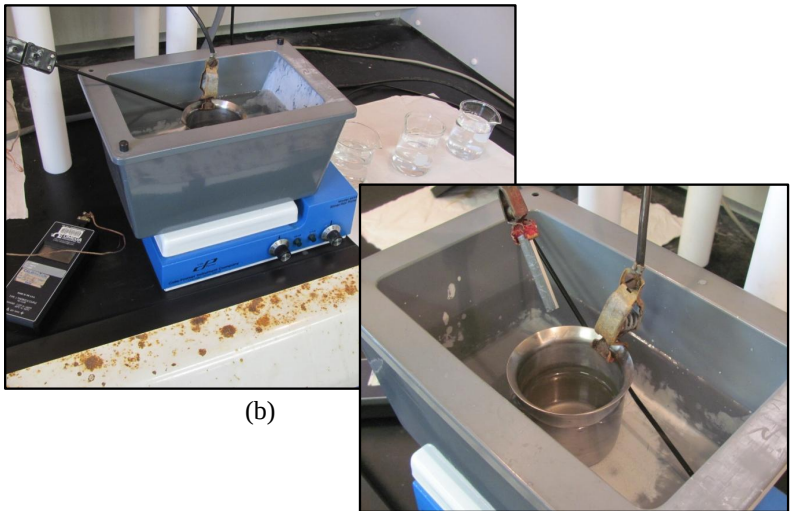

(b)

Figure B.2: a) Chemical-milling setup per specifications provided in [5]. b) Electropolishing setup per specifications provided in [5].

Figure B.3: Appearance of Al-Mg-Si specimens after various surface treatments. Left: after wire EDM and prior to any electro-chemical treatment. Middle: after chemical milling. Right: after electropolishing.

B.0.3 Mechanical Testing Details

Mechanical testing was performed at NASA Langley Research Center on a 22.5 kip hydraulic load frame with a 500 lbf load cell calibrated over the full range. A special fixture adapter with wedge grips was custom designed to mount the specimens in the load frame. The design specifications for the various fixture components issued by the author to the machine shop at NASA Langley Research Center are shown in Figs. B.4 through B.8. Renderings of the complete, fixture-adapter assembly are provided in Figs. B.9 and B.10.

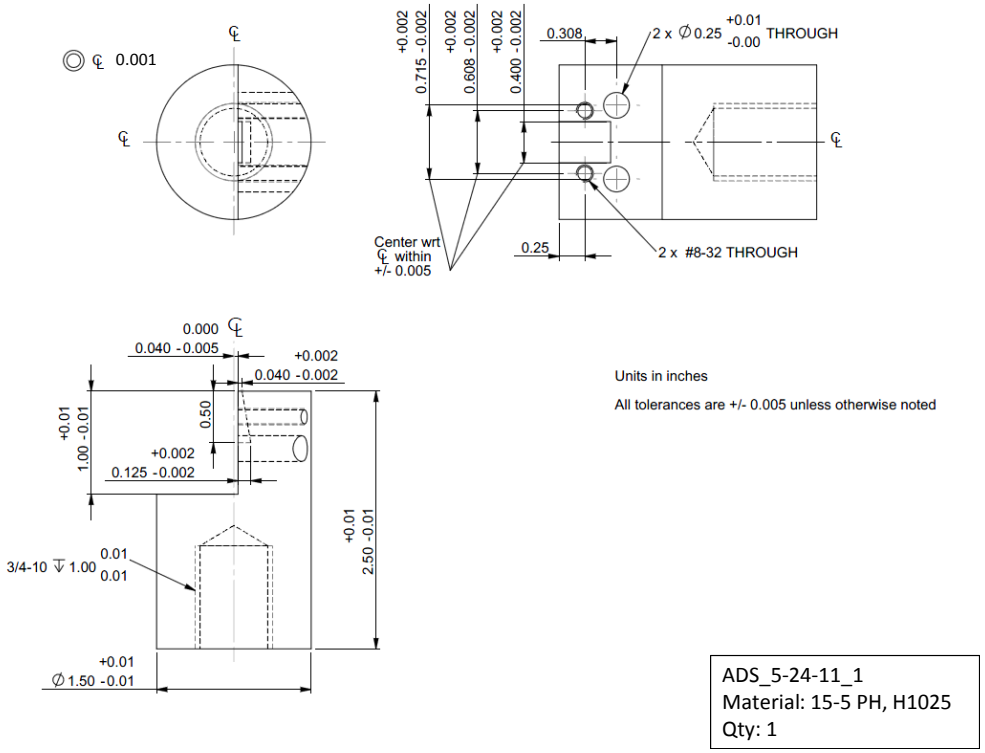

Figure B.4: Technical drawing of fixture-adapter component.

B.0.4 ASTM Tensile Tests

Standardized tensile tests of the COPV-liner material were performed at NASA Langley Research Center by Mr. Stewart Walker with assistance from Mr. William Johnston. Subscale dogbone specimens were machined from a portion of material that had been extracted from the COPV liner, as shown in Fig. B.11. Results provided by Mr. Walker are shown in Fig. B.12.

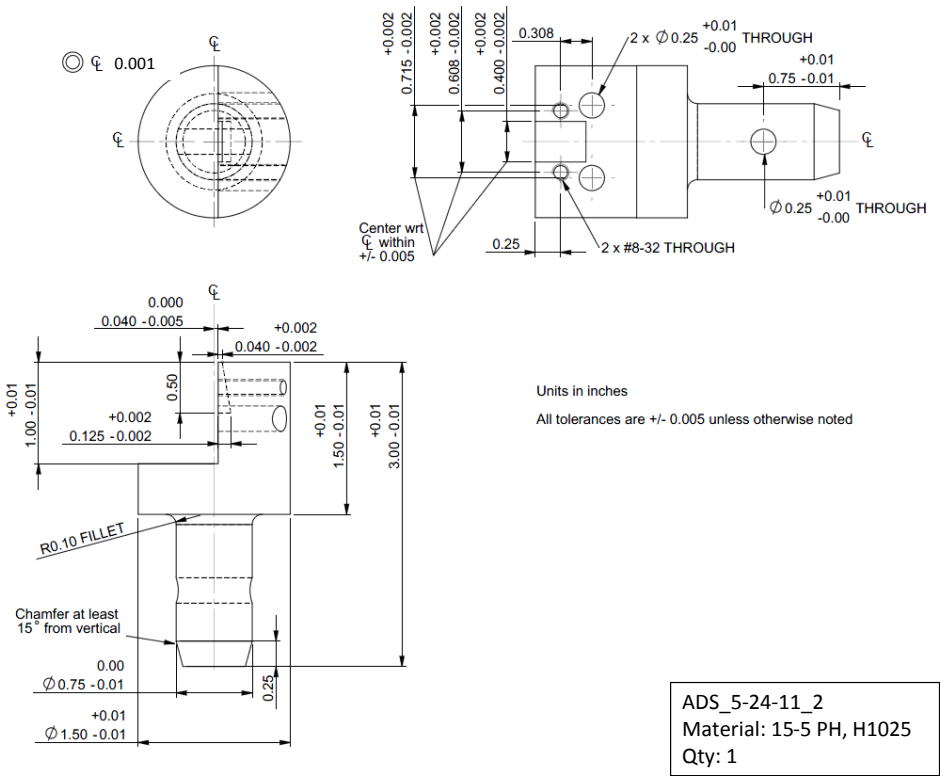

Figure B.5: Technical drawing of fixture-adapter component.

B.0.5 Digital Image Correlation Details

Initial results from the digital-image correlation data revealed a non-symmetric strain field across the notch, indicating that an initial set of test specimens had been loaded non-uniformly. From this study, it became apparent that the specimen sensitivity to boundary conditions is enhanced as the size of the specimen decreases (e.g. the specimens used in the current work, which were relatively thin compared to those typically tested in the load frame that was used, were much more sensitive to the sequence and increments of torque applied to tighten the screws in the screw-mounted wedge grips depicted in Figures B.9 and B.10). Because of this finding, the method for mounting and handling the

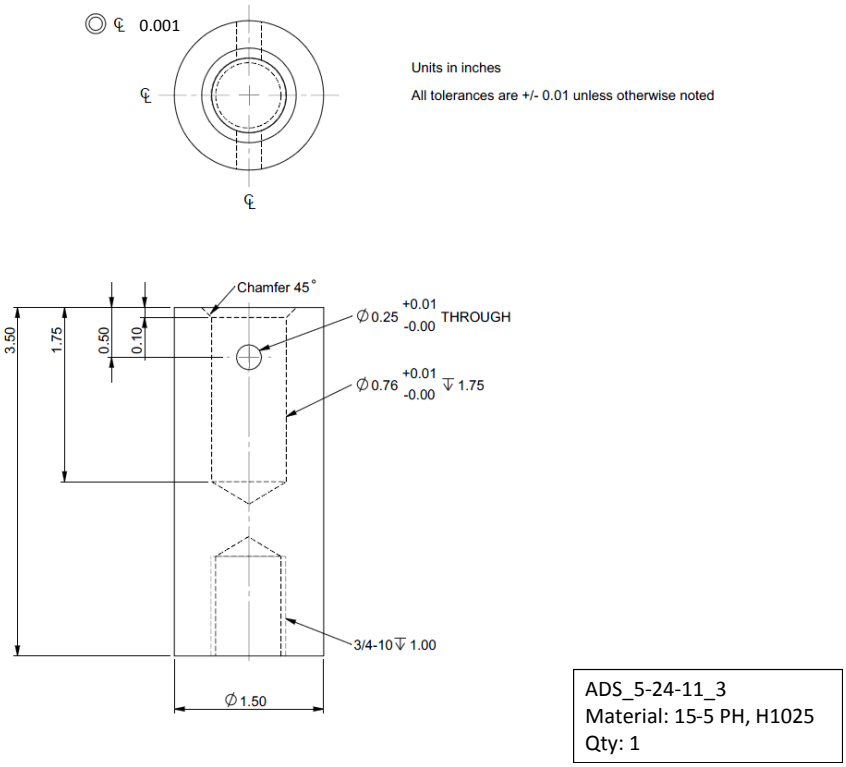

Figure B.6: Technical drawing of fixture-adapter component.

specimens in subsequent tests was modified appropriately.

Figure B.13 shows the camera and data-acquisition setup for digital image correlation with a specimen mounted in the hydraulic load frame. Figure B.14 shows a comparison between digital-image correlation results and results from an FE simulation of a specimen under the same applied load. As shown in the figure, a slightly bi-axial strain state arises as a result of out-of-plane displacement from the non-symmetric specimen geometry.

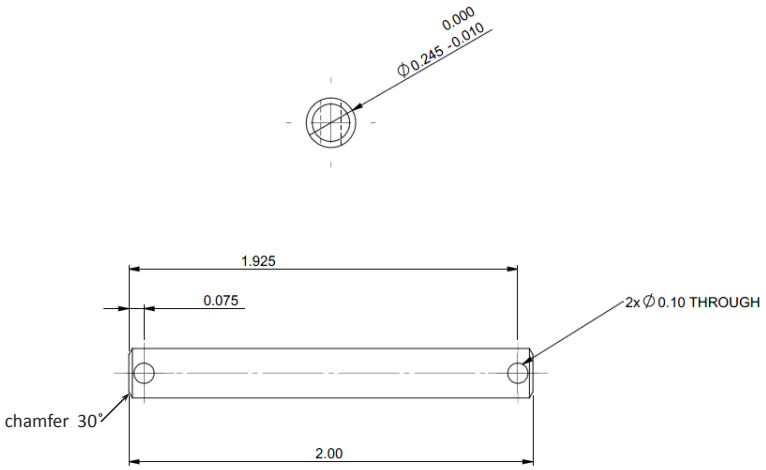

Units in inches

All tolerances are +/- 0.005 unless otherwise noted

ADS_5-24-11_4
Material: 15-5 PH, H1025
Qty: 2

Figure B.7: Technical drawing of fixture-adapter component.

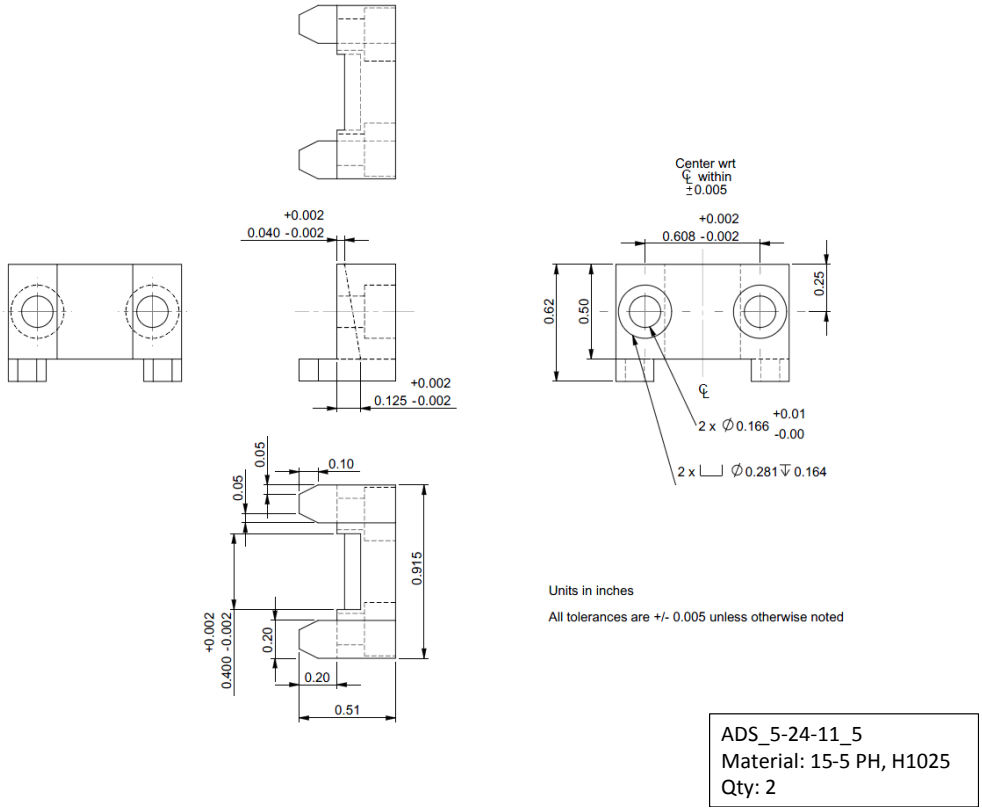

Figure B.8: Technical drawing of fixture-adapter component.

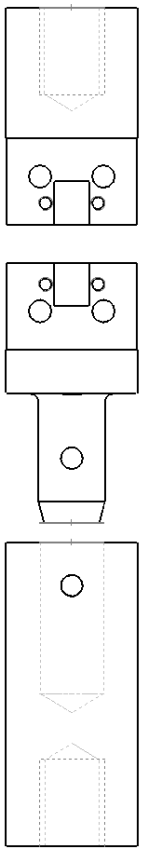

Figure B.9: Rendering of fixture-adapter assembly created using SolidWorks.

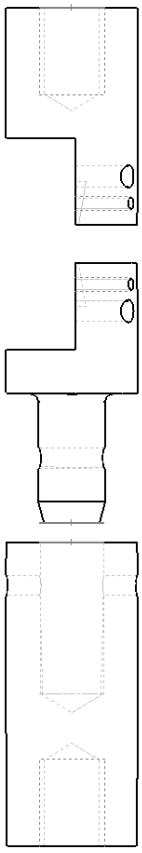

Figure B.10: Rendering of fixture-adapter assembly created using SolidWorks.

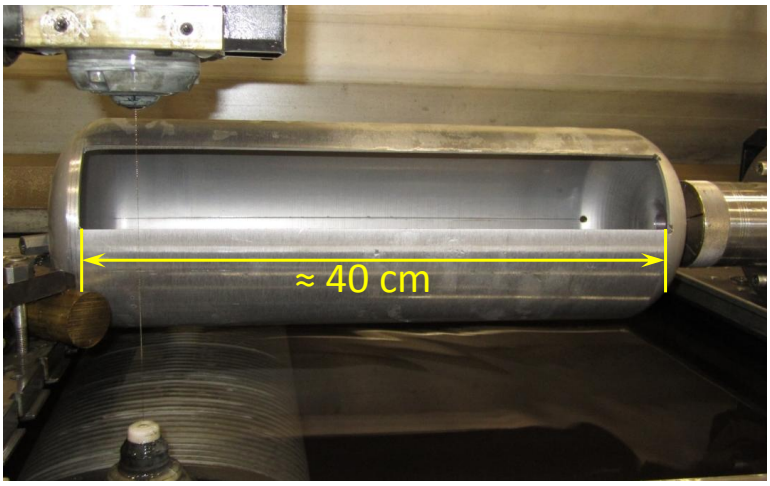

(a)

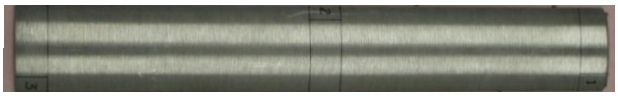

(b)

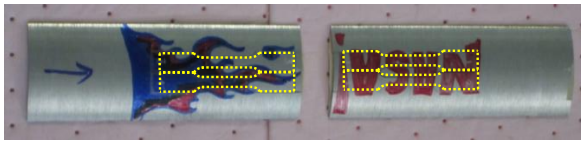

(c)

Figure B.11: a) COPV liner with portion removed using wire EDM. b) Material extracted from COPV liner for testing. c) Location of subscale dogbone specimens (outlined in yellow) used for ASTM tensile testing.

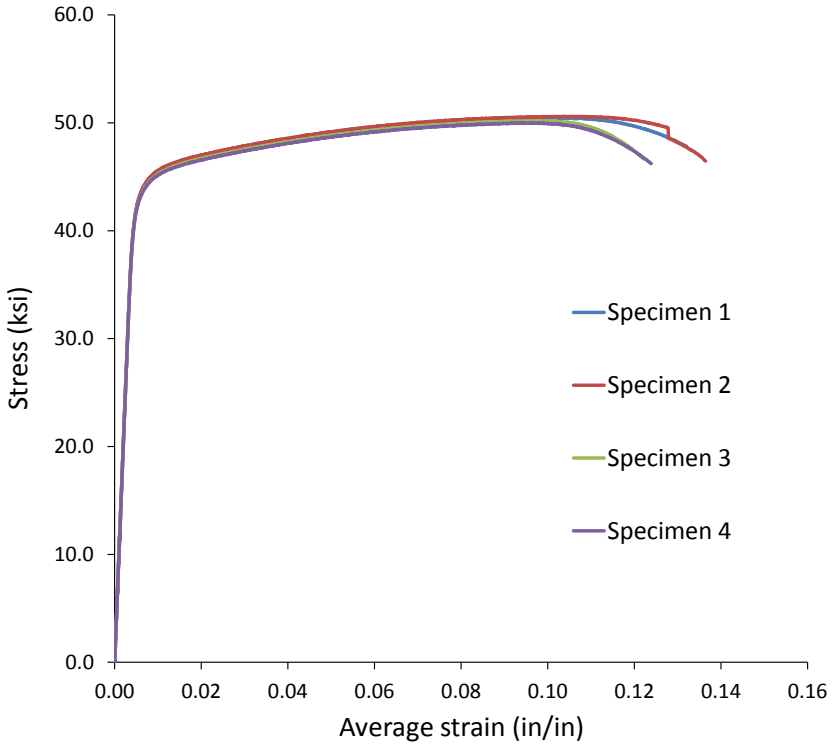

Figure B.12: ASTM tensile test results for the four specimens depicted in Fig. B.11.

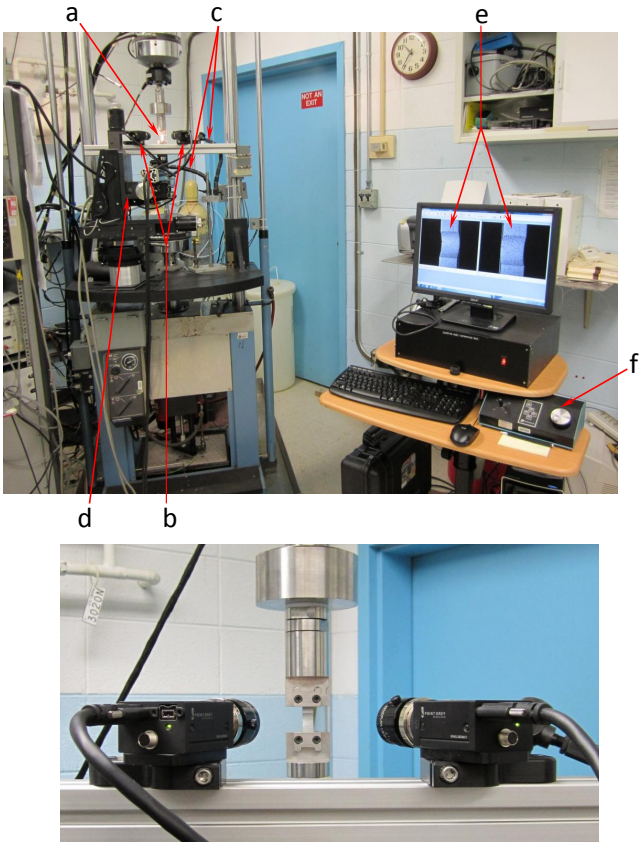

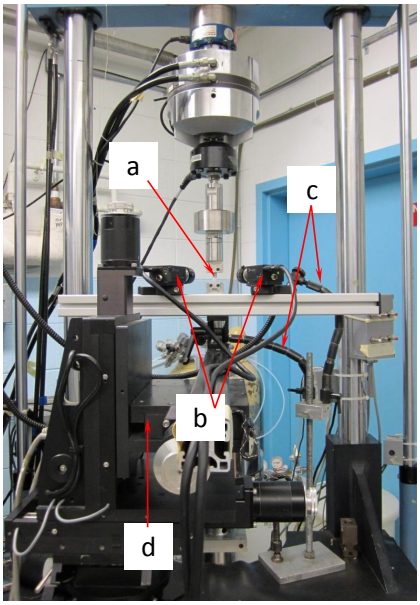

a. Specimen
b. Cameras
c. Light sources
d. Moving stage
e. Camera views in VIC-Snap software
f. Stage controller

Figure B.13: Digital image correlation test setup.

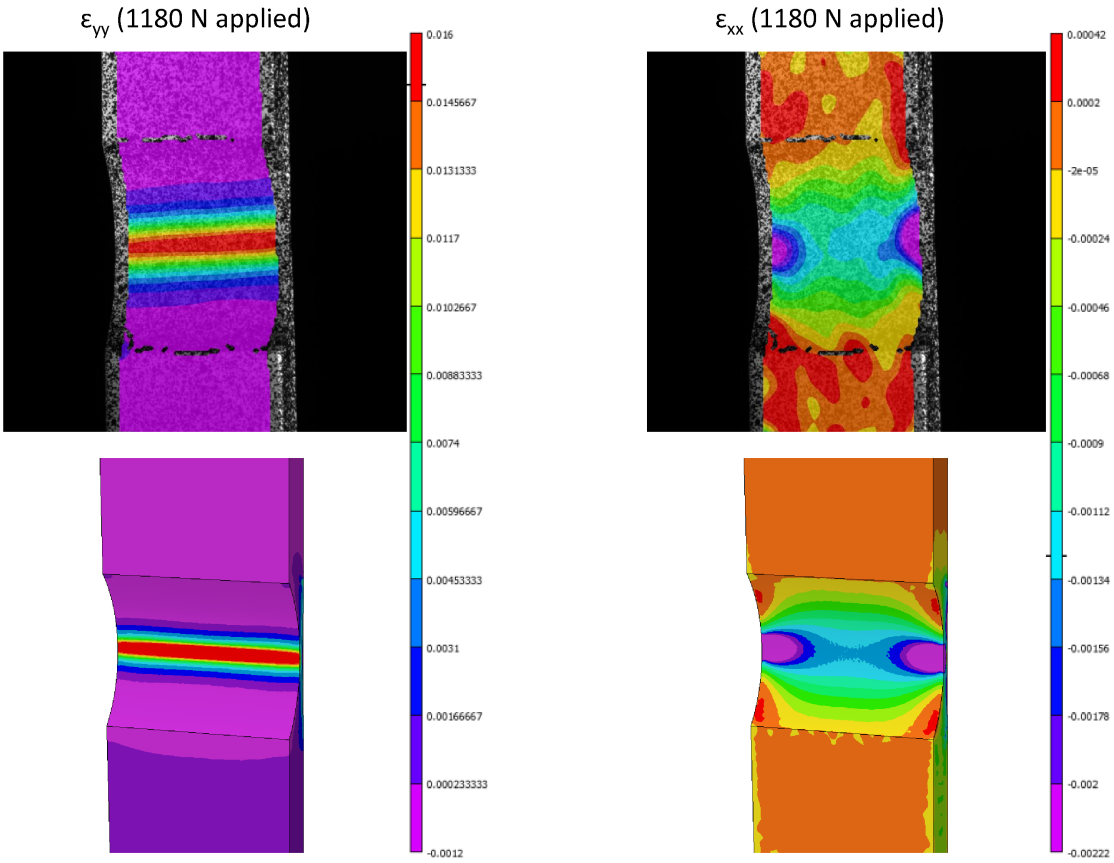

Figure B.14: Comparison between strain fields measured using digital image correlation (top) and simulated using 3-D FE analysis (bottom).

APPENDIX C

APPENDIX FOR CHAPTER 5

C.0.6 Crystal-plasticity Model Calibration

As described in [8], material-model calibration requires texture information and experimental data describing the deformation behavior of a polycrystalline aggregate of the material. Here, monotonic data are assumed to be sufficient since the aggregate, cyclic response of the aluminum alloy after initial loading was found to follow a linear path at R=0.5 (i.e. there was no marked hysteresis response of the polycrystalline aggregate at the applied-load range of interest).

In general, the calibration procedure involves two steps: (1) a high-level calibration of the material-model parameters using a reduced-order material model and (2) a three-dimensional crystal-plastic finite-element (CPFE) simulation to verify the calibrated parameters. An objective function is implemented to perform the first step of calibration. The calibration procedure seeks to minimize the objective function, i.e. the cumulative error between the experimental and simulated stress-strain response of the aggregate. The objective function serves as an interface between a constitutive, material-point simulator written in C++ and the optimization toolbox in MATLAB®. The material-point simulator is an implementation of the elasto-viscoplastic material model described in subsection 4.2.3. The objective function accepts as input a list of grain orientations representative of the material texture and an experimental stress-strain curve. Each material point (i.e. grain orientation in the list) is then passed to the material-point simulator, which returns the response of that point to a given applied-load

increment. In this way, the high-level calibration does not account for neighbor effects on each material point. A number of optimization algorithms can be used for the calibration; the current study uses a genetic algorithm to minimize the objective function. Calibrated parameters are then applied to a CPFE model to simulate experimental loading conditions. The software DREAM.3D is used to generate a synthetic polycrystal and surface mesh of the material. The surface mesh is then converted to a volume mesh using a meshing algorithm described in [187]. Figure C.1 shows a comparison between stress-strain responses from experiment and simulation for material from the central region of the pressure-vessel liner. The procedure described above can be repeated for the same alloy with varying average grain sizes by making adjustments to texture input (if necessary) and macroscopic stress-strain response.

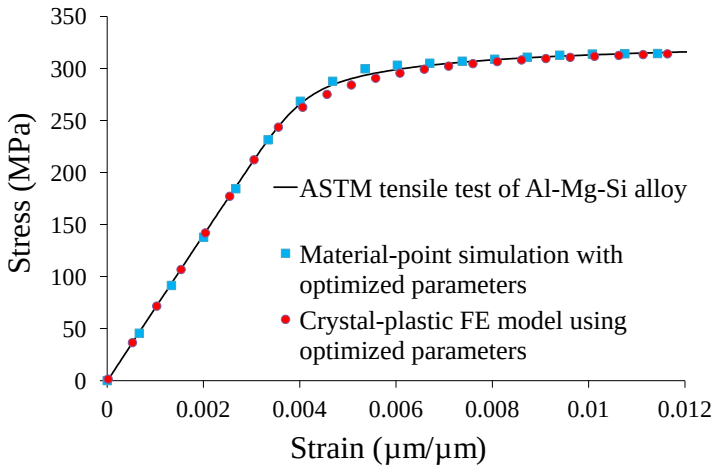

Figure C.1: Engineering stress-strain response from standardized tensile tests and simulation.

C.0.7 Mesh Convergence Study

A mesh convergence study was carried out to determine an adequate level of mesh refinement for the polycrystalline volume in the concurrent multiscale FE simulations. For a fixed polycrystalline volume, a quadratic-element mesh was generated with the following refinement levels: 6 μm, 8 μm, and 12 μm, resulting in models with 44.35M, 19.35M, and 5.20M degrees of freedom, respectively. Mesh refinement was uniform throughout the polycrystalline volume. The crystal elasto-viscoplastic material model described in subsection 4.2.3 was employed. Each model was subjected to 1% macroscopic strain applied in the z direction uniformly across the upper boundary. Simulations were performed using an in-house parallel FE solver on 1024 processor cores.

Figure C.2 shows stress results in the global loading direction at 1% globally applied strain for each of the three mesh-refinement levels. The difference in macroscopic stress-strain response for the polycrystalline aggregate among the three models is indistinguishable, as shown in Fig. C.3. Thus, a more indicative, local comparison is made using a query line A-A' that passes from one corner of the volume to the opposite, as shown in Fig. C.2. Several computed variables are quantified along the query line, including stress and strain components in the global loading direction and maximum accumulated slip. The results are presented in the plots in Fig. C.4. Based on the results, an element size equal to or less than 8 μm provides adequate convergence for the local fields considered.

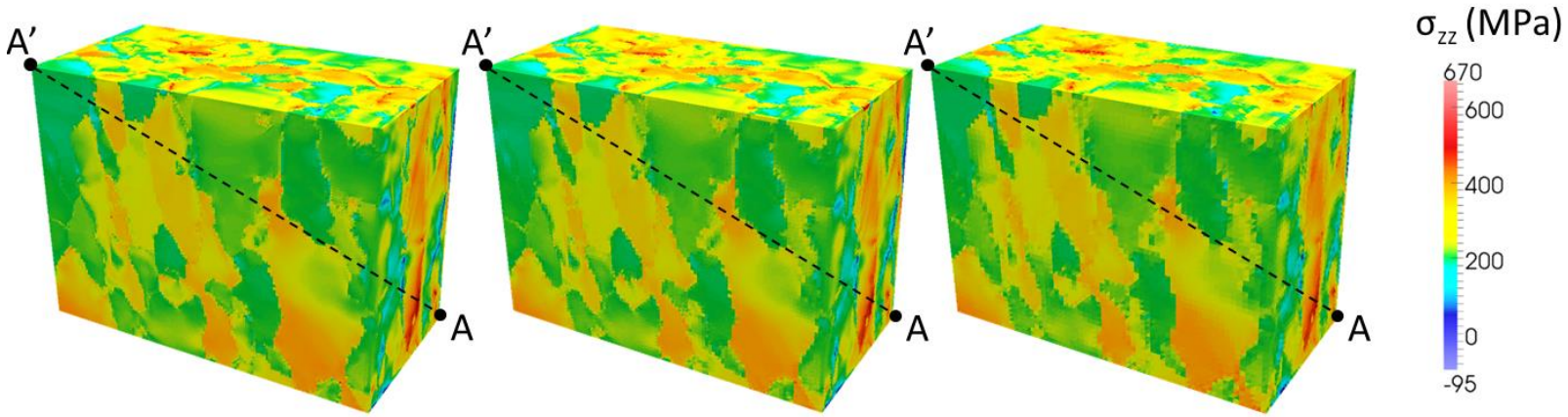

Figure C.2: CPFE simulation results for volume with three levels of mesh refinement: 6 μm (left), 8 μm (middle), 12 μm (right). Fields depict stress component in the global loading direction, z, at 1% globally applied strain. Query line A-A′ shown for reference. Mesh omitted for visualization purposes.

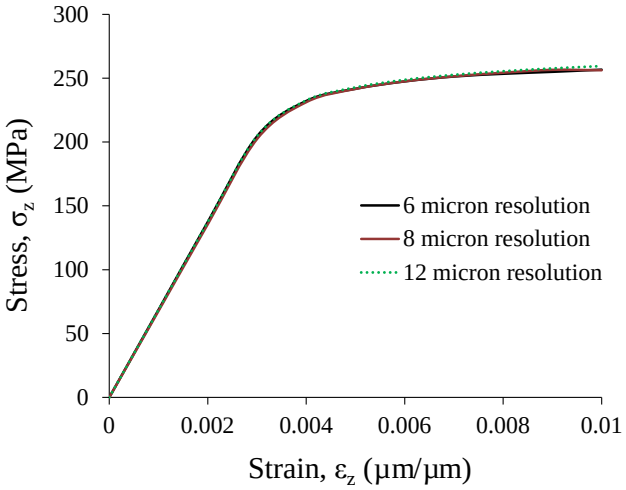

Figure C.3: Global (average) stress-strain response for each of the three mesh-refinement levels depicted in Fig. C.2.

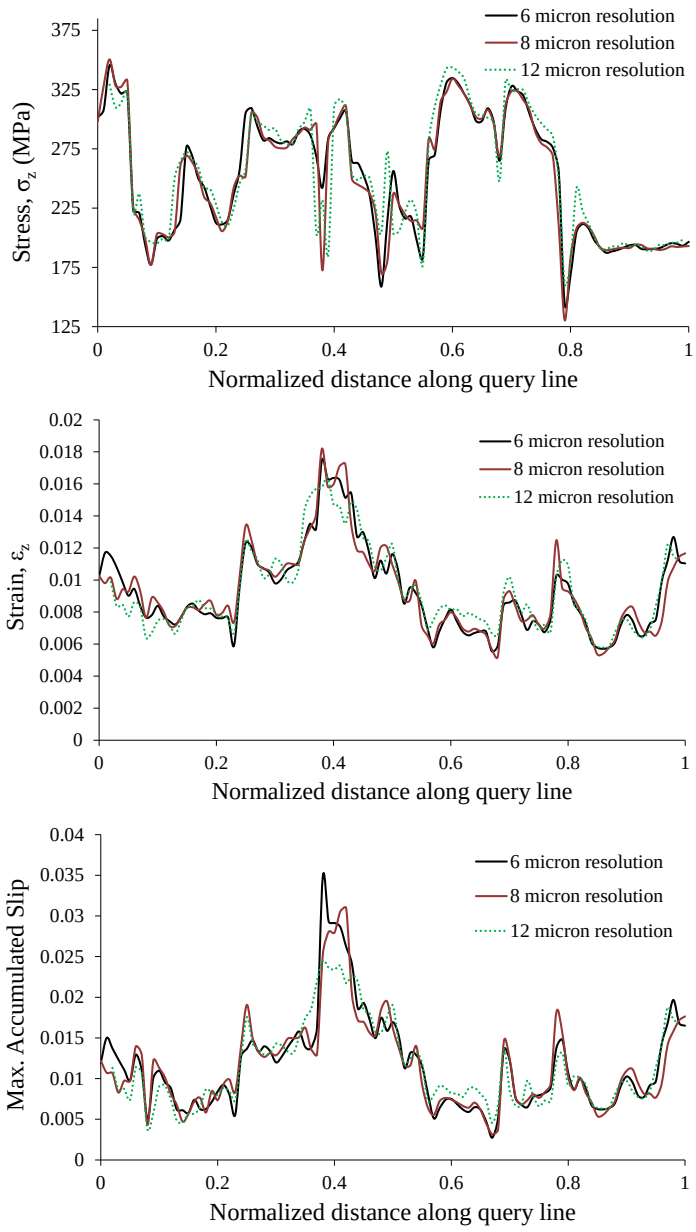

Figure C.4: Local response values along query line A-A′ for each of the three mesh-refinement levels depicted in Fig. C.2.

BIBLIOGRAPHY

[1] A.D. Spear, A.R. Priest, M.G. Veilleux, J.D. Hochhalter, and A.R. Ingraffea. Surrogate modeling of high-fidelity fracture simulations for real-time residual strength predictions. *AIAA journal*, 49(12):2770–2782, 2011.

[2] A.D. Spear, A.R. Priest, J.D. Hochhalter, M.G. Veilleux, and A.R. Ingraffea. Surrogate modeling of 3D high-fidelity fracture simulations for real-time residual strength predictions. *NASA/TM-2011-216879*, 2011.

[3] A.D. Spear, J.D. Hochhalter, and A.R. Ingraffea. Simulation of discrete-source damage propagation and residual strength of aircraft structures. In *Proceedings from the 12th International Conference on Fracture*, 2009.

[4] A.D. Spear, M.G. Veilleux, J.E. Bozek, and A.R. Ingraffea. Structural assessment and prognosis using a multi-scale, fracture mechanics-based approach. In *2010 Aircraft Airworthiness and Sustainment Conference Proceedings*, Austin, TX, May 2010.

[5] A.D. Spear and A.R. Ingraffea. Effect of chemical milling on low-cycle fatigue behavior of an Al-Mg-Si alloy. *Corrosion Science*, 68(0):144 – 153, 2013.

[6] A.D. Spear, S.F. Li, J.F. Lind, R.M. Suter, and A.R. Ingraffea. 3D characterization of microstructurally small fatigue-crack evolution using quantitative fractography combined with post-mortem X-ray tomography and high-energy X-ray diffraction microscopy. *Acta Materialia*, 2014 (accepted).

[7] A.D. Spear and A.R. Ingraffea. Microstructurally small fatigue crack growth in thin, aluminum-alloy, pressure vessel liner. *Procedia Engineering*, 10:686–691, 2011.

[8] A.D. Spear, S.F. Li, A.R. Cerrone, J.F. Lind, R.M. Suter, and A.R. Ingraffea. 3D microscale characterization and crystal-plastic fe simulation of fatigue-crack nucleation and propagation in an aluminum alloy. In *Materials Science & Technology (MS&T) 2013 Proceedings*, pages 1641–1648, 2013.

[9] D. Hughes and M.A. Dornheim. No flight controls. *Aviation Week & Space Technology*, 159(23):42 – 43, 2003.

[10] Depressurisation - 475 km north-west of Manila, Philippines - 25 July

2008. ATSB Transportation Safety Report 2, Australian Transport Safety Bureau, Nov 2009.

[11] A.R. Ingraffea. *Computational Fracture Mechanics*, volume 2 of *Encyclopedia of Computational Methods in Mechanics*. John Wiley and Sons, 2nd edition, 2007.

[12] J.C. Newman, Jr. Finite-element analysis of crack growth under monotonic and cyclic loading. *ASTM STP 637*, pages 56–80, 1977.

[13] D.S. Dawicke, M.A. Sutton, J.C. Newman, Jr., and C.A. Bigelow. Measurement and analysis of critical CTOA for an aluminum alloy sheet. *ASTM STP 1220*, 1995.

[14] X. Deng and J.C. Newman, Jr. A study of some issues in stable tearing crack growth simulations. *Engineering Fracture Mechanics*, 64(3):291 – 304, 1999.

[15] B.R. Seshadri, J.C. Newman, Jr., D.S. Dawicke, and R.D. Young. Fracture analysis of the FAA/NASA wide stiffened panels. Technical Report 208982, NASACP, 1999.

[16] M.A. Sutton, M.L. Boone, F. Ma, and J.D. Helm. A combined modeling-experimental study of the crack opening displacement fracture criterion for characterization of stable crack growth under mixed mode I/II loading in thin sheet materials. *Engineering Fracture Mechanics*, 66(2):171 – 185, 2000.

[17] C.S. Chen, A.R. Ingraffea, and P.A. Wawrzynek. Prediction of residual strength and curvilinear crack growth in aircraft fuselages. *AIAA Journal*, 40:1644–1652, Aug 2002.

[18] J.C. Newman, Jr., D.S. Dawicke, and B.R. Seshadri. Residual strength analyses of stiffened and un-stiffened panels–Part I: laboratory specimens. *Engineering Fracture Mechanics*, 70(3-4):493 – 507, 2003.

[19] B.R. Seshadri, J.C. Newman, Jr., and D.S. Dawicke. Residual strength analyses of stiffened and unstiffened panels–Part II: wide panels. *Engineering Fracture Mechanics*, 70(3-4):509 – 524, 2003.

[20] D.S. Dawicke, J.C. Newman, Jr., and C.A. Bigelow. Three-dimensional

CTOA and constraint effects during stable tearing in a thin-sheet material. *ASTM STP 1256*, pages 358–379, 1995.

[21] A. S. Gullerud, R.H. Dodds, Jr., R. W. Hampton, and D. S. Dawicke. Three-dimensional modeling of ductile crack growth in thin sheet metals: computational aspects and validation. *Engineering Fracture Mechanics*, 63(4):347 – 374, 1999.

[22] B.R. Seshadri, S.C. Forth, W.M. Johnston, Jr., and M.S. Domack. Application of CTOA/CTOD in the residual strength analysis of built-up and integral structures. In *11th International Conference on Fracture*, Turin, Italy, Mar 2005.

[23] F. Erdogan and G.C. Sih. On the crack extension of plates under plane loading and transverse shear. *Journal of Basic Engineering*, 85(4):519–527, 1963.

[24] M.A. Hussain, S.L. Pu, and J.H. Underwood. Strain energy release rate for a crack under combined mode I and mode II. *ASTM STP 560*, 1974.

[25] G.C. Sih. Strain-energy-density factor applied to mixed-mode crack problems. *International Journal of Fracture*, 10(3):305–321, 1974.

[26] M.A. Sutton, X. Deng, F. Ma, J.C. Newman, Jr., and M.A. James. Development and application of a crack tip opening displacement-based mixed mode fracture criterion. *International Journal of Solids and Structures*, 37(26):3591 – 3618, 2000.

[27] J. Zuo, X. Deng, M.A. Sutton, and C.S. Cheng. Three-dimensional crack growth in ductile materials: Effect of stress constraint on crack tunneling. *Journal of Pressure Vessel Technology*, 130(3):031401, 2008.

[28] M.A. James and D. Swenson. A software framework for two-dimensional mixed mode I/II elastic-plastic fracture. *ASTM STP 1359*, 1999.

[29] W. Lan, X. Deng, and M.A. Sutton. Three-dimensional finite element simulations of mixed-mode stable tearing crack growth experiments. *Engineering Fracture Mechanics*, 74(16):2498 – 2517, 2007.

[30] J. Zuo, X. Deng, and M.A. Sutton. Computational aspects of three-dimensional crack growth simulations. *ASME Conference Proceedings*, 2004(47020):385–391, 2004.

[31] N.V. Queipo, R.T. Haftka, W. Shyy, T. Goel, R. Vaidyanathan, and P.K. Tucker. Surrogate-based analysis and optimization. *Progress in Aerospace Sciences*, 41(1):1 – 28, 2005.

[32] R.D. Reed and R.J. Marks. *Neural Smithing: Supervised Learning in Feedforward Artificial Neural Networks*. MIT Press, Cambridge, MA, USA, 1998.

[33] J.N. Kudva, N. Munir, and P.W. Tan. Damage detection in smart structures using neural networks and finite-element analyses. *Smart Materials and Structures*, 1(2), 1992.

[34] R. Ceravolo, A. de Stefano, and D. Sabia. Hierarchical use of neural techniques in structural damage recognition. *Smart Materials and Structures*, 4(4):270–280, 1995.

[35] Y.C. Liang and C. Hwu. On-line identification of holes/cracks in composite structures. *Smart Materials and Structures*, 10(4):599–609, 2001.

[36] S.W. Liu, J.H. Huang, J.C. Sung, and C.C. Lee. Detection of cracks using neural networks and computational mechanics. *Computer Methods in Applied Mechanics and Engineering*, 191(25-26):2831 – 2845, 2002.

[37] Y.Q. Ni, B.S. Wang, and J.M. Ko. Constructing input vectors to neural networks for structural damage identification. *Smart Materials and Structures*, 11(6):825–833, 2002.

[38] Y. Lu, L. Ye, Z. Su, L. Zhou, and L. Cheng. Artificial neural network (ANN)-based crack identification in aluminum plates with Lamb wave signals. *Journal of Intelligent Material Systems and Structures*, 20(1):39–49, 2009.

[39] Z. Su and L. Ye. *Application of Algorithms for Identifying Structural Damage - Case Studies*, volume 48 of *Lecture Notes in Applied and Computational Mechanics*. Springer Berlin / Heidelberg, 2009.

[40] A. Ouenes. Practical application of fuzzy logic and neural networks to fractured reservoir characterization. *Computers & Geosciences*, 26(8):953 – 962, 2000.

[41] R.M. Pidaparti, S. Jayanti, and M.J. Palakal. Residual strength and corrosion rate predictions of aging aircraft panels: Neural network study. *Journal of Aircraft*, 39(1):175 – 180, 2002.

[42] S. Mohanty, A. Chattopadhyay, P. Peralta, and S. Das. Bayesian statistic based multivariate Gaussian process approach for offline/online fatigue crack growth prediction. *Experimental Mechanics*, pages 1–11, 2010.

[43] R. Hambli, A. Chamekh, and H. Bel Hadj Salah. Real-time deformation of structure using finite element and neural networks in virtual reality applications. *Finite Elements in Analysis and Design*, 42(11):985 – 991, 2006.

[44] S. Sankararaman, Y. Ling, and S. Mahadevan. Statistical inference of equivalent initial flaw size with complicated structural geometry and multi-axial variable amplitude loading. *International Journal of Fatigue*, 32(10):1689 – 1700, 2010.

[45] R.L. Hinrichsen, A.G. Kurtz, J.T. Wang, C.M. Belcastro, and J.L. Parks. Modeling projectile damage in transport aircraft wing structures. *AIAA Journal*, 46:328–335, February 2008.

[46] ABAQUS 6.8 Documentation, Dassault Systèmes Simulia Corp., 2008.

[47] V. Ramachandran, A.C. Raghuram, R.V. Krishnan, and S.K. Bhaumik. *Failure Analysis of Engineering Structures: Methodology and Case Histories*, chapter 6, page 45. ASM International, Materials Park, OH 44073-0002, 2005.

[48] M.D. Mckay, R.J. Beckman, and W.J. Conover. A comparison of three methods for selecting values of input variables in the analysis of output from a computer code. *Technometrics*, 42(1):55–61, 2000.

[49] MATLAB R2009a Documentation, The MathWorks, Inc., 2009.

[50] P.A. Wawrzynek, B.J. Carter, and A.R. Ingraffea. Advances in simulation of arbitrary 3D crack growth using FRANC3D/NG. In *12th International Conference on Fracture*, Ottawa, Canada, July 2009.

[51] D. Broek. *Elementary Engineering Fracture Mechanics*, chapter 14. Martinus Nijhoff Publishers, 4th edition, 1986.

[52] H. Demuth and M. Beale. *Neural Network Toolbox For Use with MATLAB (Version 4)*. The MathWorks, Inc., 3 Apple Hill Drive, Natick, MA 01760-2098, 2004.

[53] M.T. Hagan and M.B. Menhaj. Training feedforward networks with the

Marquardt algorithm. *IEEE Transactions on Neural Networks*, 5(6):989 –993, November 1994.

[54] D. M. Hamby. A review of techniques for parameter sensitivity analysis of environmental models. *Environmental Monitoring and Assessment*, 32:135–154, 1994. 10.1007/BF00547132.

[55] A.A. Wells. Unstable crack propagation in metals: cleavage and fast fracture. In *Proceedings of the Crack Propagation Symposium*, volume 1, pages 210–230, Cranfield, England, 1961. College of Aeronautics.

[56] H. Anderson. A finite-element representation of stable crack-growth. *Journal of the Mechanics and Physics of Solids*, (21):337–356, 1973.

[57] A.U. de Koning. A contribution to the analysis of quasi static crack growth in steel materials. In *4th International Conference on Fracture*, number 3, pages 25–31, 1977.

[58] J.C. Newman, Jr. An evaluation of fracture analysis methods. *ASTM STP 896*, pages 5–96, 1985.

[59] J.C. Newman, Jr., M.A. James, and U. Zerbst. A review of the CTOA/CTOD fracture criterion. *Engineering Fracture Mechanics*, 70(3-4):371 – 385, 2003.

[60] M.A. Sutton, J. Yan, X. Deng, C.S. Cheng, and P. Zavattieri. Three-dimensional digital image correlation to quantify deformation and crack-opening displacement in ductile aluminum under mixed-mode I/III loading. *Optical Engineering*, 46(5):051003, 2007.

[61] W. Lan, X. Deng, and M.A. Sutton. Investigation of crack tunneling in ductile materials. *Engineering Fracture Mechanics*, 77(14):2800 – 2812, 2010.

[62] M.A. James. *A plane stress finite element model for elastic-plastic mode* I/II *crack growth*. PhD thesis, Kansas State University, 1998.

[63] I.L. Lim, I.W. Johnston, S.K. Choi, and V. Murti. An improved numerical inverse isoparametric mapping technique for 2D mesh rezoning. *Engineering Fracture Mechanics*, 41(3):417 – 435, 1992.

[64] M. Arcan, Z. Hashin, and A. Voloshin. A method to produce uniform

plane-stress states with applications to fiber-reinforced materials. *Experimental Mechanics*, (141), 1977.

[65] B.A. Amstutz, M.A. Sutton, D.S. Dawicke, and J.C. Newman, Jr. An experimental study of CTOD for mode I/mode II stable crack growth in thin 2024-T3 aluminum specimens. *ASTM STP 1256*, pages 256–271, 1995.

[66] B.A. Amstutz, M.A. Sutton, D.S. Dawicke, and M.L. Boone. Effects of mixed mode I/II loading and grain orientation on crack initiation and stable tearing in 2024-T3 aluminum. *ASTM STP 1296*, pages 105–125, 1997.

[67] NASGRO Material Database, Southwest Research Institute®.

[68] M. Kulak, R. Bucci, H. Skyut, G. Bray, and J.C. Newman, Jr. Fatigue crack growth and residual strength analysis of TWIST spectrum loaded integrally stiffened panels simulating a lower wing skin two bay crack scenario. In J.L. Rudd and R.M. Bader, editors, *ICAF 20, 1999 - Structural Integrity for the Next Millenium*, volume I, Bellevue, Washington, USA, July 1999. International Committee on Aeronautical Fatigue, EMAS Publishing.

[69] G.H. Bray, R.J. Bucci, and R.L. Brazill. Lessons neglected: Effects of moist air on fatigue and fatigue crack growth in aluminum alloys. In *7th International Conference on Aluminum Alloys*, Charlottesville, VA, 2000.

[70] B.R. Seshadri, M.A. James, W.M. Johnston, Jr., R.D. Young, and J.C. Newman, Jr. Recent developments in the analysis of monolithic structures at NASA Langley. In *Sixth Joint FAA/DoD/NASA Conference on Aging Aircraft*, San Francisco, CA, Sept 2002.

[71] J.W. Dini. Chemical milling. *International Metallurgical Reviews*, 20, 1975.

[72] D. Novovic, R.C. Dewes, D.K. Aspinwall, W. Voice, and P. Bowen. The effect of machined topography and integrity on fatigue life. *International Journal of Machine Tools and Manufacture*, 44:125 – 134, 2004.

[73] P. Maiya and D. Busch. Effect of surface roughness on low-cycle fatigue behavior of type 304 stainless steel. *Metallurgical and Materials Transactions A*, 6:1761–1766, 1975.

[74] M.R. Bayoumi and A.K. Abdellatif. Effect of surface finish on fatigue strength. *Engineering Fracture Mechanics*, 51(5):861 – 870, 1995.

[75] T.T. Lamark, Y. Estrin, and X.Z. Hu. Fatigue of aluminum 6061-T6 and magnesium AS21X under variable amplitude loading. In A.V. Dyskin, X. Hu, and E. Sahouryeh, editors, *Structural Integrity and Fracture*. Swets & Zeitlinger Publishers, 2002.

[76] D. Taylor and O.M. Clancy. Fatigue performance of machined surfaces. *Fatigue and Fracture of Engineering Materials and Structures*, 14(2-3):329–336, 1991.

[77] W.A. Wood. Formation of fatigue cracks. *Philosophical Magazine*, 3:692–699, 1958.

[78] R.W. Suhr. The effect of surface finish on high cycle fatigue of a low alloy steel. In K.J. Miller and E.R. de los Rios, editors, *Mechanical Engineering Publications*. London, 1986.

[79] R.W. Suhr. *High Cycle Fatigue*, pages 226–287. The Institute of Metals, London, 1988.

[80] L. Wagner. Mechanical surface treatments on titanium, aluminum and magnesium alloys. *Materials Science and Engineering: A*, 263(2):210 – 216, 1999.

[81] M.F.E. Ibrahim and K.J. Miller. Determination of fatigue crack initiation life. *Fatigue & Fracture of Engineering Materials & Structures*, 2(4):351–360, 1979.

[82] P.S. Maiya. Effects of surface roughness and strain range on the low-cycle fatigue behavior of type 304 stainless steel. *Scripta Metallurgica*, 9:1277–1282, 1975.

[83] G.H. Bray, R.J. Bucci, E.L. Colvin, and M. Kulak. Effect of prior corrosion on the S/N fatigue performance of aluminum sheet alloys 2024-T3 and 2524-T3. In W.A. Van Der Sluys, R.S. Piascik, and R. Zawierucha, editors, *Effects of the Environment on the Initiation of Crack Growth, ASTM STP 1298*. American Society for Testing and Materials, 1997.

[84] K.K. Sankaran, R. Perez, and K.V. Jata. Effects of pitting corrosion on the fatigue behavior of aluminum alloy 7075-T6: modeling and experimental studies. *Materials Science and Engineering: A*, 297:223 – 229, 2001.

[85] R.M. Pidaparti and A.S. Rao. Analysis of pits induced stresses due to metal corrosion. *Corrosion Science*, 50(7):1932 – 1938, 2008.

[86] M. Shahzad, M. Chaussumier, R. Chieragatti, C. Mabru, and F. Rezai-Aria. Surface characterization and influence of anodizing process on fatigue life of Al 7050 alloy. *Materials & Design*, 32(6):3328 – 3335, 2011.

[87] J.T. Burns, J.M. Larsen, and R.P. Gangloff. Driving forces for localized corrosion-to-fatigue crack transition in Al-Zn-Mg-Cu. *Fatigue & Fracture of Engineering Materials & Structures*, 34(10):745–773, 2011.

[88] E.J. Dolley, B. Lee, and R.P. Wei. The effect of pitting corrosion on fatigue life. *Fatigue & Fracture of Engineering Materials & Structures*, 23(7):555–560, 2000.

[89] D.L DuQuesnay, P.R Underhill, and H.J Britt. Fatigue crack growth from corrosion damage in 7075-T6511 aluminium alloy under aircraft loading. *International Journal of Fatigue*, 25(5):371 – 377, 2003.

[90] J.T. Burns, S. Kim, and R.P. Gangloff. Effect of corrosion severity on fatigue evolution in Al-Zn-Mg-Cu. *Corrosion Science*, 52(2):498 – 508, 2010.

[91] X.D. Li, X.S. Wang, H.H. Ren, Y.L. Chen, and Z.T. Mu. Effect of prior corrosion state on the fatigue small cracking behaviour of 6151-T6 aluminum alloy. *Corrosion Science*, 55:26 – 33, 2012.

[92] K. van der Walde, J.R. Brockenbrough, B.A. Craig, and B.M. Hillberry. Multiple fatigue crack growth in pre-corroded 2024-T3 aluminum. *International Journal of Fatigue*, 27:1509 – 1518, 2005.

[93] K. van der Walde and B.M. Hillberry. Initiation and shape development of corrosion-nucleated fatigue cracking. *International Journal of Fatigue*, 29(7):1269 – 1281, 2007.

[94] S.I. Rokhlin, J.-Y. Kim, H. Nagy, and B. Zoofan. Effect of pitting corrosion on fatigue crack initiation and fatigue life. *Engineering Fracture Mechanics*, 62:425 – 444, 1999.

[95] H.D. Beeson, D.D. Davis, W.L. Ross, Sr., and R.M. Tapphorn. Composite overwrapped pressure vessels. Technical Report TP-2002-210769, NASA, 2002.

[96] P.B. McLaughlan, S.C. Forth, and L.R. Grimes-Ledesma. Composite overwrapped pressure vessels, A primer. Technical Report SP-2011-573, NASA, 2011.

[97] Statement of work: Mars Exploration Rover propulsion system tank liner chem-milling, 2001. Issued for Carleton Pressure Technology Division (unpublished).

[98] T. Savas and J. Earthman. Surface characterization of 7075-T73 aluminum exposed to anodizing pretreatment solutions. *Journal of Materials Engineering and Performance*, 17:674–681, 2008.

[99] ASTM E8-11. Standard Test Methods for Tension Testing of Metallic Materials. American Society for Testing and Materials International, West Conshohocken, PA, 2011.

[100] Understanding extruded aluminum alloys: Alloy 6061. Datasheet, ALCOA, 2002. http://www.alcoa.com/adip/catalog/pdf/Extruded_Alloy_6061.pdf.

[101] J.H. Gross, D.E. Gucer, and R.D. Stout. The plastic fatigue strength of pressure vessel steels. *Welding Journal*, 33:31s–39s, Jan 1954.

[102] M.R. Gross. Engineering materials evaluation by reversed bending. In *Manual on Low Cycle Fatigue Testing, ASTM STP 465*, pages 149–162. American Society for Testing and Materials, 1969.

[103] American Society for Metals. Metals Handbook Ninth Edition. In *Metallography and Microstructures*, volume 9, chapter Aluminum Alloys. 1985.

[104] F. Marinello, P. Bariani, E. Savio, A. Horsewell, and L. De Chiffre. Critical factors in SEM 3D stereo microscopy. *Measurement Science and Technology*, 19(6):065705, 2008.

[105] W. Drzazga, J. Paluszynski, and W. Słówko. Three-dimensional characterization of microstructures in a SEM. *Measurement Science and Technology*, 17(1):28, 2006.

[106] J. Paluszynski and W. Słówko. Surface reconstruction with the photometric method in SEM. *Vacuum*, 78(24):533 – 537, 2005.

[107] Z. Szklarska-Smialowska. Pitting corrosion of aluminum. *Corrosion Science*, 41(9):1743 – 1767, 1999.

[108] G.S. Chen, M. Gao, and R.P. Wei. Microconstituent-induced pitting corrosion in aluminum alloy 2024-T3. *Corrosion*, 52(1):8–15, 1996.

[109] B. Zaid, D. Saidi, A. Benzaid, and S. Hadji. Effects of pH and chloride concentration on pitting corrosion of AA6061 aluminum alloy. *Corrosion Science*, 50(7):1841 – 1847, 2008.

[110] D. Landolt. Fundamental aspects of electropolishing. *Electrochimica Acta*, 32(1):1–11, 1987.

[111] L. De Chiffre, P. Lonardo, H. Trumpold, D.A. Lucca, G. Goch, C.A. Brown, J. Raja, and H.N. Hansen. Quantitative characterisation of surface texture. *CIRP Annals - Manufacturing Technology*, 49(2):635 – 652, 2000.

[112] K.J. Stout, P.J. Sullivan, W.P. Dong, E. Mainsah, N. Luo, T. Mathia, and H. Zahouani. The development of methods for the characterisation of roughness in three dimensions. Eur 15178 en, Commission of the European Communities, 1993.

[113] ISO/FDIS 25178-2. Geometrical product specificiation (GPS) - surface texture: areal - part 2: terms, definitions and surface texture parameters. International Organization for Standardization, Geneva, Switzerland, 2010.

[114] R. Ihaka and R. Gentleman. R: A language for data analysis and graphics. *Journal of Computational and Graphical Statistics*, 5(3):299–314, 1996.

[115] D.C. Slavik, J.A. Wert, and R.P. Gangloff. Determining fracture facet crystallography using electron backscatter patterns and quantitative tilt fractography. *Journal of Materials Research*, 8:2482–2491, 1993.

[116] Y. Pang and P. Wynblatt. Correlation between grain-boundary segregation and grain-boundary plane orientation in Nb-Doped TiO2. *Journal of the American Ceramic Society*, 88(8):2286–2291, 2005.

[117] Y.J. Ro, S.R. Agnew, and R.P. Gangloff. Environmental fatigue-crack surface crystallography for Al-Zn-Cu-Mg-Mn/Zr. *Metallurgical and Materials Transactions A*, 39:1449–1465, 2008.

[118] J.E. Hilliard. Quantitative analysis of scanning electron micrographs. *Journal of Microscopy*, 95:45–58, 1972.

[119] Y.J. Ro, S.R. Agnew, and R.P. Gangloff. Uncertainty in the determination of fatigue crack facet crystallography. *Scripta Materialia*, 52(6):531 – 536, 2005.

[120] P.J.E. Forsyth. Fatigue damage and crack growth in aluminium alloys. *Acta Metallurgica*, 11(7):703–715, 1963.

[121] Y. Takahashi, T. Shikama, S. Yoshihara, T. Aiura, and H. Noguchi. Study on dominant mechanism of high-cycle fatigue life in 6061-T6 aluminum alloy through microanalyses of microstructurally small cracks. *Acta Materialia*, 60(67):2554 – 2567, 2012.

[122] J.D. Hochhalter, D.J. Littlewood, M.G. Veilleux, J.E. Bozek, A.M. Maniatty, A.D. Rollett, and A.R. Ingraffea. A geometric approach to modeling microstructurally small fatigue crack formation: III Development of a semi-empirical model for nucleation. *Modelling and Simulation in Materials Science and Engineering*, 19(3), 2011.

[123] ANSI/AIAA S-081-2000 Standard. *Space Systems - Composite Overwrapped Pressure Vessels (COPVs)*, December 2000.

[124] S. Suresh and R. Ritchie. Propagation of short fatigue cracks. *International Materials Reviews*, 29(1):445–475, 1984.

[125] S. Suresh. Fatigue of materials. 1998. *UK: Cambridge University Press, Cambridge*, 1998.

[126] K.S. Chan. Roles of microstructure in fatigue crack initiation. *International Journal of Fatigue*, 32(9):1428 – 1447, 2010.

[127] U. Krupp. *Fatigue crack propagation in metals and alloys: Microstructural aspects and modeling concepts*. Wiley-VCH, 2007.

[128] C.J. Taylor, T. Zhai, A.J. Wilkinson, and J.W. Martin. Influence of grain orientations on the initiation of fatigue damage in an Al-Li alloy. *Journal of Microscopy*, 195(3):239–247, 1999.

[129] F.P.E. Dunne, A.J. Wilkinson, and R. Allen. Experimental and computa-

tional studies of low cycle fatigue crack nucleation in a polycrystal. *International Journal of Plasticity*, 23(2):273–295, 2007.

[130] J. Payne, G. Welsh, R.J. Christ, Jr., J. Nardiello, and J.M. Papazian. Observations of fatigue crack initiation in 7075-T651. *International Journal of Fatigue*, 32(2):247–255, 2010.

[131] Y.M. Hu, W. Floer, U. Krupp, and H.-J Christ. Microstructurally short fatigue crack initiation and growth in Ti-6.8Mo-4.5Fe-1.5Al. *Materials Science and Engineering: A*, 278(1-2):170 – 180, 2000.

[132] V.K. Gupta, R.P. Gangloff, and S.R. Agnew. Diffraction characterization of microstructure scale fatigue crack growth in a modern Al-Zn-Mg-Cu alloy. *International Journal of Fatigue*, 42(0):131 – 146, 2012.

[133] D.L. McDowell and F.P.E. Dunne. Microstructure-sensitive computational modeling of fatigue crack formation. *International Journal of Fatigue*, 32(9):1521–1542, 2010.

[134] P.A. Davies and V. Randle. Combined application of electron backscatter diffraction and stereo-photogrammetry in fractography studies. *Journal of Microscopy*, 204(1):29–38, 2001.

[135] Y.J. Ro, S.R. Agnew, and R.P. Gangloff. Crystallography of fatigue crack propagation in precipitation-hardened Al-Cu-Mg/Li. *Metallurgical and Materials Transactions A*, 38(12):3042–3062, 2007.

[136] V.K. Gupta and S.R. Agnew. Fatigue crack surface crystallography near crack initiating particle clusters in precipitation hardened *legacy* and *modern* Al-Zn-Mg-Cu alloys. *International Journal of Fatigue*, 33(9):1159–1174, 2011.

[137] G.G. Garrett and J.F. Knott. Crystallographic fatigue crack growth in aluminium alloys. *Acta Metallurgica*, 23(7):841–848, 1975.

[138] S.A. Willard. Use of marker bands for determination of fatigue crack growth rates and crack front shapes in pre-corroded coupons. *NASA/CR-97-206291*, December 1997.

[139] S.A. Barter, L. Molent, and R.J.H. Wanhill. Marker loads for quantitative fractography of fatigue cracks in aerospace alloys. In M.J. Bos, editor,

ICAF 2009, Bridging the Gap between Theory and Operational Practice, pages 15–54. Springer Netherlands, 2009.

[140] S. Kim, J.T. Burns, and R.P. Gangloff. Fatigue crack formation and growth from localized corrosion in Al-Zn-Mg-Cu. *Engineering Fracture Mechanics*, 76(5):651 – 667, 2009.

[141] J.T. Burns, J.M. Larsen, and R.P. Gangloff. Effect of initiation feature on microstructure-scale fatigue crack propagation in Al-Zn-Mg-Cu. *International Journal of Fatigue*, 42:104 – 121, 2012.

[142] W. Ludwig, J.-Y. Buffière, S. Savelli, and P. Cloetens. Study of the interaction of a short fatigue crack with grain boundaries in a cast Al alloy using X-ray microtomography. *Acta Materialia*, 51(3):585–598, 2003.

[143] E. Ferrie, J.-Y. Buffiere W., and Ludwig. 3d characterisation of the nucleation of a short fatigue crack at a pore in a cast al alloy using high resolution synchrotron microtomography. *International Journal of Fatigue*, 27(10):1215–1220, 2005.

[144] H. Proudhon, J.-Y. Buffière, and S. Fouvry. Three-dimensional study of a fretting crack using synchrotron x-ray micro-tomography. *Engineering Fracture Mechanics*, 74(5):782–793, 2007.

[145] T.J. Marrow, J.-Y. Buffiere, P.J. Withers, G. Johnson, and D. Engelberg. High resolution X-ray tomography of short fatigue crack nucleation in austempered ductile cast iron. *International Journal of Fatigue*, 26(7):717–725, 2004.

[146] S. Birosca, J.-Y. Buffiere, M. Karadge, and M. Preuss. 3-D observations of short fatigue crack interaction with lamellar and duplex microstructures in a two-phase titanium alloy. *Acta Materialia*, 59(4):1510–1522, 2011.

[147] H. Proudhon, A. Moffat, I. Sinclair, and J.-Y. Buffiere. Three-dimensional characterisation and modelling of small fatigue corner cracks in high strength Al-alloys. *Comptes Rendus Physique*, 13(3):316–327, 2012.

[148] W. Ludwig, A. King, P. Reischig, M. Herbig, E.M. Lauridsen, S. Schmidt, H. Proudhon, S. Forest, P. Cloetens, S. Roscoat, et al. New opportunities for 3D materials science of polycrystalline materials at the micrometre lengthscale by combined use of X-ray diffraction and X-ray imaging. *Materials Science and Engineering: A*, 524(1):69–76, 2009.

[149] A. King, G. Johnson, D. Engelberg, W. Ludwig, and T.J. Marrow. Observations of intergranular stress corrosion cracking in a grain-mapped polycrystal. *Science*, 321(5887):382–385, 2008.

[150] A. King, W. Ludwig, M. Herbig, J.-Y. Buffière, A.A. Khan, N. Stevens, and T.J. Marrow. Three-dimensional in situ observations of short fatigue crack growth in magnesium. *Acta Materialia*, 59(17):6761–6771, 2011.

[151] M. Herbig, A. King, P. Reischig, H. Proudhon, E.M. Lauridsen, T.J. Marrow, J.-Y. Buffière, and W. Ludwig. 3-D growth of a short fatigue crack within a polycrystalline microstructure studied using combined diffraction and phase-contrast X-ray tomography. *Acta Materialia*, 59(2):590–601, 2011.

[152] P.J. Withers and M. Preuss. Fatigue and damage in structural materials studied by X-ray tomography. *Annual Review of Materials Research*, 42:81–103, 2012.

[153] H.D. Beeson, D.D. Davis, W.L. Ross, Sr., and R.M. Tapphorn. Composite overwrapped pressure vessels. Technical Report TP-2002-210769, NASA, 2002.

[154] P.B. McLaughlan, S.C. Forth, and L.R. Grimes-Ledesma. Composite overwrapped pressure vessels, a primer. *NASA Special Publication NASA/SP-2011-573*, March 2011.

[155] R.M.Suter, D. Hennessy, C. Xiao, and U. Lienert. Forward modeling method for microstructure reconstruction using X-ray diffraction microscopy: Single-crystal verification. *Review of Scientific Instruments*, 77(12):123905–123905, 2006.

[156] S.F. Li and R.M. Suter. Adaptive reconstruction method for three-dimensional orientation imaging. *Journal of Applied Crystallography*, 46(2):512–524, 2013.

[157] B.N. Cox and W.L. Morris. Monte carlo simulations of the growth of small fatigue cracks. *Engineering Fracture Mechanics*, 31(4):591–610, 1988.

[158] B.N. Cox. Inductions from monte carlo simulations of small fatigue cracks. *Engineering Fracture Mechanics*, 33(4):655 – 670, 1989.

[159] C.Y. Kung and M.E. Fine. Fatigue crack initiation and microcrack growth

in 2024-T4 and 2124-T4 aluminum alloys. *Metallurgical Transactions A*, 10(5):603–610, 1979.

[160] W.J. Baxter and T.R. McKinney. Growth of slip bands during fatigue of 6061-T6 aluminum. *Metallurgical Transactions A*, 19(1):83–91, 1988.

[161] Y.H. Zhang and L. Edwards. On the blocking effect of grain boundaries on small crystallographic fatigue crack growth. *Materials Science and Engineering: A*, 188(1):121–132, 1994.

[162] R.S. Piascik and R.P. Gangloff. Environmental fatigue of an Al-Li-Cu alloy: Part II. Microscopic hydrogen cracking processes. *Metallurgical Transactions A*, 24(1):2751–2762, 1993.

[163] D.L. McDowell. A perspective on trends in multiscale plasticity. *International Journal of Plasticity*, 26(9):1280–1309, 2010.

[164] D.L. McDowell and F.P.E. Dunne. Microstructure-sensitive computational modeling of fatigue crack formation. *International Journal of Fatigue*, 32(9):1521–1542, 2010.

[165] D. McDowell, K. Gall, M. Horstemeyer, and J. Fan. Microstructure-based fatigue modeling of cast A356-T6 alloy. *Engineering Fracture Mechanics*, 70(1):49–80, 2003.

[166] Y. Xue, D. McDowell, M. Horstemeyer, M. Dale, and J. Jordon. Microstructure-based multistage fatigue modeling of aluminum alloy 7075-T651. *Engineering Fracture Mechanics*, 74(17):2810–2823, 2007.

[167] K.-S. Cheong, M.J. Smillie, and D.M. Knowles. Predicting fatigue crack initiation through image-based micromechanical modeling. *Acta Materialia*, 55(5):1757 – 1768, 2007.

[168] T.R. Bieler, P. Eisenlohr, F. Roters, D. Kumar, D.E. Mason, M.A. Crimp, and D. Raabe. The role of heterogeneous deformation on damage nucleation at grain boundaries in single phase metals. *International Journal of Plasticity*, 25(9):1655–1683, 2009.

[169] J.E. Bozek, J.D. Hochhalter, M.G. Veilleux, M. Liu, G. Heber, S.D. Sintay, A.D. Rollett, D.J. Littlewood, A.M. Maniatty, H. Weiland, et al. A geometric approach to modeling microstructurally small fatigue crack formation: I. Probabilistic simulation of constituent particle cracking in AA

7075-T651. *Modelling and Simulation in Materials Science and Engineering*, 16(6):065007, 2008.

[170] J.D. Hochhalter, D.J. Littlewood, R.J. Christ, Jr., M.G. Veilleux, J.E. Bozek, A.R. Ingraffea, and A.M. Maniatty. A geometric approach to modeling microstructurally small fatigue crack formation: II. Physically based modeling of microstructure-dependent slip localization and actuation of the crack nucleation mechanism in AA 7075-T651. *Modelling and Simulation in Materials Science and Engineering*, 18(4):045004, 2010.

[171] G.P. Potirniche and S.R. Daniewicz. Finite element modeling of microstructurally small cracks using single crystal plasticity. *International Journal of Fatigue*, 25(911):877 – 884, 2003. International Conference on Fatigue Damage of Structural Materials IV.

[172] M. Shenoy, J. Zhang, and D.L. McDowell. Estimating fatigue sensitivity to polycrystalline Ni-base superalloy microstructures using a computational approach. *Fatigue & Fracture of Engineering Materials & Structures*, 30(10):889–904, 2007.

[173] L. Wang, S.R. Daniewicz, M.F. Horstemeyer, S. Sintay, and A.D. Rollett. Three-dimensional finite element analysis using crystal plasticity for a parameter study of microstructurally small fatigue crack growth in a AA7075 aluminum alloy. *International Journal of Fatigue*, 31(4):651 – 658, 2009.

[174] A.M. Cuitio and M. Ortiz. Three-dimensional crack-tip fields in four-point-bending copper single-crystal specimens. *Journal of the Mechanics and Physics of Solids*, 44(6):863 – 904, 1996.

[175] S. Flouriot, S. Forest, G. Cailletaud, A. Köster, L. Rémy, B. Burgardt, V. Gros, S. Mosset, and J. Delautre. Strain localization at the crack tip in single crystal CT specimens under monotonous loading: 3D finite element analyses and application to nickel-base superalloys. *International Journal of Fracture*, 124(1-2):43–77, 2003.

[176] C.M. Hefferan, S.F. Li, J. Lind, U. Lienert, A.D. Rollett, P. Wynblatt, and R.M. Suter. Statistics of high purity nickel microstructure from high energy X-ray diffraction microscopy. *Computers, Materials, & Continua*, 14(3):209–220, 2010.

[177] U. Lienert, S.F. Li, C.M. Hefferan, J. Lind, R.M. Suter, J.V. Bernier, N.R. Bar-

ton, M.C. Brandes, M.J. Mills, M.P. Miller, et al. High-energy diffraction microscopy at the advanced photon source. *JOM*, 63(7):70–77, 2011.

[178] E.O. Hall. The deformation and ageing of mild steel: III Discussion of results. *Proceedings of the Physical Society B*, 64:747–753, 1951.

[179] N.J. Petch. The cleavage strength of polycrystals. *J. Iron Steel Inst.*, 174:25–28, 1953.

[180] J.D. Evensen, N. Ryum, and J.D. Embury. The intergranular fracture of Al-Mg-Si alloys. *Materials Science and Engineering*, 18(2):221–229, 1975.

[181] K. Matouš and A.M. Maniatty. Finite element formulation for modelling large deformations in elasto-viscoplastic polycrystals. *International Journal for Numerical Methods in Engineering*, 60(14):2313–2333, 2004.

[182] A.M. Maniatty, P.R. Dawson, and Y.-S. Lee. A time integration algorithm for elasto-viscoplastic cubic crystals applied to modelling polycrystalline deformation. *International Journal for Numerical Methods in Engineering*, 35(8):1565–1588, 1992.

[183] D. Peirce, R.J. Asaro, and A. Needleman. Material rate dependence and localized deformation in crystalline solids. *Acta Metallurgica*, 31(12):1951–1976, 1983.

[184] U.F. Kocks. Laws for work-hardening and low-temperature creep. *Journal of Engineering Materials and Technology*, 98(1):76–85, 1976.

[185] E. Voce. A practical strain-hardening function. *Metallurgia*, 51(307):219–226, 1955.

[186] J.B. de Jonge, D. Schutz, H. Lowak, and J. Schijve. A standardized load sequence for flight simulation tests on transport aircraft wing structures. NLR Technical Report TR 73029 U, National Aerospace Laboratory NLR, Amsterdam, The Netherlands, 1973.

[187] J.B.Cavalcante Neto, P.A. Wawrzynek, M.T.M. Carvalho, L.F. Martha, and A.R. Ingraffea. An algorithm for three-dimensional mesh generation for arbitrary regions with cracks. *Engineering with Computers*, 17(1):75–91, 2001.